ISAS - INTERNATIONAL SCHOOL FOR ADVANCED STUDIES

First–principle studies of structural phase transformations

Thesis submitted for the degree of

"Doctor Philosophiæ"

CANDIDATE

Paolo Focher

SUPERVISORS

Prof. Michele Parrinello

Dr. Guido L. Chiarotti

October 1994

TRIESTE

SISSA - SCUOLA INTERNAZIONALE SUPERIORE STUDI AVANZATI

TRIESTE

Strada Costiera 11

SISSA ISAS
SCUOLA INTERNAZIONALE SUPERIORE DI STUDI AVANZATI
INTERNATIONAL SCHOOL FOR ADVANCED STUDIES

First-principle studies of structural phase transformations

Thesis submitted for the degree of

"Doctor Philosophiæ"

CANDIDATE

Paolo Focher

SUPERVISORS

Prof. Michele Parrinello

Dr. Guido L. Chiarotti

October 1994

Ai miei genitori

Table of Contents

List of Figures

1 Introduction

Solid–solid structural phase transitions with increasing of pressure and/or temperature are ubiquitous in condensed matter. Existing *ab–initio* theory of these transitions has been mostly restricted to the study of relative energies of known structural phases at different volumes and at zero temperature [1]. Despite a remarkable level of understanding attained in this area, the main goal of simulating these transitions under real conditions of temperature and pressure, while still retaining the first principles accuracy required for the prediction of new structures, has not yet been achieved. In particular, heavily first order structural phase transitions do not take place in *ab–initio* Car–Parrinello Molecular Dynamics simulation [2], in spite of a correct description of both energetics and thermal fluctuations. The problem lies in the (mandatory) use of periodic boundary conditions within a rigid simulation cell, which does not allow for the necessary density and shape fluctuations.

In the early 80's Parrinello and Rahman proposed a lagrangian which, by allowing for a variation of the periodic boundary conditions guided by the internal stress, made simulations of solid–solid phase transitions possible [3]. However, existing implementations of

the Parrinello–Rahamn scheme are based on empirical – rather than *ab–initio* – potentials: this restriction reduces the predictive power, and thus the general usefulness of numerical simulations in this relevant field, particularly where phase transitions are accompained by a large reconstruction of electronic states and thus of the chemical bonding properties.

In this thesis we present a new computational scheme for constant–pressure *ab–initio* Molecular Dynamics, which allows the simulation of these phenomena with the correct quantum–mechanical description of inter–atomic forces and internal stress along with the correct statistical mechanics of ionic degrees of freedom. This is obtained by efficiently combining the Car–Parrinello with the Parrinello–Rahman method.

This new scheme, while describing the ionic dynamics with first principles accuracy, still allows for the symmetry breaking fluctuations necessary for phase transitions to take place *spontaneously* during the simulation, due to variations of external pressure and/or temperature. At variance with standard total–energy calculations, within our new scheme the prediction of new phases is obtained without any initial guess on the final stable structure.

The metal–insulator transition in silicon from diamond to high density phases is well known and the underneath physics established. For this reason silicon has been chosen as test case for our scheme. In the section of the thesis devoted to describe this first application we point out technical details and difficulties encountered in this type of simulation.

The absence of extensive theoretical studies and contradictory experimental results make the C_{60} pressure induced transformation from fullerite to amorphous carbon a very challenging and appealing subject to be studied via our first–principle constant pressure

method. The simulation of $C_{60} \rightarrow$ a–C points out that a–C obtained in this way differs from those obtained via melt–quenching, showing in particular a high density of sp^3 sites. These are not clustered as in ordinary a–C, but percolate in the whole space. Moreover the simulation show an intermediate molecular phase, in which C_{60} molecules are connected by short (diamond–like) covalent bonds.

Finally we face two other applications of our method: graphite $\rightarrow$ diamond conversion in carbon and acetylene polymerization. At the time writing the work on these subjects is still in progress and we present few preliminary results.

Many interesting solid–solid phase transformations involve oxides. Since the standard norm–conserving pseudopotential for oxygen is to hard for practical use, we have implemented in our computational scheme also the more recent ultra–soft pseudopotentials. The technique opens the way to explore this new stimulating field.

The thesis is divided in the following parts: in Chapter 2 we describe the theory underneath our scheme. Starting from a brief review of both original Parrinello–Rahman method and Car–Parrinello Molecular Dynamics, we present our extension of the latter to allow constant–pressure simulations. In Chapter 3 the guide–lines for the practical implementation of the method are given. In particular we focous our attention to the derivation of quantum–mechanical stress tensor, the new quantity needed for constant–pressure Molecular Dynamics. We also describe the main differences in the implementation using two different classes of atomic pseudopotentials: the "standard" norm–conserving and the recent ultra–soft pseudopotentials. At the end of this chapter we discuss the problems arising in the electronic wave–functions representation using a constant–number

plane–wave expansion when the simulation box varies, and we propose a modification of energy density functional in order to perform constant cut–off simulations. Chapter 4 is devoted to the description of the above mentioned applications. Finally the last Chapter is devoted to conclusions.

2 Theory

In this chapter we present the method for *ab–initio* Molecular Dynamics with variable cell in three steps: at first we review the original Parrinello–Rahman [3] method for classical MD. We briefly recall the well–known Car–Parrinello [2] scheme in its original formulation for fixed cell, and finally present our extension of Car–Parrinello by including Parrinello–Rahman.

2.1 Parrinello–Rahman Molecular Dynamics

The Parrinello–Rahman method (PR) is the natural extension of Andersen [4] Molecular Dynamics. In the original Andersen method the simulation cell is allowed to change its size *isotropically*, following the deviation of internal pressure from an assigned value. This is done by introducing the volume of the cell as a new dynamical variable, without renouncing to the periodic boundary conditions. In the PR method, the cell can change, more generally, both shape and size, thus adding to the problem the degrees of freedom of the cell, in the following way.

Let us consider a generic simulation cell for MD, which fill all the space by repeating

it at infinity with periodic boundary conditions. The MD cell is described by the three primitive Bravais vectors $(\mathbf{a}, \mathbf{b}, \mathbf{c})$. Defining the matrix

$$\mathbf{h} = (\mathbf{a}, \mathbf{b}, \mathbf{c}) \tag{2.1}$$

(where the vectors constitute the columns of the matrix) , the real space position of a generic particle in the box, $\mathbf{R}$, can be written as:

$$\mathbf{R} = \mathbf{h}\mathbf{S}. \tag{2.2}$$

$\mathbf{S}$ is the vector of the so called *scaled* coordinates of the particle, whose components assume values between 0 and 1 inside the cell. (In other words, in the scaled variable space, the cell is always a cube of side 1.) The relation between distances in real and in scaled coordinates will be given by the metric tensor $\mathcal{G} = \mathbf{h}^t\mathbf{h}$, so that:

$$(\mathbf{R}_i - \mathbf{R}_j)^2 = (\mathbf{S}_i - \mathbf{S}_j)^t \mathcal{G} (\mathbf{S}_i - \mathbf{S}_j). \tag{2.3}$$

Since we want the cell to change in time, the basic idea of Parrinello–Rahman method. in analogy with Andersen dynamics, is to consider an *extended* langrangian system, where the nine components of the matrix $\mathbf{h}$ are classical degrees of freedom, whose trajectories are determined by appropriate generalized forces. This is obtained by writing the Lagrangian $\mathcal{L}$ of the extended system as:

$$\mathcal{L} = \frac{1}{2}\sum_{i=1}^{N} M_i(\dot{\mathbf{S}}_i^t \mathcal{G} \dot{\mathbf{S}}_i) - V(\mathbf{R}_1, ..., \mathbf{R}_N) + \frac{1}{2} W \mathrm{Tr}(\dot{\mathbf{h}}^t \dot{\mathbf{h}}) - p\Omega, \tag{2.4}$$

where M_i is the mass of i-th particle, V the classical potential, W an inertia parameter controlling the cell motion, p the external pressure, and $\Omega = \det \mathbf{h}$ the volume of the simulation cell.

The first two terms of Eq. 2.4 define the Lagrangian for the usual fixed cell Molecular Dynamics. Note however that when the cell varies in time, the kinetic energy term in Eq. 2.4 does not correspond to the actual kinetic energy of the particles in the real system.

The Euler-Lagrange equations of motion derived from Eq. 2.4 are:

$$\ddot{\mathbf{S}}_i^\alpha = -\frac{1}{M_i}\frac{\partial V}{\partial \mathbf{R}_i^\beta}(\mathbf{h}^t)^{-1}_{\beta\alpha} - \mathcal{G}^{-1}_{\alpha\beta}\dot{\mathcal{G}}_{\beta\gamma}\dot{\mathbf{S}}_i^\gamma, \tag{2.5}$$

$$\ddot{\mathbf{h}}_{\alpha\beta} = \frac{1}{W}\left(\Pi_{\alpha\gamma} - p\delta_{\alpha\gamma}\right)\Omega(\mathbf{h}^t)^{-1}_{\gamma\beta}, \tag{2.6}$$

where:

$$\Pi_{\alpha\gamma} = \frac{1}{\Omega}\left(\sum_i M_i \mathbf{v}_i^\alpha \mathbf{v}_i^\gamma - \frac{\partial V}{\partial \mathbf{h}_{\alpha\delta}}\mathbf{h}^t_{\delta\gamma}\right), \tag{2.7}$$

and

$$\mathbf{v}_i^\alpha = \mathbf{h}_{\alpha\gamma}\dot{\mathbf{S}}_i^\gamma. \tag{2.8}$$

(Greek indices indicate the components of vectors and matrices, and the convention of implicit sum over repeated indices is assumed.)

Interpreting $M_i\mathbf{v}_i$ as the momentum of i-th particle, Π is nothing but the internal stress tensor. This can be seen by comparing the second term of Π with the usual definition of internal stress tensor coming from the theory of elasticity [5]:

$$\pi_{\alpha\beta} = -\frac{1}{\Omega}\frac{\partial V}{\partial \epsilon_{\alpha\beta}}, \tag{2.9}$$

where ϵ is the strain tensor with respect to the present configuration. Let ϵ be a small strain, which deforms the cell from $\mathbf{h}$ to $\mathbf{h}' = \mathbf{h} + d\mathbf{h}$ and the positions from $\mathbf{R}$ to $\mathbf{R}'$; we

have (up to first order in $\mathbf{dh}$):

$$\mathbf{R}' = (1+\epsilon)\mathbf{R} = \mathbf{h}'\mathbf{S} = \mathbf{h}'\mathbf{h}^{-1}\mathbf{R}. \tag{2.10}$$

Therefore:

$$\epsilon = \mathbf{h}'\mathbf{h}^{-1} - \mathbf{1}, \tag{2.11}$$

from which we obtain:

$$\frac{\partial V}{\partial \mathbf{h}}\mathbf{h}^t = \frac{\partial V}{\partial \epsilon}. \tag{2.12}$$

From Eq. 2.6 we see that the "forces" on the cell are proportional to the difference $(\Pi - p)$, which implies that the time variation of matrix $\mathbf{h}$ is driven by the imbalance between external pressure and total stress.

The Lagrangian (Eq. 2.4) is conservative with the constant of motion given by:

$$\mathcal{H} = \frac{1}{2}\sum_i M_i v_i^2 + V(\mathbf{R}_1, ..., \mathbf{R}_N) + p\Omega + \frac{1}{2}W\mathrm{Tr}(\dot{\mathbf{h}}^t\dot{\mathbf{h}}). \tag{2.13}$$

Physically $\langle\mathcal{H}\rangle$ corresponds to the enthalpy of the system [6], apart for the last term, which becomes negligible for large N (its contribution to $\langle\mathcal{H}\rangle$ at equilibrium is $\frac{9}{2}k_BT$).

It has been shown [7, 4] that trajectories generated with PR dynamics give averages of thermodynamical quantities that are in fact equivalent in the thermodynamical limit to the Gibbs averages in the (H,p,N) statistical ensemble, i.e. the ensemble with enthalpy, pressure and number of particles kept constant.

Let us point out some considerations about the role played by the parameter W. In the equations this quantity is the "mass" of the cell, in the sense that it is related to the *inertia* of $\mathbf{h}$. It is clear that W does not influence equilibrium properties, since in

classical mechanics the equilibrium properties of a system do not depend on the mass of the constituents. This is however no longer true for dynamical properties. Andersen has suggested a physical criterion for the choice of W: W should be tuned so as to obtain a relaxation time of the cell of the order of $\tau = L/c$, where L is the linear dimension of the cell and c the sound velocity inside the system. From a slightly different point of view, one can estimate the characteristic frequency of the cell by linearizing Eq. 2.6. Assuming this frequency to be roughly $1/\tau$, one obtains [6]: $W = 3\sum_i M_i/4\pi^2$.

After the original work of Parrinello and Rahman [3] several improvements of variable–cell MD has been proposed. In particular constant pressure MD lends itself naturally to the introduction of non–isotropic external stress [8], which may be used for simulations of uniaxial stress transformations.

It is also possible to combine PR-MD with Nosè thermostat [9], in order to sample the statistical ensamble where free energy, pressure and number of particles are kept constant. One possibility (which we followed in our MD scheme) is to simply add to PR Lagrangian the Nosè energy terms [9]. The discussion about the sampling of the corresponing statistical ensamble by the trajectories of such combined Lagrangian is given in Ref. [10].

More recently Wentzcovitch [11] has proposed a slightly different Lagrangian for variable–cell MD under constant pressure, where the fictitious degrees of freedom for the extended classical system are taken to be the strain tensor components with respect to a given reference state. This differs from original PR where the degrees of freedom are the components of matrix $\mathbf{h}$. In the Wentzcovitch extension the Lagrangian has the symmetry

of the system and not of the chosen simulation cell, and the symmetry breaking needed to induce a structural transformation is due only to thermal fluctuations (first term in Eq. 2.7). This symmetry constraint on the equations of motion seems to be useful for structural parameters optimization or dynamical properties studies *inside* a given phase for the system, but may actually limit the freedom of the extended classical system to explore its configuration space.

To conclude this introduction to the PR formulation we briefly point out some comments about its applicability. PR works well when applied to solid–solid transformation. On the contrary it it may show some pathologies when reproducing solid–liquid phase transitions, due to the zero shear modulus in the liquid phase [12]: if the initial imbalance between internal stress and external applied pressure leads to a distortion of the cell, the liquid will not "drive" this distortion with "physical" elastic forces, and the motion of the cell will be mostly determined by the choice of the initial conditions. This bad coupling between atomic positions and fictitious cell dynamics may also occur for crystals with a small bulk modulus (such as molecular crystals): for these systems the internal stress of Eq. 2.7 mostly depends on the molecular configuration than on the week Van der Waals interaction between molecules. In this case attention has to paied to the relaxation time of the cell, which means to the choice of the "mass" W in Eq. 2.6, in particular during a decompression of the system. Indeed, if the initial conditions drive an expansion of the cell and the relaxation time of the molecules is fast enough with respect to cell expansion leaving the molecule length almost constant, internal stress will not vary significantly and the expansion may lead to an unphysical fragmentation of the system. Finally we under-

line that the dynamics of the cell is fictitious, and dependent on the choice of W. For this reason one must be cautious in comparing simulated transition paths with physical ones.

2.2 Car–Parrinello Molecular Dynamics

The Car–Parrinello method (CP) [2, 13, 14] is a very elegant and powerful scheme for ab–initio MD simulations, successfully used in the last years for solving a wide variety of problems for real materials which were inaccessible for standard simulation method (see, for example, Ref. [15] and references therein). In CP the forces acting on classical ionic degrees of freedom are calculated not from a parameter–dependent potential – usually determined via an empirical *ad hoc* procedure – but from the quantum treatment of the electronic system based on Density Functional Theory (DFT) [16, 17, 18] in a consistent way as the simulation proceeds. This is done by introducing a *fictitious* dynamical system, associated with the *physical* system, whose potential energy surface E is an appropriate functional of both ionic and electronic degrees of freedom, with electronic wave–functions treated as classical fields. The fictitious system is devised in such a way that the ionic trajectories generated by its dynamics reproduce very closely those of the physical system with Born–Oppenheimer (BO) energy surface V defined by $V(\{\mathbf{R}_I\}) = \min_{\{\psi_i\}} E\left[\{\psi_i\}, \{\mathbf{R}_I\}\right]$. The generalized classical Lagrangian of the fictitious system is defined as:

$$\begin{aligned} \mathcal{L} &= \mu \sum_{i}^{\text{OCC}} \int d\mathbf{r}\, |\dot{\psi}_i(\mathbf{r})|^2 + \frac{1}{2} \sum_I M_I \dot{\mathbf{R}}_I^2 - E\left[\{\psi_i\}, \{\mathbf{R}_I\}\right] \\ &+ \sum_{ij} \Lambda_{ij} \left(\int d\mathbf{r}\, \psi_i^*(\mathbf{r}) \psi_j(\mathbf{r}) - \delta_{ij} \right). \end{aligned} \tag{2.14}$$

$\mathcal{L}$ is a functional of ionic positions $\mathbf{R}_I$ and electronic wave–functions ψ_i, treated here as classical scalar fields. The parameter μ (of units mass $\times$ length^2) is the generalized mass for the electronic degrees of freedom. The sums over i and j are taken on the electronic states, and the sum over I on the ions. The first and second term in Eq. 2.14 are the (classical) kinetic energy of the electronic and ionic degrees of freedom; E given by the DFT total energy functional is the potential energy of the coupled electron–ion fictitious system. Λ_{ij} are the Lagrangian multiplier associated with the orthonormalization constraints of the wave–functions. [1] The Euler–Lagrange equations of motion derived from Eq. 2.14 are:

$$\mu\ddot{\psi}_i(\mathbf{r}) = -\frac{\delta E}{\delta \psi_i^*(\mathbf{r})} + \sum_j \Lambda_{ij}\psi_j(\mathbf{r}) \tag{2.15}$$

$$\ddot{\mathbf{R}}_I = -\frac{1}{M_I}\frac{\partial E}{\partial \mathbf{R}_I}. \tag{2.16}$$

In general the ionic trajectories generated by Eq. 2.16 and those obtained by:

$$\ddot{\mathbf{R}}_I = -\frac{1}{M_I}\frac{\partial V(\{\mathbf{R}_I\})}{\partial \mathbf{R}_I} \tag{2.17}$$

do not coincide, unless $E[\{\psi_i\},\{\mathbf{R}_I\}]$ is at the instantaneous minimum. However, the *mass* μ and the initial conditions on the wave–functions can be chosen in such a way that the time–scale for the electronic degrees of freedom is much shorter than that of the ions, allowing the electrons, initially lying on the BO surface, to follow abiabatically the ionic motion remaining close to the instantaneous ground state. If this condition for the

[1] The Lagrangian in Eq. 2.14 is correct for a system where the occupied electronic states are described by a set of mutually orthogonal wave–functions. If the orthonormalization constraint is relaxed, the last term of Eq. 2.14 has to be modified (see, for example, the case of ultra–soft pseudopotentials described in Section 3.2).

adiabatic motion is satisfied, the instantaneous value of the forces acting on the ions does not coincide with the Hellmann–Feynman forces, but their *average* value does to a very high degree of accuracy [19, 15].

Although entirely classical, the fictitious dynamics of electronic wave–functions accounts for the properties of the quantum eigenvalue spectrum of the electrons. It has been shown [20] that for small deviations from the ground state, the dynamics of the wave–functions can be well described as a superposition of oscillations whose frequency is given by:

$$\omega_{ij} = \left(\frac{2(\epsilon_j - \epsilon_i)}{\mu}\right)^{\frac{1}{2}}, \tag{2.18}$$

where ϵ_j and ϵ_i are the eigenvalues of an empty and an occupied state respectively. From Eq. 2.18 one gets that the lowest characteristic frequency for the electronic degrees of freedom is: $\omega_{\min} = (2E_g/\mu)^{\frac{1}{2}}$, where E_g is the energy gap.

Since the condition for the adiabatic separation of electronic and ionic degrees of freedom is that $\omega_{\min}$ is much higher than the highest ionic frequency, the CP method works well, with a proper choice of parameter μ, for systems with a clearly defined single–particle gap, like semiconductors and insulators. The use of CP for metals is more subtle: in this case E_g is vanishing in an infinite system and is very small in a finite one. Thus one has in principle to use a very small value of μ to obtain an adiabatic separation between ionic and electronic degrees of freedom. The use of small electronic mass has however the serious drawback that a small time step has to be used in the numerical integration of Eqs. 2.15, 2.16. In practice, for resonable values of the integration step, this adiabatic separation is not obtained for metals and an irreversible transfer of energy between ions

and electrons is observed [20, 15]. This leads to a quick drift of the electrons from the BO surface and to a cooling of the ions. To overcome this problem the use of two different Nosé [9] thermostats has been proposed [21]: one coupled to the ions, to keep them at the desired temperature, and the other to the electronic wave–functions, to keep them "cold", which means close to the BO surface.

2.3 Constant Pressure Ab–initio Molecular Dynamics

We now extend the previous formulation of the original Parrinello–Rahman method to the case of CP described above.

The problem of extending this method to the case of a deformable cell is in principle the same as for classical systems. One would like to take into account shape and volume changes of the simulation cell (CP with changing cell volume has already been developed by Buda *at al.* [22] implementing the Andersen MD [4] in the original CP) by considering the extended system obtained by rewriting the original Lagrangian (Eq. 2.14) in scaled coordinates with the two additional terms pertaining to the cell (last two terms in Eq. 2.4).

The presence of the electronic wave–functions in the CP Lagrangian makes this procedure slightly more subtle here than in the classical case. We want indeed to write a new classical Lagrangian, which reduces to the original CP Lagrangian in the fixed cell case, and in which the degrees of freedom are some scalar fields ψ (not explicitly dependent on $\mathbf{h}$) associated to the electrons, the scaled ionic coordinates $\mathbf{S}$ and the cell matrix $\mathbf{h}$. We also want to preserve the physical meaning of PR equations of motion. It is clear that the original wave–functions $\psi_h(\mathbf{r})$ (where the lower index h indicates a wave–function defined

and normalized on the cell generated by $\mathbf{h}$) are no longer a good candidate for being the scalar field of our Lagrangian, because of the dependence on the cell. The natural way to scale the ψ, which we will demonstrate to have several advantages, is to define the wave–functions ψ onto the scaled variable space $\mathbf{s} = \mathbf{h}^{-1}\mathbf{r}$ (normalized on the unitary cube), such as:

$$\psi_h(\mathbf{r}) = \frac{1}{\sqrt{\Omega}}\psi(\mathbf{h}^{-1}\mathbf{r}) = \frac{1}{\sqrt{\Omega}}\psi(\mathbf{s}), \tag{2.19}$$

where the prefactor $1/\sqrt{\Omega}$ preserves the normalization. As required $\psi(\mathbf{s})$ is independent on $\mathbf{h}$. From Eq. 2.19 follows the transformation law for the electronic charge density, which appear in the DFT energy functional (see Eq. 3.1 in the next section):

$$\rho_h(\mathbf{r}) = \frac{1}{\Omega}\rho(\mathbf{h}^{-1}\mathbf{r}). \tag{2.20}$$

This choice for the transformation of the wave–functions corresponds to consider that the only *direct* effect of the deformation of the cell on the wave–functions and on the electronic density in real space is a "stretching"of them, in order to satisfy the changed boundary conditions.

Starting from Eq. 2.14 we write the new Lagrangian as:

$$\begin{aligned}\mathcal{L} &= \mu\sum_i \int ds\, |\dot{\upsilon}_i(\mathbf{s})|^2 + \frac{1}{2}\sum_I M_I(\dot{\mathbf{S}}_I^t \mathcal{G}\dot{\mathbf{S}}_I) - E\left[\{\psi_i\}, \{\mathbf{h}\mathbf{S}_I\}\right] + \\ &\sum_{ij}\Lambda_{ij}\left(\int ds\, \psi_i^*(\mathbf{s})\psi_j(\mathbf{s}) - \delta_{ij}\right) + \frac{1}{2}W\mathrm{Tr}(\dot{\mathbf{h}}^t\dot{\mathbf{h}}) - p\Omega,\end{aligned} \tag{2.21}$$

where the integrals are taken on the scaled cell (of volume $\Omega_0 = 1$). Notice that if the cell is kept fixed, Eq. 2.21 reduces to the original CP Lagrangian (Eq. 2.14), written for the scaled wave–functions, apart for the constant term $p\Omega$. From Eq. 2.19 the integrals in the

first and fourth term of Eq. 2.21 are, in fact, invariant under scale transformation:

$$\int_{\Omega_0} \psi^*(\mathbf{s})\psi(\mathbf{s})d\mathbf{s} = \Omega \int_{\Omega_0} \psi_h^*(\mathbf{hs})\psi_h(\mathbf{hs})d\mathbf{s} = \int_{\Omega} \psi_h^*(\mathbf{r})\psi_h(\mathbf{r})d\mathbf{r}. \tag{2.22}$$

Notice also that using the scaled wave–functions, we neglect in the kinetic term (first term of Eq. 2.21) the contribution due to the deformation of the cell (exactly in the same way as in Eq. 2.4 this contribution to the kinetic energy of the ions is neglected). This ensures that the equations of motion for the electronic wave–functions are formally the same of original CP (Eq. 2.15).

The equations for ionic degrees of freedom have exactly the same form as in classical PR case (see Eq. 2.5), with the replacement of the classical forces $-\partial V/\partial \mathbf{R}$ with $-\partial E/\partial \mathbf{R}$, which gives, like in Eq. 2.16, the actual quantum–mechanical forces acting on the ions [19].

The independence of the integrals in Eq. 2.21 on $\mathbf{h}$ ensures also that no extra terms with respect to Eq. 2.6 appear in the equations for the cell parameters. Here in the tensor Π (Eq. 2.7) $\partial V/\partial \mathbf{h}$ is replaced by $\partial E/\partial \mathbf{h}$. This is the partial derivative of a functional of classical fields and coordinates, and we will show that it is nothing but the quantum–mechanical internal stress tensor. For this reason the proposed extension of PR Dynamics in the *ab–initio* scheme is physically meaningful.

If we consider the electronic quantum Hamiltonian of our system and the ground state Ψ_o corresponding to a generic configuration of cell ($\mathbf{h}$) and ions, then we have seen in the previous section that $E \simeq \langle \Psi_o | H | \Psi_o \rangle$ (apart from small deviations due to the oscillations of wave–functions around their instantaneous ground–state). In close analogy to the Hellmann–Feynmann theorem, it can be shown [23, 24] that the calculation of

$\partial E/\partial \mathbf{h}$ at a generic $\mathbf{h}$ does not require the knowledge of the perturbed ground–state, since, from the variational property of E, the perturbation of the ground–state due to $\mathrm{d}\mathbf{h}$ does not change E to first order. We can therefore calculate the derivative of E as the expectation value on Ψ_o of the derivative of the electronic Hamiltonian, *i.e.* the partial derivative inside E, keeping the wave–functions constant. However one has to pay attention in the present case to the "stretching" of the unperturbed ground–state wave–functions: since the wave–functions satisfy boundary conditions, which are changed by the perturbation, it is necessary to rescale the "stretched" functions such as to preserve their normalization on the perturbed cell. This is automatically taken into account by replacing $\psi_h(\mathbf{r})$ with $\psi(\mathbf{s})$ using Eq. 2.19. This indeed implies that the term $(\partial E/\partial \mathbf{h})\mathbf{h}^t$ (see also Eq. 2.12) appearing in Π (Eq. 2.7) is the actual quantum–mechanical stress tensor, as we want.

Summarizing, we have shown in this section how it is possible to extend in a general and natural way the PR method into the CP Molecular Dynamics. All the equations of motion derived from the Lagrangian in Eq. 2.21 can be formally written as:

$$\mu\ddot{\psi}_i(\mathbf{s}) = -\frac{\delta E}{\delta \psi_i^*(\mathbf{s})} + \sum_j \Lambda_{ij}\psi_j(\mathbf{s}) \tag{2.23}$$

$$\ddot{\mathrm{S}}_i^\alpha = -\frac{1}{M_i}\frac{\partial E}{\partial \mathbf{R}_i^\beta}(\mathbf{h}^t)^{-1}_{\beta\alpha} - \mathcal{G}^{-1}_{\alpha\beta}\dot{\mathcal{G}}_{\beta\gamma}\dot{\mathrm{S}}_i^\gamma, \tag{2.24}$$

$$\ddot{\mathbf{h}}_{\alpha\beta} = \frac{1}{W}(\Pi_{\alpha\gamma} - p\delta_{\alpha\gamma})\,\Omega(\mathbf{h}^t)^{-1}_{\gamma\beta}. \tag{2.25}$$

Next chapter is devoted to the description of the explicit derivation in the framework of CP method of the internal stress tensor, the only quantity which is still lacking for a practical implementation of the *ab–initio* Molecular Dynamics with deformable cell.

3 Implementation: Stress Tensor from DFT–LDA Total Energy

Consider a system of N atoms and M electronic states ($\{\psi(\mathbf{r})\}$) in a cell generated by $\mathbf{h}$. (For simplicity we consider in the following just one atomic species, the extension to more than one species being trivial.) The interaction between electrons and ions is described by using ab–initio pseudopotentials [25, 26]. For such a system, the DFT total energy E in Local Density Approximation (LDA) [17, 27, 28] can be written as:

$$\begin{aligned} E\left[\{\psi_i\},\{\vec{R}_I\}\right] &= \sum_i^{occ} f_i \int \mathrm{d}\vec{r}\,\psi_i^*(\vec{r})\left(-\frac{1}{2}\nabla^2 + V_{\mathrm{nl}}^{\mathrm{ps}}\right)\psi_i(\vec{r}) + \int \mathrm{d}\vec{r} V_{\mathrm{loc}}^{\mathrm{ps}}(\vec{r})\rho_e(\vec{r}) \\ &+ \frac{1}{2}\int \mathrm{d}\vec{r}\,\mathrm{d}\vec{r}\,'\frac{\rho_e(\vec{r})\rho_e(\vec{r}\,')}{|\vec{r}-\vec{r}\,'|} + E_{xc}[\rho_e] + \sum_{I\neq J}\frac{Z_v^2}{\left|\vec{R}_I-\vec{R}_J\right|}. \end{aligned} \tag{3.1}$$

$V_{\mathrm{nl}}^{\mathrm{ps}}$ and $V_{\mathrm{loc}}^{\mathrm{ps}}$ are the non–local and local total ionic potential respectively, expressed as a sum of ionic pseudopotentials; $\rho_e(\vec{r})$ is the electronic charge density, f_i the occupation numbers of electronic states, Z_v is the valence charge density of the atoms, and E_{xc} the exchange–correlation energy functional expressed within LDA.

The simulation cell is periodically repeated to infinity and, as a consequence of the

periodicity, the electronic wave–functions can be expanded in plane–waves. [1] Considering the Γ–point representation of the Brillouin zone (which will be our practical choice), a generic wave–function is written as:

$$\psi_h(\mathbf{r}) = \frac{1}{\sqrt{\Omega}} \sum_{\mathbf{G}} c_h(\mathbf{G}) e^{i\mathbf{G}\cdot\mathbf{r}}. \tag{3.2}$$

The basis set for the expansion in Eq. 3.2 is reduced to a finite set by truncating the sum over G to include only those plane–waves with a kinetic energy $K = \frac{1}{2}\mathbf{G}^2$ less than a given energy E_{cut}. (Atomic units are used in the following.) It is clear that the choice of E_{cut} determines the accuracy of the calculation of the DFT energy, and its value depends on the specific system.

Since we use plane–waves, it is much more convenient to evaluate all terms of Eq. 3.1, except the last two, in Fourier space [19]. In order to calculate $\partial E/\partial \mathbf{h}$ as described in previous section, we must isolate the dependence of E on h also in Fourier space. It is therefore useful to introduce the *scaled* reciprocal vectors, *i.e.* the reciprocal vectors of the unitary cube:

$$\mathbf{q} = 2\pi \begin{pmatrix} h \\ k \\ l \end{pmatrix}, \qquad h, k, l \text{ integers}, \tag{3.3}$$

where h, k, l are the Miller indices of the time–varying super–cell. Consider now the reciprocal vector in *real* variables:

$$\mathbf{G} = h\mathbf{b}_1 + k\mathbf{b}_2 + l\mathbf{b}_3. \tag{3.4}$$

[1] About the convenience of the choice of plane–waves as basis set we refer the reader to literature, for example Ref. [19] and references therein.

From the definitions of primitive reciprocal vectors $\mathbf{b}_i$ and of $\mathbf{h}$ (Eq. 2.1), $\mathbf{G}$ is related to $\mathbf{q}$ by:

$$\mathbf{G} = (\mathbf{h}^t)^{-1}\mathbf{q}, \tag{3.5}$$

which is the transformation law of coordinates in reciprocal space. Note that from Eq. 2.2 and Eq. 3.5 we have:

$$\mathbf{G} \cdot \mathbf{r} = \mathbf{q} \cdot \mathbf{s}. \tag{3.6}$$

Hereafter, each time scaled and real coordinates are mixed in equations, these are related by the previous transformation laws. Using Eqs. 2.2, 2.19 and 3.6 it is easy to get the transformation for wave–functions in Fourier space:

$$c_h(\mathbf{G}) = \frac{1}{\sqrt{\Omega}} \int \mathrm{dr}\, \mathrm{e}^{-i\mathbf{G}\cdot\mathbf{r}} \psi_h(\mathbf{r}) = \int \mathrm{ds}\, \mathrm{e}^{-i\mathbf{q}\cdot\mathbf{s}} \psi(\mathbf{s}) = c(\mathbf{q}). \tag{3.7}$$

As expected $c_h(\mathbf{G})$ are invariant under scale transformation. They are in fact the electronic degrees of freedom in Fourier space, whose equations of motion from Eq. 2.23 are therefore the same in real or in scaled variables.

We have now all the basic ingredients to evaluate the explicit formulas for the stress tensor $\Pi = -\frac{1}{\Omega}(\partial E/\partial \mathbf{h})\mathbf{h}^t$. The calculations are quite straightforward but boring in some cases and we address the reader to the Appendix 6.1 for the complete set of formulas, as implemented in our *FORTRAN* code, and for the mathematical details. The implicit expression for Π obtained deriving Eq. 3.1 with respect to $\mathbf{h}$ in the reciprocal space formalism (see Appendix 6.1) is:

$$\begin{aligned}\frac{\partial E}{\partial \mathrm{h}_{\alpha\gamma}}\mathrm{h}^t_{\gamma\beta} &= -\sum_i f_i \sum_{\mathbf{q}} |c_i(\mathbf{q})|^2 \mathrm{G}_\alpha \mathrm{G}_\beta + \frac{\partial E^{ps}_{nl}}{\partial \mathrm{h}_{\alpha\gamma}}\mathrm{h}_{\gamma\beta} \\ &- \Omega \sum_{\mathbf{q}\neq 0} \rho^*_e(\mathrm{G}) S(\mathrm{G}) \left(\frac{\partial v_{loc}(|\mathrm{G}|)}{\partial G^2} 2\mathrm{G}_\alpha \mathrm{G}_\beta + v_{loc}(|\mathrm{G}|)\delta_{\alpha\beta} \right) \qquad (3.8) \\ &+ \frac{1}{2}(4\pi)\Omega \sum_{\mathbf{q}\neq 0} \frac{|\rho_t(\mathrm{G})|^2}{|\mathrm{G}|^2} \left(\frac{\mathrm{G}_\alpha \mathrm{G}_\beta}{|\mathrm{G}|^2} - \delta_{\alpha\beta} \right) + \int \mathrm{d}\mathbf{r} \left[\epsilon_{xc}(\rho_e(\mathbf{r})) - v_{xc}(\mathbf{r}) \right] \rho_e(\mathbf{r}) \delta_{\alpha\beta} \\ &- \frac{1}{2} \sum_I \sum_{J\neq I} \frac{Z_v^2}{|\mathbf{R}_I - \mathbf{R}_J|^3} (\mathrm{R}^\alpha_I - \mathrm{R}^\alpha_J)(\mathrm{R}^\beta_I - \mathrm{R}^\beta_J).\end{aligned}$$

$S(\mathrm{G})$ is the atomic structure factor, v_{loc} the spherically symmetric local potential ($V^{ps}_{loc}(\mathbf{r}) = \sum_I v_{loc}(|\mathbf{r} - \mathbf{R}_I|)$). ϵ_{xc} and v_{xc} are the exchange and correlation energy and potential given by LDA [18], and E^{ps}_{nl} the contribution of V^{ps}_{nl} to the energy of Eq. 3.1. Eq. 3.8 coincide with the expression obtained by Nielsen and Martin [23] and gives, as discussed at the end of the previous chapter, the quantum–mechanical stress tensor in LDA–DFT.

In Eq. 3.8 the expression for the contribution of the non–local pseudopotential is written in implicit form. In the next section we discuss the main differences in the calculation of stress tensor between the two classes of pseudopotentials we implemented in our method: the "standard" well–known norm–conserving pseudopotentials of Bachelet–Hamann–Schlüter [26], and the more recent ultra–soft pseudopotentials of Vanderbilt [29].

3.1 Norm–Conserving Pseudopotentials

The norm–conserving pseudopotentials (NC–PP) are defined by a non–local and a local part, which enter in $V^{\mathrm{ps}}_{\mathrm{nl}}$ and $V^{\mathrm{ps}}_{\mathrm{loc}}$ of Eq. 3.1 respectively [26]. The norm–conservation constraint on the atomic pseudo–wavefunctions allows one to write the electronic charge

density as:

$$\rho_e(\mathbf{r}) = \sum_i^{occ} f_i \, |\psi_i(\mathbf{r})|^2 \, . \tag{3.9}$$

Its dependence on $\mathbf{h}_{\alpha\beta}$ is simply given by the scaling law Eq. 2.20, which states that the product $\Omega\rho_e(\mathbf{r})$ is invariant. Thus:

$$\frac{\partial \rho_e(\mathbf{r})}{\partial \mathbf{h}_{\alpha\beta}} = -\rho_e(\mathbf{r})(\mathbf{h}^t)^{-1}_{\alpha\beta}. \tag{3.10}$$

Let us consider the second term in the first integral of Eq. 3.1. The operator $V_{\rm nl}^{\rm ps}$ is written as:

$$V_{\rm nl}^{\rm ps} = \sum_I v_{\rm nl}(\mathbf{r} - \mathbf{R}_I), \tag{3.11}$$

where

$$v_{\rm nl}(\mathbf{r}) = \sum_l v^l(\mathbf{r})|l\rangle\langle l|. \tag{3.12}$$

$|l\rangle$ is the eigenstate of momentum l, and the sum runs from zero to infinity. Let v_{l_m} be the non–local pseudopotential acting on the state with highest angular momentum treated in the non–local form, which means that $v_l = v_{l_m}$ for $l \geq l_m$, and $\delta v_l = v_l - v_{l_m}$; $v_{\rm nl}$ becomes:

$$v_{\rm nl} = v_{l_m} + \sum_{l=0}^{l_m} \delta v_l |l\rangle\langle l|. \tag{3.13}$$

v_{l_m} may then be incorporated in the definition of the local part of the pseudopotential and one can redefine the non–local part as:

$$v'_{\rm nl} = \sum_{l=0}^{l_m} \delta v_l |l\rangle\langle l|. \tag{3.14}$$

In order to calculate the scalar product $\langle\psi_i|v'_{\rm nl}|\psi_i\rangle$ in Eq. 3.1, it is more convenient to use the Kleinman–Bylander fully non–local separable form [30] for $v'_{\rm nl}$:

$$v'_{\rm nl} = \sum_{l,m} \frac{|\delta v_l \phi_{lm} Y_{lm}\rangle\langle Y_{lm}\phi_{lm}\delta v_l|}{\langle\phi_{lm}|\delta v_l|\phi_{lm}\rangle}, \tag{3.15}$$

where $\phi_{lm}(r)$ is the atomic radial pseudo–wavefunction corresponding to v_l, Y_{lm} is the spherical harmonic function with indices l, m. [2] The corresponding energy in Eq. 3.1 is:

$$E_{\rm nl} = \sum_i f_i \sum_{lm} \langle\phi_{lm}|\delta v_l|\phi_{lm}\rangle^{-1} \sum_I \langle\psi_i|\xi^I_{lm}\rangle\langle\xi^I_{lm}|\psi_i\rangle, \tag{3.16}$$

where $|\xi^I_{lm}\rangle$ denotes the state $|\delta v_l \phi_{lm} Y_{lm}\rangle$ centered on ion in $\mathbf{R}_I$. Since $\langle\phi_{lm}|\delta v_l|\phi_{lm}\rangle^{-1}$ is invariant under cell transformations, the only contribution of this energy to the stress tensor is coming from the derivative of the scalar product $\langle\xi^I_{lm}|\psi_i\rangle$. All the details are given in the Appendix 6.1.

3.2 Ultra–soft Pseudopotentials

In this section we briefly describe the ultra–soft pseudopotentials (US-PP) and point out the most relevant differences with the norm–conserving scheme. In his paper [29] Vanderbilt has proposed a pseudopotential scheme where the norm–conservation condition has been relaxed. This allows to obtain pseudo-wavefunctions to be as soft as possible within the core region, yielding a significant reduction of the cut–off energy (E_{cut}) required to describe them. Moreover, the scattering properties of such pseudopotentials

[2] Physical properties of Kleinman–Bylander pseudopotentials are similar to those of Hamann–Schlüter–Chang form [25] (Eq. 3.14), a part the possible presence of "ghost states", which can destroy important physical properties of the atoms if the procedure is not applied cautiously [31].

are, by construction, correct at several energies spanning the range of occupied states and the transferability can be systematically improved by increasing the number of such energies. With the new recipe of Vanderbilt several elements of the Periodic Table become accessible for practical total energy calculations with plane–wave expansion of electronic wavefunctions. In particular compounds with first–row elements, transition metals and oxygen became possible candidates for first–principle MD studies.

The relaxation of the norm–conservation condition adds some complications to the derivation of the Euler–Lagrange equations of motion (Eqs. 2.23–2.25), with new terms appearing in the description of the forces acting on ions and of the internal stress tensor. The US–PP has been efficiently implemented in the original Car–Parrinello scheme for constant volume Molecular Dynamics by Laasonen *et al* [32, 33]. We refer to their papers for the expression of the forces acting on wave–functions (in Eq. 2.23) and ions (in Eq. 2.24), focusing here our attention on the derivation of stress tensor within this pseudopotential scheme.

The softness of the new pseudopotentials is accompanied by the complication of the pseudopotential definition, with the introduction of a generalized orthonormality condition. In order to recover the full electronic charge, the electron density in Eq. 3.9 has to be augmented by appropriate functions in the core region:

$$\rho_e(\mathbf{r}) = \rho_e^{soft}(\mathbf{r}) + \rho_e^{hard}(\mathbf{r}), \tag{3.17}$$

where:

$$\rho_e^{soft}(\mathbf{r}) = \sum_i f_i \psi_i^*(\mathbf{r})\psi_i(\mathbf{r}), \tag{3.18}$$

$$\rho_e^{hard}(\mathbf{r}) = \sum_i f_i \sum_{nn',I} Q^I_{nn'}(\mathbf{r}) \langle \psi_i | \beta^I_n \rangle \langle \beta^I_{n'} | \psi_i \rangle, \tag{3.19}$$

and:

$$\beta^I_n(\mathbf{r}) = \beta_n(\mathbf{r} - \mathbf{R}_I), \tag{3.20}$$

$$Q^I_{nn'}(\mathbf{r}) = Q_{nn'}(\mathbf{r} - \mathbf{R}_I). \tag{3.21}$$

$\beta^I_n(\mathbf{r})$ and $Q^I_{nn'}(\mathbf{r})$ are arbitrary functions centered on the atomic coordinates and strictly localized in the core region. In particular β_n is an angular momentum eigenfunction in the angular variables, times a radial function which vanishes outside the core region (like the functions ξ_{lm} introduced in the previous section for the Kleinman–Bylander scheme). The non–local and the local part of the pseudopotential are respectively defined as:

$$V^{\rm ps}_{\rm nl} = \sum_{nn',I} D^0_{nn'} |\beta^I_n\rangle \langle \beta^I_{n'}|, \tag{3.22}$$

$$V^{\rm ps}_{\rm loc}(\mathbf{r}) = \sum_I v^{ion}(\mathbf{r} - \mathbf{R}_I). \tag{3.23}$$

The indices n and n' in the previous equations run over the total number N_β of β functions. In the US–PP two reference energies, and therefore two functions β, are usually required for each included angular momentum channel. This leads to a number N_β which is generally twice as large as the number N_ξ of ξ functions in Eq. 3.15. The functions β_n, $Q_{nn'}$, v^{ion} and the parameters $D^0_{nn'}$ are obtained from first–principles [29] and characterize the atomic species (hereafter, for simplicity, we consider only one species). From Eq. 3.22 one can see that the US–PP take the form of a few separable terms very similar to Kleinman–Bylander–type (Eq. 3.15), with the states $|\xi^I_{lm}\rangle$ substituted by the new states $|\beta^I_n\rangle$ and the non–diagonal constant matrix $D^0_{nn'}$ replacing the diagonal term $\langle \phi_{lm} | \delta v_l | \phi_{lm} \rangle^{-1}$. Using

Eq. 3.22 the non–local contribution to total energy (Eq. 3.1) is:

$$E_{\rm nl} = \sum_i f_i \sum_{nn'} D^0_{nn'} \sum_I \langle\psi_i|\beta^I_n\rangle\langle\beta^I_{n'}|\psi_i\rangle, \tag{3.24}$$

which has to be compared with Eq. 3.16.

The relaxation of the norm–conservation condition is achieved by introducing a generalized orthonormality condition [29]:

$$\langle\psi_i|\hat{S}(\{\mathbf{R}_I\})|\psi_j\rangle - \delta_{ij} = 0, \tag{3.25}$$

which substitutes the ordinary orthonormality constraints in Eq 2.21. $\hat{S}$ is a Hermitian overlap operator given by:

$$\hat{S} = 1 + \sum_{nn',I} q_{nn'}|\beta^I_n\rangle\langle\beta^I_{n'}|, \tag{3.26}$$

where $q_{nn'} = \int d\mathbf{r} Q_{nn'}(\mathbf{r})$. The orthonormality condition Eq. 3.25 is consistent with the conservation of the charge [29]. Note that the overlap operator $\hat{S}$ depends on the ionic positions through the functions $|\beta^I_n\rangle$.

Due to the $\mathbf{h}$ dependence of functions $Q_{nn'}$ (through $(\mathbf{r}-\mathbf{R}_I) = h(\mathrm{s}-\mathrm{S}_I)$) and of scalar products $\langle\psi_i|\beta^I_n\rangle$, the derivative of ρ_e^{hard} (Eq. 3.19) with respect to $\mathbf{h}_{\alpha\beta}$ is not as simple as that given by Eq. 3.10. This fact introduces new terms in the expression for $\partial E/\partial h$. The only contribution which remains the same in US–PP as in norm–conserving scheme is the kinetic energy contribution. Moreover the dependence of the new orthonormality constraints (Eq. 3.25) on $\mathbf{h}_{\alpha\beta}$ adds to the stress tensor a term which takes into account the change in the constraints with a change of $\mathbf{h}$. The internal stress tensor has thus the

form:

$$\Pi_{\alpha\beta} = -\frac{1}{\Omega}\left(\frac{\partial E}{\partial \mathbf{h}_{\alpha\gamma}} - \sum_{ij}\Lambda_{ij}\frac{\partial}{\partial \mathbf{h}_{\alpha\gamma}}\langle\psi_i|\hat{S}|\psi_j\rangle\right)\mathbf{h}^t_{\gamma\beta}. \tag{3.27}$$

The explicit expressions for all the quantities introduced in this section are given in Appendix 6.1, together with the formulas for the contribution of the various energy terms to internal stress.

Due to the presence of ρ_e^{hard} and to the fact that N_β is generally twice as large as N_ξ, the stress tensor calculation is more costly for US–PP than for NC–PP. In Appendix 6.2 we discuss the computational effort needed to calculate total energy, forces and stress with the two types of pseudopotentials. We anticipate here the convenience criterion for choosing between them in the case of standard fixed–cell CP and in the case of our extension to variable–cell. For fixed–cell CP the use of US–PP becomes advantageous [32] when it is possible to use a kinetic energy cut–off E_{cut}^{US} such that:

$$E_{cut}^{US} < \frac{1}{2^{2/3}}E_{cut}^{NC}. \tag{3.28}$$

This inequalitiy is easily satisfied for first–row elements, transition metals and other elements like oxygen [32, 33, 34, 35]. However, as shown in Appendix 6.2, when the calculation of stress tensor is needed, as in our variable–cell CP, this criterion becomes more strict:

$$E_{cut}^{US} < \frac{1}{3}E_{cut}^{NC}. \tag{3.29}$$

3.3 Constant Cut–off or Constant Number of PW?

To conclude this chapter, we will point out some considerations about the well known problems arising from using a finite basis set of plane–waves in the expansion of Eq. 3.2.

Plane–waves are very appealing, because they are independent of the structure of the system, and systematic improvements of the quality of the basis set can be simply done by increasing the number of Fourier components. Furthermore, fast Fourier transform techniques can be adopted in the practical calculation of E. The difficulty encountered when using plane–waves is mainly related to the problem of convergence in Fourier space, i.e. to the question: how small cut–off energy E_{cut} will suffice in order to shrink the errors due to a finite Fourier series to negligible values?

In the present case we are interested in performing calculations of DFT functional E, while the simulation cell varies in shape and volume. This implies that the set of plane–waves with kinetic energy less than E_{cut} varies according to the change of $\mathbf{G}$–vectors. In the CP method, however, the plane–wave coefficients in the representation of wave–functions are the actual lagrangian electronic degrees of freedom, and their number N_{pw} is kept constant during the simulation, because variable number of degrees of freedom is highly undesirable in Molecular Dynamics. This implies that wave–functions, charge densities and potentials appearing in the functional E are resolved with variable precision. Let us imagine for simplicity an isotropic volume change of the cell. If the volume decreases and N_{pw} remaines constant, the effective energy cut–off will become higher and higher and the corresponding curve E versus volume will be distorted with respect to an analogous curve calculated with constant E_{cut}. These discrepancy gives, for instance, different static equilibrium properties. Although in principle both this curves are wrong, and only at convergence in Fourier space they will coincide with the correct one, the most common experience [36, 1] shows that when choosing a constant E_{cut} procedure the incomplete

convergence leads to much smaller errors in the static equilibrium parameters. Working at constant cut–off would be then preferable.

In order to recover the accuracy of a constant E_{cut} calculation in a constant N_{pw} simulation we have modified the kinetic term of the DFT functional (Eq. 3.1) as follows [37].

Considering only the Γ point of the Brillouin zone of the simulation cell, the kinetic energy is:

$$E_{ke} = \frac{1}{2}\sum_{i=1}^{M} f_i \sum_{\mathbf{q}} G^2 c_i^*(\mathbf{q}) c_i(\mathbf{q}), \tag{3.30}$$

where $c_i(\mathbf{q})$ are the Fourier coefficients of $\psi_i(\mathbf{s})$, $\mathbf{q}$ are scaled reciprocal vectors (Eq. 3.3), and $\mathbf{G} = (\mathbf{h}^t)^{-1}\mathbf{q}$. The set of $\{\mathbf{q}\}$ is fixed at the beginning of the simulation. We replace the kinetic factor G^2 in (3.30) by an expression which forces zero occupancy for those plane waves whose kinetic contribution $\frac{1}{2}G^2$ exceeds E_{cut}. This is done by adding to G^2 a smooth step function of height A and width σ, so that:

$$G^2 \rightarrow G^2 + A\left[1 + \mathrm{erf}\left(\frac{\frac{1}{2}G^2 - E_0}{\sigma}\right)\right]. \tag{3.31}$$

In the $A \rightarrow 0$ limit, the constant N_{pw} results are recovered. In the opposite $\sigma \rightarrow 0$, $A \rightarrow \infty$ limit, all plane waves with $\frac{1}{2}G^2 > E_0$ drop out of the ground-state wave function, therefore mimicking a constant E_{cut}. The optimum practical choice lies somewhere in between these two extrema, since one would like to work as close as possible to the constant E_{cut}, while avoiding unphysical discontinuities. Making $A > 0$ introduces an additional term in the stress tensor. In the large-A limit this extra term corresponds to the so called Pulay stress [36], i.e. the difference between the stress tensor calculated using $\frac{\partial E}{\partial h}$, which corresponds in any case to *locally constant* number of plane waves derivative, and the

"true" (constant cut-off) stress. In practice we obtain even for finite A a good estimate for the Pulay stress, which allows to calculate the correct stress for a given configuration of the system with a much modest effort than that required by standard E_{cut} procedure, where more calculations at different volumes are needed.

Since the set of plane waves is fixed at the beginning of the simulation, their number should be large enough for this trick to be reasonably accurate. The modification of the kinetic energy (Eq. 3.31) increases by a factor $\frac{A}{E_{cut}} + 1$ the energy E_{max} of the highest unoccupied state in the Hilbert space defined by the basis set. Since the time step for the integration of the equation of motion (Eq. 2.23) scales as $(E_{max})^{-\frac{1}{2}}$ (see Eq. 2.18), the value of A should be kept as low as possible.

We have tested this method on carbon which, due to the hardness of its pseudopotential, is known to be particular sensitive to the basis set choice. For our test, whose results are reported in Fig. 3.1, we have used a conventional cubic cell for diamond with two carbon atoms, Γ–point sampling of the BZ, and Bachelet–Hamann–Sclüter [26] pseudopotential in the Kleinman–Bylander form [30]. We find that the constant-N_{pw} equilibrium lattice constant and bulk modulus with $N_{pw} = 12789$ (corresponding to $E_{cut} \simeq 40$ Ry for a cell–volume of 75.5 a.u.) differ from the same quantities computed at constant cut-off by 3 % and 36 % respectively. With our method, using $A = 200$ Ry, $\sigma = 2$ Ry and $E_0 = 40$ Ry in Eq. 3.31, the lattice constant and the bulk modulus differ only by 0.5% and 1% from those computed at constant cut-off. Note in Fig. 3.1 that the Pulay stress affecting the value of the stress calculated with the constant–N_{pw} procedure is of about 400 Kbar at the "true" equilibrium volume and reduces drastically to about zero using the modified

kinetic energy functional.

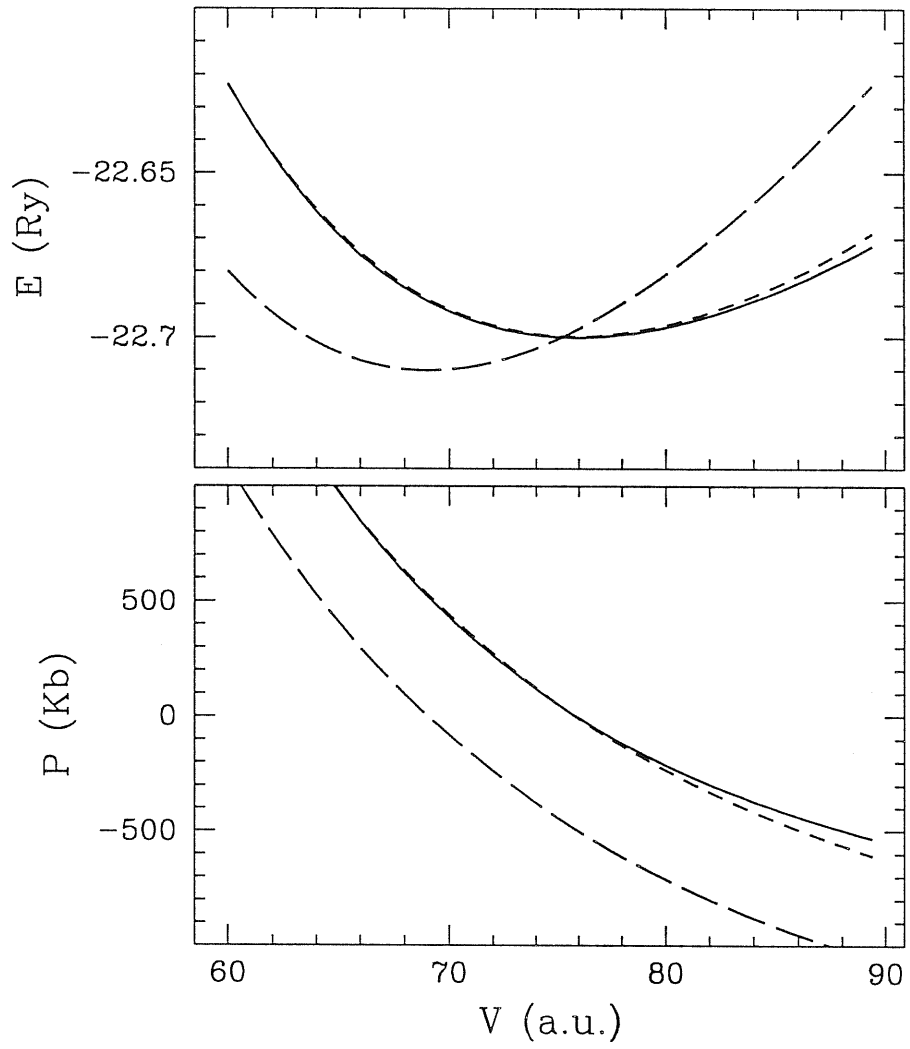

Figure 3.1: Energy versus volume (upper panel) and pressure versus volume (lower panel) for carbon–diamond in three different calculations: at constant E_{cut} = 40 Ry (solid line), with the modified kinetic energy (Eq 3.31) (short–dashed line), and with constant number of plane–waves N_{pw} (dashed line). For the parameters used see text.

4 Applications

4.1 Structural Phase Transformation in Silicon

We have tested our method by simulating a pressure induced transition in Silicon [38]. Silicon has been chosen as the test case since the physics underneath the Si phase diagram is well understood and established. For this reason in this section we devote a longer space to technical details and difficulties posed by a simulation of this kind than to the discussion os Si pressure dependent properties. Si has a quite complicated phase diagram with many high pressure phases. Studies of this phase diagram have challenged both theorists and experimentalists over the last ten years. Thanks to many different experiments based on x–rays spectroscopy, the phase diagram of Si at room–temperature is well-known up to pressures of about 250 GPa [39, 40]. The experimental sequence up to 30 GPa is: diamond (D) $\rightarrow$ β-Sn $\rightarrow$ sh, with transition pressures at 11 and 13-16 GPa respectively [40]. Simple hexagonal structure is then found to be stable up to 35-40 Gpa. The domain of stability of β-Sn is very narrow in contrast with those of D and sh. The existence of an intermediate stable orthorhombic phase between β–tin and sh has also recently been claimed [41].

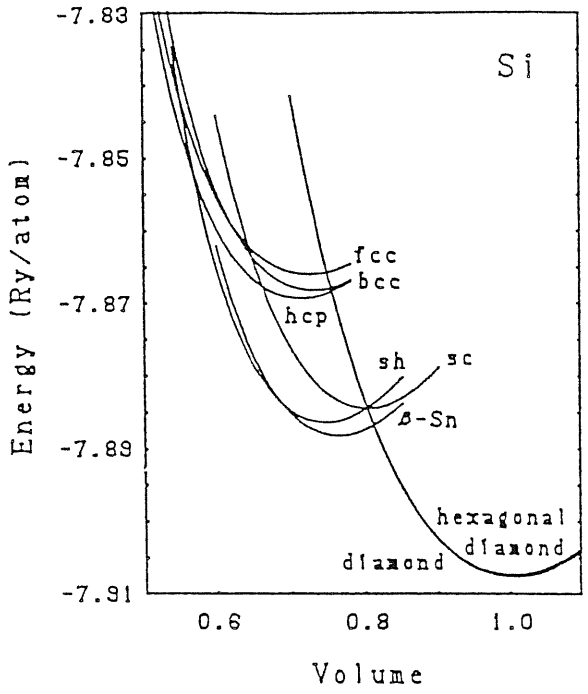

Figure 4.1: Total structural energy vs. volume (normalized by the calculated equilibrium volume in D structure). The data come from LDA total energy calculations (Ref. [43]).

Other experimental findings [42] show however that, if the pressure increase is applied at low temperatures, the β–tin phase is skipped, with the system moving directly to sh phase. Other more compact phases appear at considerably higher pressures [39] but they will not be investigated in the present work. The transition pressures calculated with standard zero temperature LDA total energy calculations [43, 44] for the different phases essentially reproduce the experimental values. In Fig. 4.1 are plotted the LDA equations of state energy vs. volume for different phases, as calculated in Ref. [43]. The calculated equilibrium energy difference between diamond and the other two phases (β–tin and sh) is relevant, about 20 mRy/atom. The volume reduction during the first–order transition D$\rightarrow$ β–tin is of about 20 %. while that during the transition β–tin$\rightarrow$sh is much

smaller. Silicon is an insulator in the diamond phase, while the high–pressure phases are metallic. The transition we are interested in is thus a metal–insulator transition, with a relevant rearrangement of the electronic structure (*i.e.* the charge distribution giving rise to chemical bonds). For this reason we expect that only a method in which the electronic structure is calculated self–consistently will be able to describe at the same level of accuracy all the different phases.

To perform the simulation we used an *ab–initio* pseudopotential of the Kleinman–Bylander [30] form, constructed from the tables of Ref. [26] retaining only s–nonlocality. Wave–functions were expanded in plane waves up to a kinetic energy cut–off of 12 Ry, using only the Γ point of the super–cell Brillouin zone (BZ) in the K–point expansion of wave–functions. For the MD simulation the inertia parameters μ and W were fixed to the values of 300 a.u. and 4.05 Si mass respectively. In particular W was tuned in order to maximize energy exchange between the ionic degrees of freedom and the cell, which allows the equilibration of the cell degrees of freedom. The integration step was 1.45×10^{-16} s (6 a.u.). The temperature of the ions during the main part of the simulation was controlled by a Nosé thermostat [9], and when necessary (see below) the electrons were maintained close to their ground state using a second Nosé thermostat coupled to the electronic degrees of freedom, as described in section 2.2.

We started the simulation from an fcc periodically repeated cell containing 54 atoms, initially arranged in a diamond lattice. Since the choice of the starting cell is a particularly delicate problem in these kind of simulations, we devote to that a quite long digression. Due to the heavy computational cost of our quantum mechanical approach we are forced

to use simulation cells much smaller (typically containing at most one hundred atoms) than those used in classical PR. Large cells have several advantages when performing PR simulations on phase transformations. First a large number of degrees of freedom allows to move in a larger phase space, and thus to explore lower symmetry paths connecting the various phases. Moreover it reduces the presence of spurious "ghost" structures induced by boundary conditions: when correlation lengths become as large as the cell size, as they do close to phase transitions, periodic boundary conditions may induce on the system additional false constraints, leading to wrong transformations. Finally, for a phase transformation to occur it is necessary that both the starting and the final structure fit in the starting and in the final cell respectively. Due to our procedure with constant number of atoms, this is more easily achieved by using larger cells. We are thus forced in using largest possible cells. Due to computational cost, this implies the use of the Γ–point only representation of K–point summation in the calculation of the energy functional E (see Eq. 3.1). [1] Γ–point sampling is in principle exact when the cell size becomes infinite. However it gives quite poor accuracy even for cells of about 100 atoms, where several K–points of the first Brillouin zone (FBZ) of the crystal are folded onto the Γ–point of the super–cell. This poor accuracy in the energy of the various phases may produce a wrong energetic hierarchy in the energy versus volume equations of state. However transitions in PR do not proceed via phase coexistence, with the double tangent (Maxwellian) construction in the E–V plane, and thus wrong energy differences between the different phases at

[1] In terms of computational effort, the use of only Γ–point has the great advantage that wave–functions are real in direct space. This implies reduced cost in FFT with respect to complex wave–functions.

different volumes will only affect the value of the transition pressure, and not the stability of the different phases at different densities, which is indeed our main task. The value of the transition pressure is also affected by hysteresis phenomena related to our small cell size. Increasing the cell size will eventually reduce these problems, but it is too costly with present computer facilities.

It should be mentioned that K–point convergence will be different for the starting and final cells and structures. This is related not only to the possible variation of electronic band structure between initial and final phases (it is well known, for example, that K–point convergence is more severe in presence of a Fermi surface). It is also due to the possibility for the system to choose in our scheme the K–point sampling that produces the lowest energy for a given structure (K–point self–consistency). Due to the absence of variationality of E as a function of K–point representation, [2] K–point self–consistency may produce a final structure and cell having an energy even lower than the converged value. In principle simulations started with a cell having a high energy value may evolve reducing the energy by simply changing the cell shape, the final structure being the same as the starting one. When choosing the initial cell, all these considerations must be taken into account and we have exploited different strategies for different cases.

In silicon we decided to use the 54 atoms fcc repeated cell, because the K–point folding of this cell, although giving an energy per particle ~20 mRy higher than the fully converged

[2]The Hohenberg–Kohn theorem [16] holds only if the Hilbert space over which the charge density is defined is fixed. When the K–point representation is changed, which means, in our case, when the matrix h appearing in E (see Eq. 2.21) is changed, the density $\rho(\mathbf{r})$ will be represented on a different basis set, and therefore variationality is not ensured.

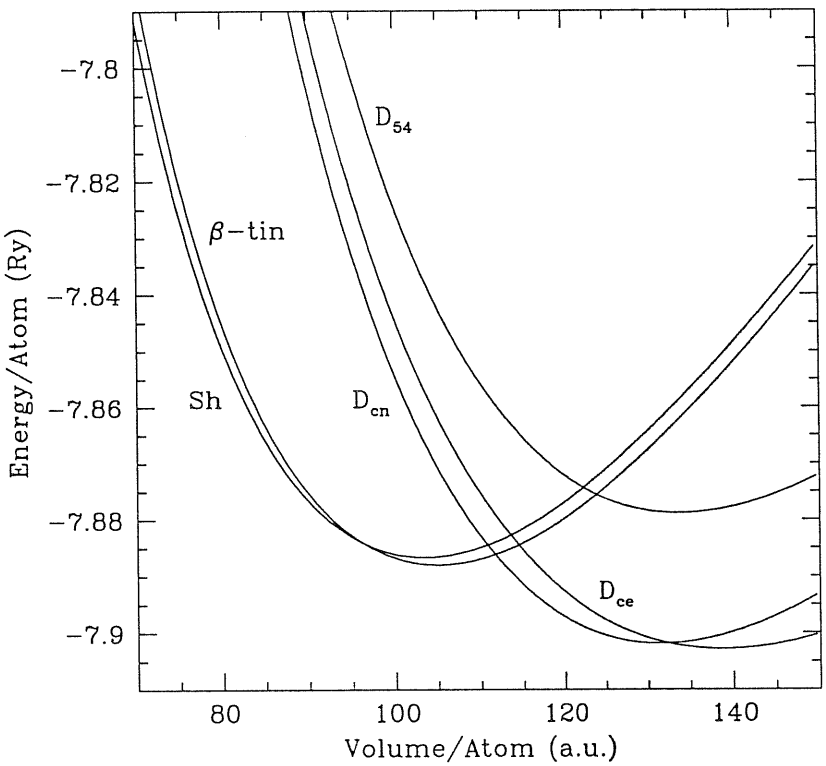

Figure 4.2: Equation of state for Si in D, β–tin and sh structure from LDA total energy calculations. D_{54} is calculated using the Γ–point representation of the fcc cell with 54 atoms. The other curves are obtained with a converged sampling of BZ. All calculations are done with constant number of plane–waves, corresponding to E_{cut}= 12 Ry for our initial cell (lattice constant for diamond: a= 5.36 Å), except D_{ce}, which is obtained with a constant cut–off calculation (E_{cut} = 12 Ry). The Pulay stress of the curve D_{cn} at the equilibrium volume of D_{ce} is of −57 Kbar and the equilibrium lattice constant calculated by D_{cn} is less than that of D_{ce} by 1.8 %.

value (as visible in Fig. 4.2), it gives the correct energy hierarchy between D and β–tin structure. The energy of the centered tetragonal β–tin structure is calculated with the guess that the final cell is obtained by rescaling the starting one along the [001] direction. If the K–point folding may in fact be constructed for the starting cell, this may only be guessed for the final one.

Another more satisfactory strategy, that we adopted in the application of graphite — diamond conversion in carbon (see section 4.2.2), is to start with a cell having the K–point folding which gives the lowest possible energy. It turns out that, for fixed volume of the supercell, the number of cells giving a different folding of the FBZ of the crystal structure over the supercell Γ–point is finite. Thus one can in principle calculate the energy for all the cells belonging to this class (or of a resonable sub–set of it), and then choose the starting simulation cell giving the lowest value. This choice reduce the problems in energy hierarchy induced by the above mentioned K–point self–consistency.

The modified energy functional in Eq. 3.31 has not been used for silicon since in this case the error introduced by working at constant number of plane waves is much smaller than the error due to the poor accuracy in BZ integration, as visible by comparing the curves labelled D_{cn} and $D_{c\epsilon}$ in Fig. 4.2. The plane–waves number was kept fixed during the simulation, and assigned by the 12 Ry cutoff with our initial cell and a lattice constant of 5.36 Å. This error, as well as that introduced by the constant plane–waves number are expected to affect only the numerical values of the transition pressures. Since a large uncertainty on the phase boundaries is anyway likely, due to the hysteresis phenomena related to our small cell and short simulation time, we have not tried to improve these

aspects of the calculation.

We started the simulation by heating our D-Si system (with fixed–cell MD) up to 300 °K. We then switched the Nosé thermostat and the constant pressure MD on, equilibrating both ions and cell degrees of freedom for $\sim$ 1 ps at zero external pressure. Skipping a possible search of the β-Sn phase, of unlikely value in view of our relatively limited accuracy and of the narrow range of stability of this phase, we directly raised the pressure from zero to a value larger than the experimental transition pressure to sh structure. This was done in steps, but without waiting for equilibration at each step, with two different pressure rates. In a first simulation we increased the pressure up to 30 GPa in an overall time of 0.4 ps (a pressure increment of about 6 GPa every 600 MD steps). In the second simulation we wanted to reproduce the results of the first one, but with a slower pressure rate: we raised the pressure to 30 GPa in about 4 ps. Although the two simulations were performed in a very different way, the crystal structures found after the transition we are going to describe are exactly the same. A comparison of the paths followed by the system during the two simulations is given in Fig. 4.3, where the energy versus volume of the system is reported, together with the Murnaghan equation of state for diamond and simple–hexagonal of Fig. 4.2. In the second simulation, after the phase transition we furthermore increased the pressure up to 60 GPa, in order to check the stability of the new phase. Since we obtained the same physical results in both cases, hereafter we refer to the first simulation, although some figures correspond to the second one. In Fig. 4.4 we plotted some quantities we monitored during MD simulations. Figure refers to second simulation. Note the behavior of kinetic energy of the cell degrees of freedom: when the

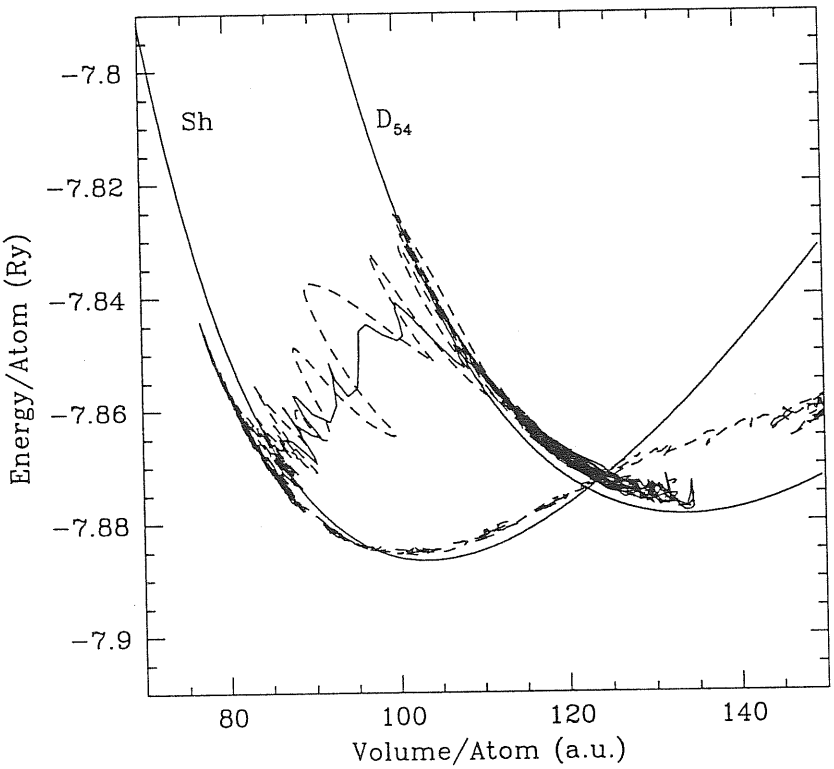

Figure 4.3: Energy vs. volume of the 54 Si system during the simulations at T= 300°K, starting from the fcc cell. Dotted line refer to first simulation, solid line to the second one. The Murnaghan equations of state for diamond (calculated using the Γ–point representation of the 54 atoms starting cell) and simple hexagonal (at K–point convergence) of Fig. 4.2 are plotted. The transition from D → sh structure is clearly visible.

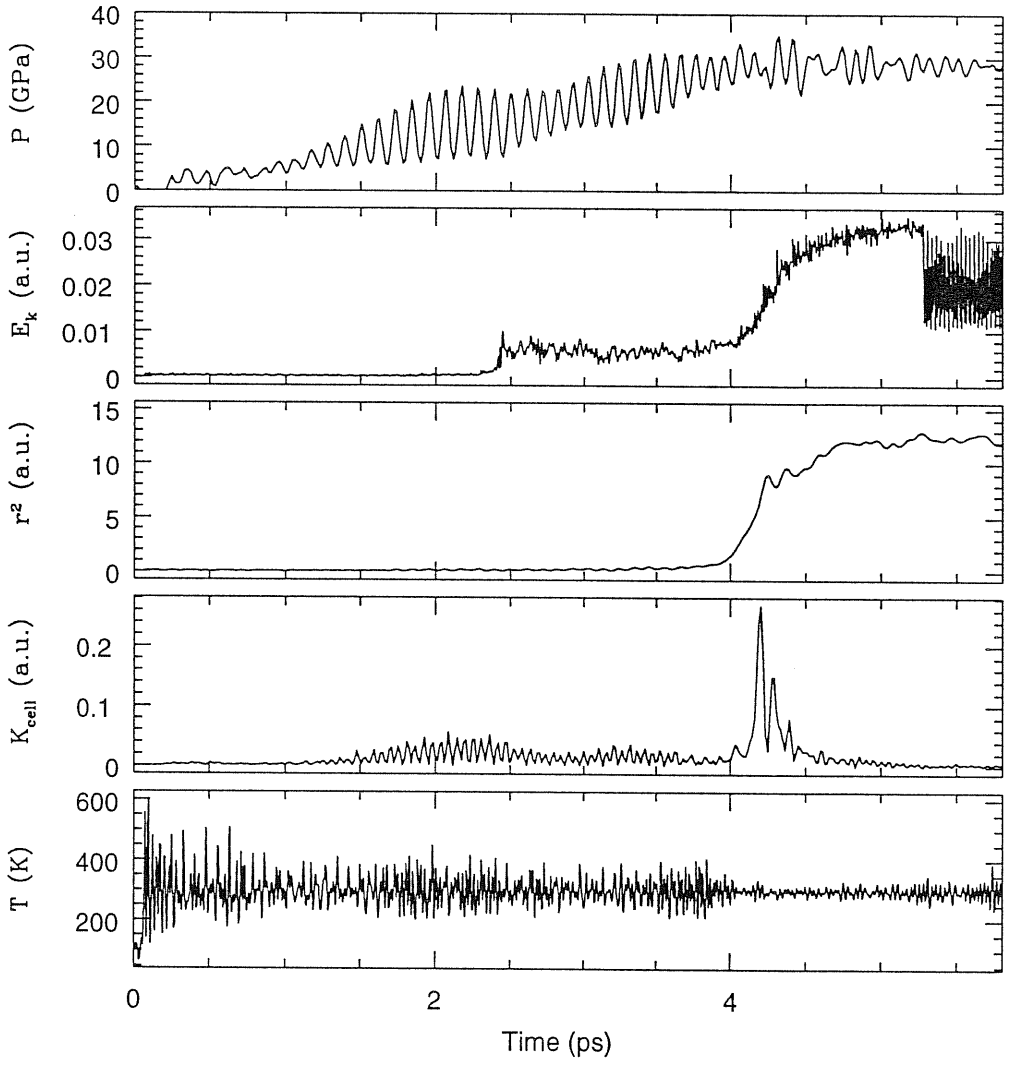

Figure 4.4: Behavior of some observables during the constant–pressure MD simulation as functions of time. The data refer to the second simulation (see text). From the bottom to the top: temperature using Nosè thermostat and $\langle T \rangle = 300$ °K, kinetic energy of the cell, mean squared displacement of the ions, fictitious kinetic energy of electronic degrees of freedom, and internal pressure, calculated as 1/3 of the trace of internal stress tensor.

transition occurs, this energy suddenly increases, due to the quick change in cell geometry. After the transition the strong coupling of the cell with the ionic degrees of freedom, induces a quenching of the cell kinetic energy, with an energy flow from the cell to the Nosè thermosthat applied to the ions. The rearrangement of atoms in a new structure is also revealed by the mean squared displacement, which raises to large values at the transition. The fictitious kinetic energy of electrons feels the change of electronic and atomic structure during the compression: the first increase visible in Fig. 4.4 corresponds to a reduction of the energy gap between lowest unoccupied and highest occupied states (see below and Fig. 4.8). At the transition the kinetic energy furthermore increases, since wave–functions follow almost adiabatically the rapid change of atomic positions and boundary conditions. The Nosé thermostat for the electrons was switched on only after the transition, with a mean kinetic energy of 0.2 a.u.

Initially the system follows the equation of state of the D structure (see Fig. 4.3) up to a pressure of about 30 Gpa. The cell edges and their relative angles oscillate isotropically for a while as a function of time (Fig. 4.5), with large volume fluctuations due to the compressive shock, following the sudden pressure increase. At that pressure a dramatic transformation spontaneously takes place. The cell undergoes a change of shape, with a drastic volume decrease from 115 to 88 a.u./atom in the overall very short time of 0.2 ps. The present behavior indicates a first order phase transition with a volume jump at constant pressure, which is very well shown by Fig. 4.6, where we report the pressure versus volume diagram. The change in shape of the cell is accompanied by radical changes in the electronic and ionic structure, transforming the initial D structure into sh. In

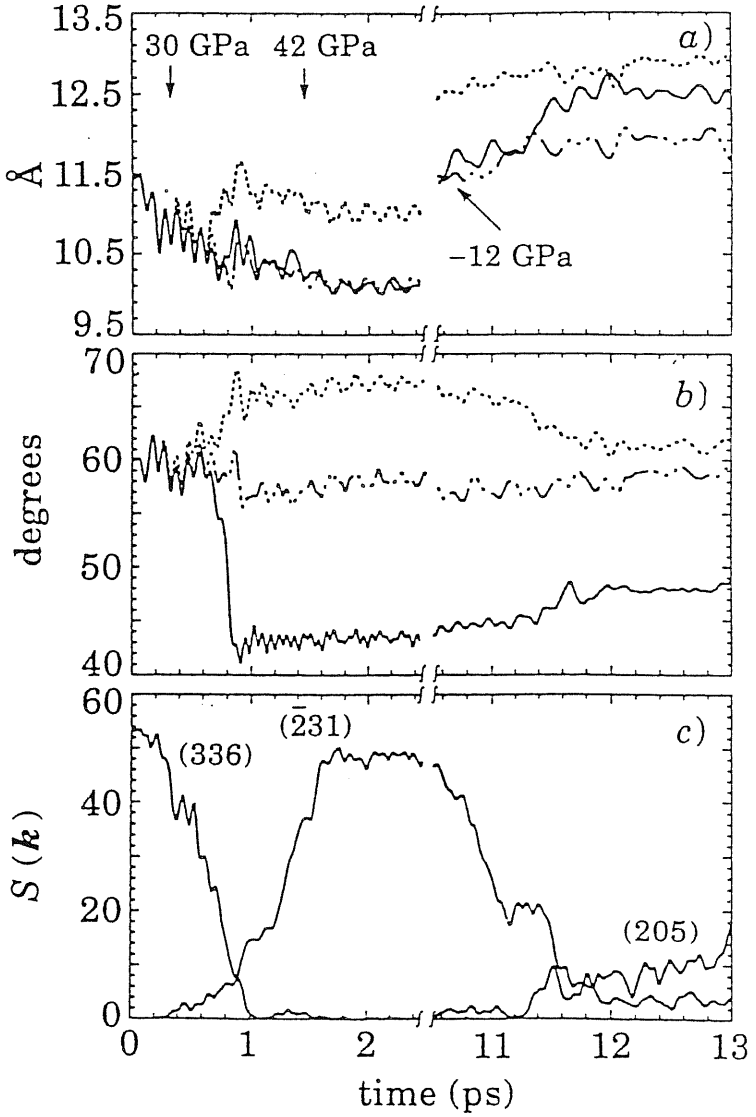

Figure 4.5: Time history of the compression and decompression MD run on Si (first simulation). Cell edges (a), their relative angles (b), and the largest peaks in the ionic structure factor (c) are shown as a function of time. The k vectors of S(k) are labelled by the Miller indices of the time–varying supercell. The arrows denote the points where the external pressure was raised to the specified value. T is 300 °K up to 11 ps where it was raised to 500 °K.

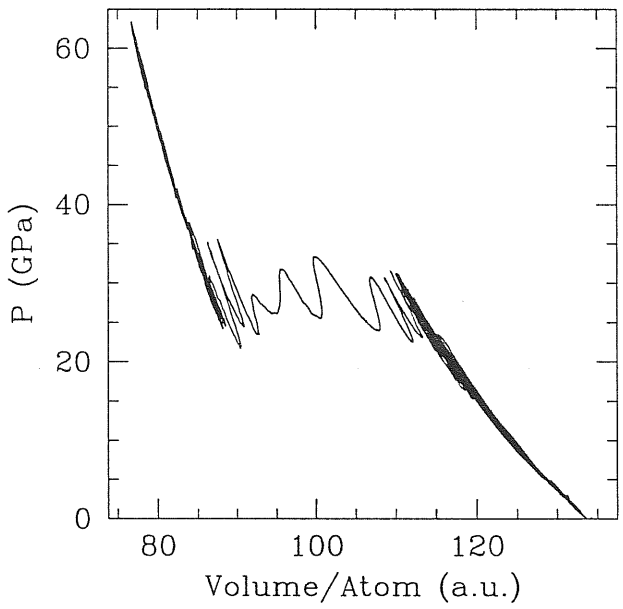

Figure 4.6: Pressure ($\frac{1}{3}$TrΠ) vs. volume (deth) diagram of Si during the compression procedure at 300 °K(second simulation run).

Fig. 4.5c we show as a function of time two peaks in the structure factors which are characteristic of the D and sh structures. It is clearly seen that the initial D structure has changed into a new one, which we will show to be sh. The transformation occurs via large, concerted, atomic motions. A simple transformation path has not so far been further rationalized. The crystal structure of the new phase is reflected in the average pair correlation function $g(r)$ and angle distribution function $f(\theta)$ reported in Fig. 4.7, both of which are only compatible with a sh structure, with $f(\theta)$ peaks at 60°, 90°, 120° and 180°. However the peaks of both $g(r)$ and $f(\theta)$ are too broad for a perfect crystal structure. Visual inspection (see Figs. 4.9– 4.12 at the end of this section) reveals defected hexagonal

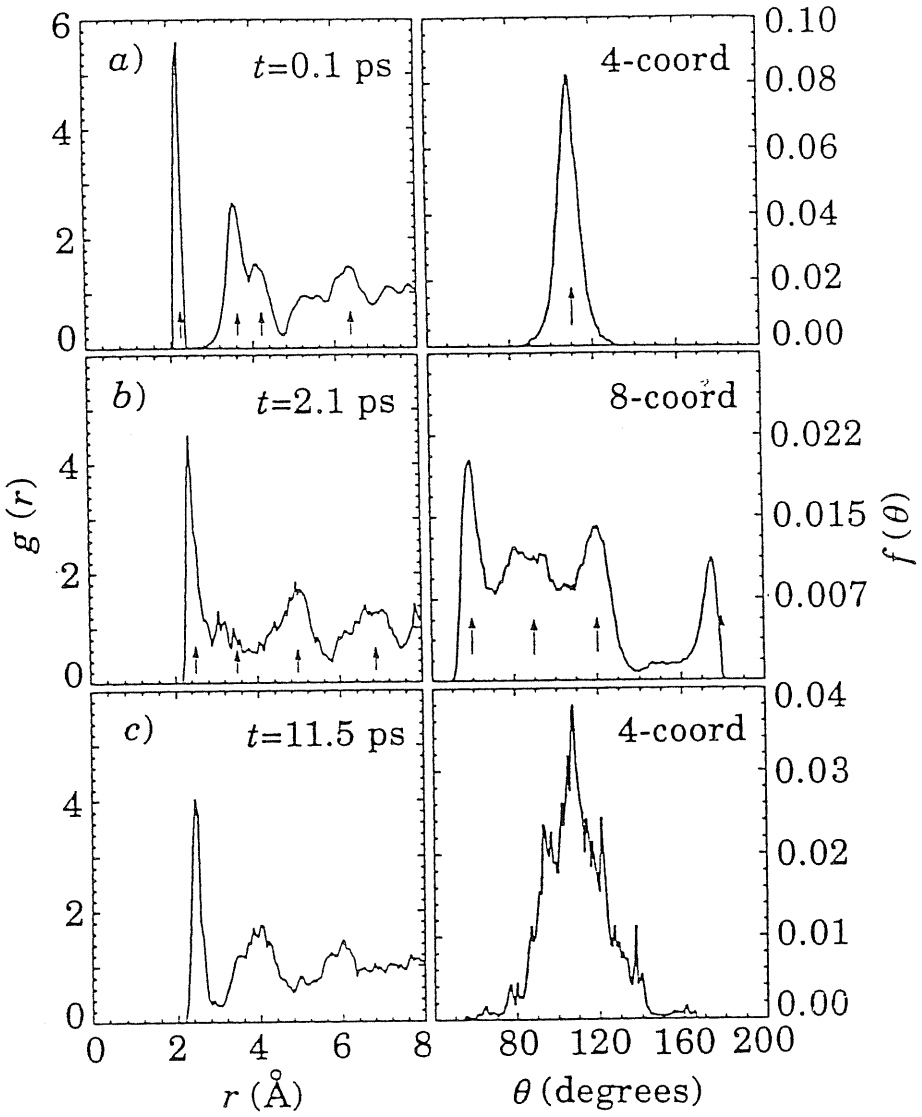

Figure 4.7: Pair correlation function $g(r)$ (left panels) and angle distribution function $f(\theta)$ (right panels) at three selected times during the MD run described in the text (first simulation). In a) and b) the arrows indicate the peaks position expected for perfect D and sh crystals respectively. $f(\theta)$ is computed including atoms with coordination four in D and a-Si structures, and coordination eight in sh structure. $g(r)$ are plotted to r larger than the half width of the simulation cell to show the effect of the cell shape on crystal structures.

planes. Interference between these planes gives rise to the strong Bragg reflection in Fig. 4.5c. These planes are however somewhat misaligned which explains the large width of the peak in $f(\theta)$ at 90^o. The defect can be seen as a missing 3–atoms segment in one of the hexagonal rows. Thus addition of three atoms should remove the defect. To prove this we have constructed an "ideal" structure compatible with the shape of the MD cell. The primitive cell in reciprocal space of this ideal crystal is constructed using three linearly independent k vectors corresponding to zero order Bragg reflections. One of the k vectors used is perpendicular to the hexagonal planes, the other two almost lye on the hexagonal planes. The "ideal" structures compatible with the form of the MD cell are all and only those generated by using allowed (linearly independent) k vectors to determine the primitive reciprocal cell. This, together with the fact that we have used k vectors giving zero order reflections guarantees that the obtained "ideal" structure is the closest to the real one. This construction gives rise to a triclinically distorted sh (9 % in plane distortion and a misalignment of about 2^o between adjacent hexagonal planes) made of 57 atoms in the original MD cell. With a further relaxation of the cell the 57 atoms crystal transforms in a perfect sh with $a = 2.52$Å and $c = 2.26$Å. [3] We have separately calculated the properties of this perfect sh and its energy is 5 mRy/atom lower than the exact value at full k-points convergence, and only 3 mRy/atom lower than the energy of the defected 54 atoms cell. It is remarkable how little is the defect energy cost. Moreover in the first run, where the pressure shock was faster, the defect appears to translate along the [010]

[3] The relaxation of the triclinically distorted sh ends up in a quasi-perfect sh (1.5 % residual distortion), if the non-spherical cutoff imposed by our constant plane waves technique is used. This residual distortion is eliminated by imposing a spherical cutoff. The a and c values given in the test refer to this latter case.

direction in the hexagonal plane with a velocity comparable to the velocity of sound. In Fig. 4.12 we report two snapshots of the same hexagonal plane at different times during the long equilibration of the cell at p= 42 GPa. The defected part of the structure is clearly visible there.

Electronic states also undergo a transition together with the D→sh structural transformation. Strikingly (Fig. 4.8) both the starting D configuration *and* the final defected sh show a gap at the Fermi level (E_F). This is at first surprising, since the perfect sh crystal is a metal with only a pseudogap just below E_F [43]. This is clearly visible in Fig. 4.8 where we report the electronic density of states for the sh perfect crystal, along with the Γ-point electronic states of the cells containing 57 atoms arranged in the triclinically distorted and perfect sh structures. As seen there, the defect in the 54 atoms cell deforms the cell enhancing the pseudogap and causing E_F to drop to the bottom of the pseudogap, in a region of very low density of states. Therefore the excellent stability of the 3-atoms defect (plus deformation) results from a kind of charge compensation – the defect is an acceptor and getters away the excess of electrons populating the high energy states. Note that to move E_F from its original value to the bottom of the pseudogap, it is necessary a defect density (3/57) that is probably unrealistic for a physical crystal at room temperature.

At this point, having obtained the D-sh conversion, it was natural to ask whether the reverse sh→D transformation could also be observed upon a decompression procedure. We therefore proceeded in reverse in the first simulation by decreasing the pressure back to zero. Wary of difficulties and metastable phases encountered by experimentalist along this path, we tried a very careful and slow decompression process, allowing the system to

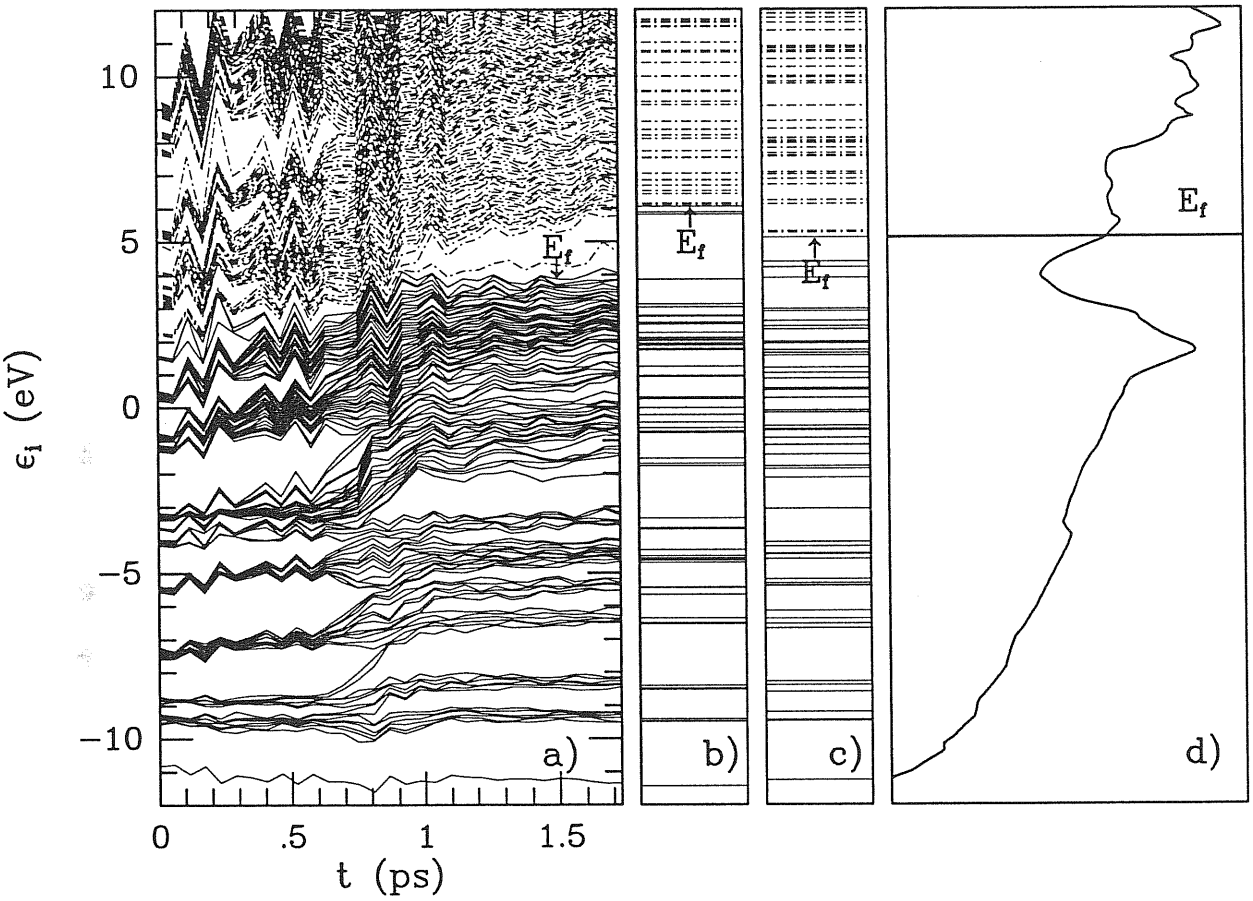

Figure 4.8: Evolution of the electronic states in the compression process. Panel a) shows the electronic states ϵ_i at the Γ point of the 54-atoms simulation cell as a function of time. The two central panels show ϵ_i at Γ of b) triclinically distorted and c) perfect sh 57-atoms cell (see text). Panel d) shows the electronic density of states relative to the potential of c). Filled states are represented with continuous lines, empty states with dash-dotted lines.

equilibrate at every intermediate step. This took ~4 ps with p decreasing from 42 GPa to -12 GPa. In this pressure range (still with T= 300 °K) very little happened to the defected sh structure, with only a gradual expansion. In a first trial we then further decreased p down to -20 GPa, which led to an explosive fragmentation of our system. In a second run, still starting from $p = -12$ GPa and T=300 °K, we instead increased T up to 500 °K and decreased the pressure slower. Here another fast transition occurred as is clearly shown by the behaviour of cell shape, as visible in the right part of Fig. 4.5. The $g(r)$ and $f(\theta)$ of this novel structure are reported in Fig. 4.7c. The $g(r)$ shows four-fold coordination and is quite similar to the original diamond $g(r)$. The width of the peak in $f(\theta)$ is however quite large ($\sim 14^{o}$), indicating that the final structure is closer to amorphous silicon than to a proper crystal. Also, other features characteristic of the D-structure became sizable (Fig 4.5c), but never quite as large as in the perfect crystal. This amorphous phase is similar to those previously obtained by first principles simulation via melt quenching [45]. It is remarkable that β–tin $\rightarrow$ a–Si transition upon decompression *and* heating has recently been observed by experimentalist [41]. Since a continous path from sh to β–tin exists, the similarity between the simulated sh $\rightarrow$ a–Si and the experimentally observed β–tin $\rightarrow$ a–Si transition is astonishing.

In view of the well known metastability and slow relaxation rates of covalent amorphous states, we were very satisfied with this result and did not attempt to anneal further to an ordered D phase.

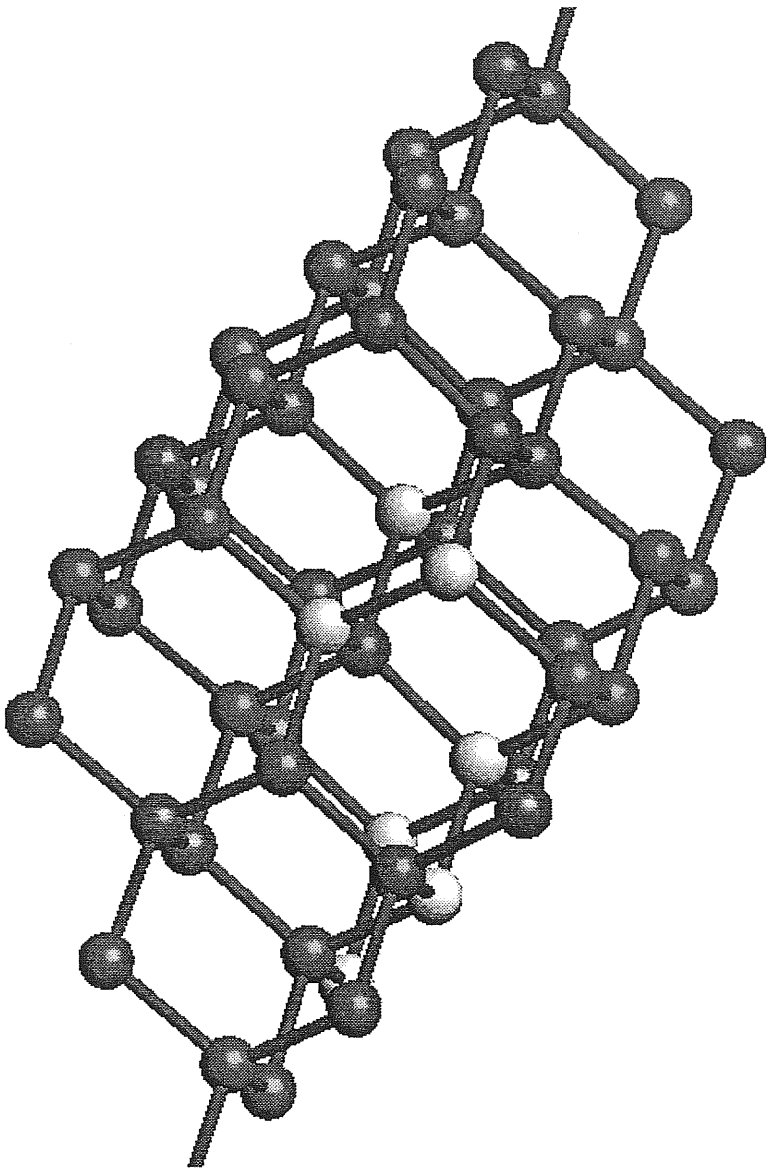

Figure 4.9: The 54 Si atoms in the starting diamond structure, arranged in the fcc simulation cell. The white balls indicate the atoms which after the transition will form a hexagon of the sh structure (see next two figures).

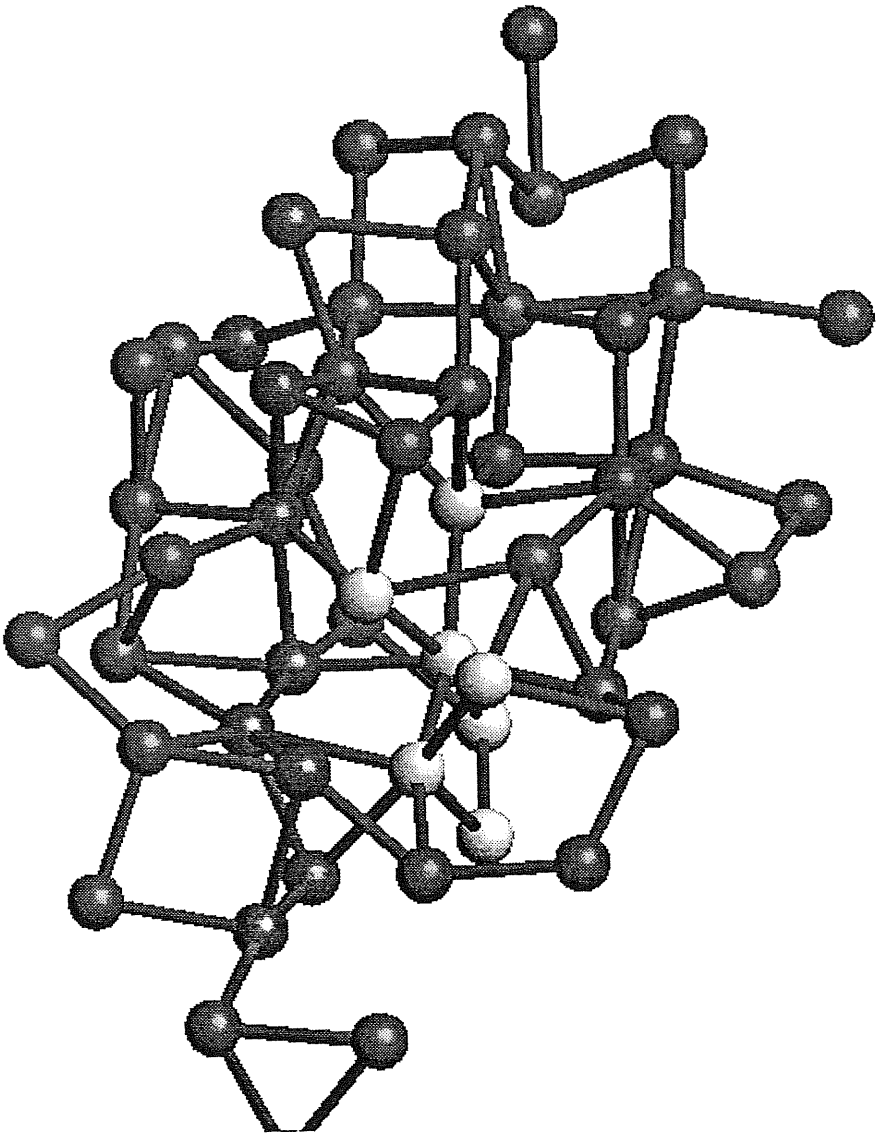

Figure 4.10: The 54 Si atoms during the fast D→sh transition.

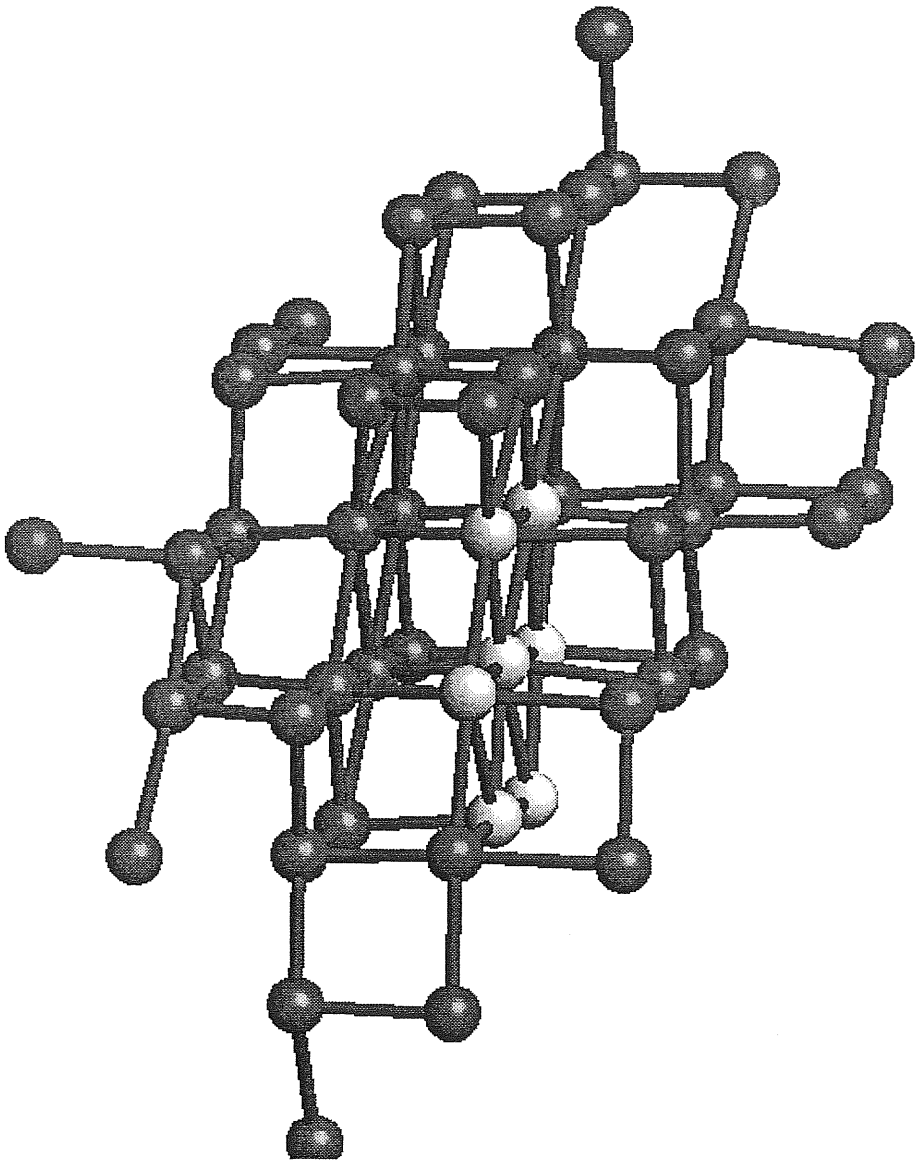

Figure 4.11: The 54 Si atoms arranged in the final defected sh structure. One can regard an the defect as a misalignment of some corresponding atoms in adjacent hexagonal planes. The point of view is the same of the two preceding figures.

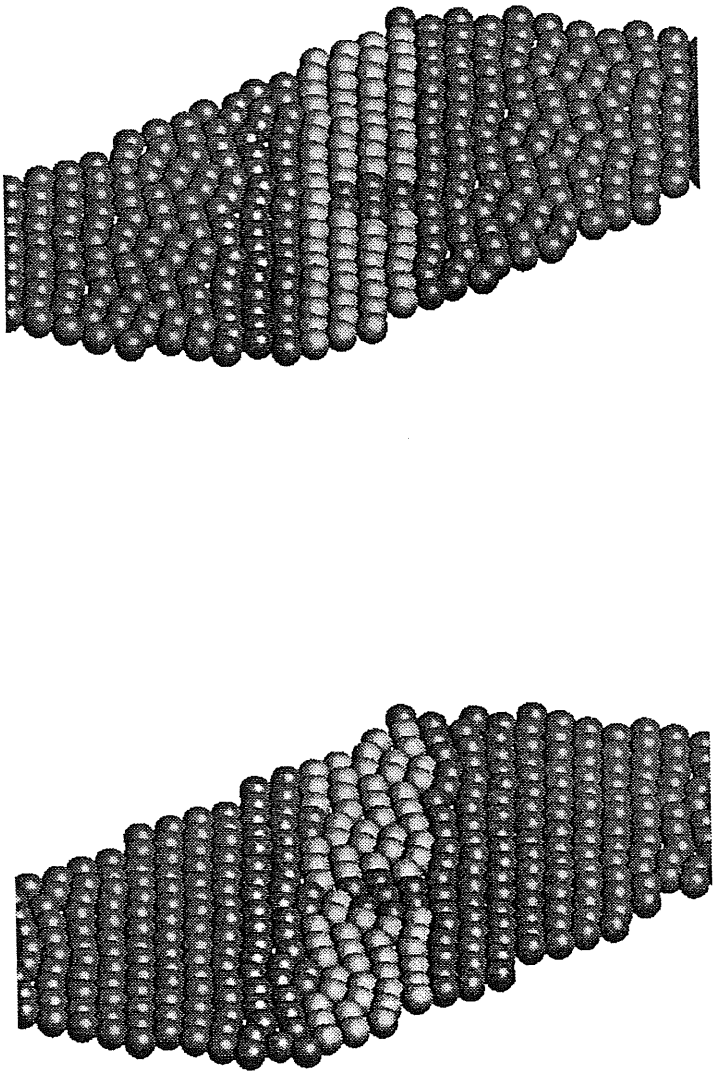

Figure 4.12: Snapshots of an hexagonal plane of the defected sh structure obtained in the simulation at two different times during the equilibration at $P = 42$ GPa. Darker regions in upper panel indicate defective sh. Several periodically repeated simulation cells are shown.

4.2 Carbon

We propose two different applications of our method to the study of Carbon under high pressure conditions: the behavior of C_{60} crystal (fullerite) under extreme conditions of pressure and temperature, in particular its transition to diamond–like structures, and the interesting structure transformation from graphite to diamond. Due to the enormous technological interest in the properties and in the synthesis procedures of diamond or very hard amorphous carbon, it is of interest to investigate via first–principle simulations the conversion of carbon from its low–pressure sp^2–bonded phases, like C_{60} or graphite, to the sp^3–bonded diamond–like phases.

We discuss the physical properties and our results on C_{60} and graphite separately in the next sections of this chapter, while here we briefly describe only those details of simulation which are shared by both applications. In our simulations a Car–Von Barth atomic pseudopotential for carbon in the Kleinman–Bylander form was used [46]. The sampling of the BZ is restricted, as usual, to the Γ–point only. Due to the hardness of carbon pseudopotential and to the large volume reduction expected in the compression of both fullerite and graphite, the kinetic energy correction of Eq. 3.31 is essential. We use in Eq. 3.31 $A = 70$ Ry, $\sigma = 8$ Ry and $E_0 = 35$ Ry. Although full convergence can not be claimed with 35 Ry energy cut–off, with this choice bond lengths in solid carbon are overestimated by only a few per cent [46]. Additionally, the equations of motion have been "preconditioned" by introducing different masses for different plane-wave components [47, 48], allowing us to use for the integration step $\Delta t = 6$ a.u. (1.45×10^{-4} ps)

instead of $\Delta t = 2$ a.u., as required by the standard integration algorithm in presence of the kinetic energy correction of Eq. 3.31. The parameter μ (in Eq. 2.23) was fixed to 200 a.u.

4.2.1 C_{60}

In the last few years there have been a number of fascinating experimental results on the properties of fullerite, solid C_{60}, at ambient conditions and at high pressures. These include observations of high–T_c superconductivity [49] in doped fullerite, speculations about a possible super–hardness of compressed fullerite [50], and the possibility to induce with both hydrostatic and non–hydrostatic compressions structural transformations of fullerite into graphite [51], diamond [52] or unknown amorphous structures [53] at high pressures, or to new molecular structures at relatively small pressures [54, 55] and high temperatures [56, 57].

The experimental situation is far from being complete and understood. This is because the results seem to strongly depend on experimental conditions, and particularly on compression procedures and compression rates.

The single molecule in fullerite has the well known truncated–icosahedral structure with alternating pentagons (twelve) and hexagons (twenty) (see Fig. 4.13), only slightly relaxed in the solid by the weak interactions with the neighbours. The molecule is characterized by strong sp^2 bonding, with two different types of C–C bonds: one, referred as *single* bond, of length 1.46 Å, on the regular pentagons, and the other, referred as *double* bond, of length 1.40 Å [58], shared by two hexagons. Unlike the layered graphite structure, in which the sp^2 bonds lie in two dimensions, the solid C_{60} structure has sp^2 bonds that

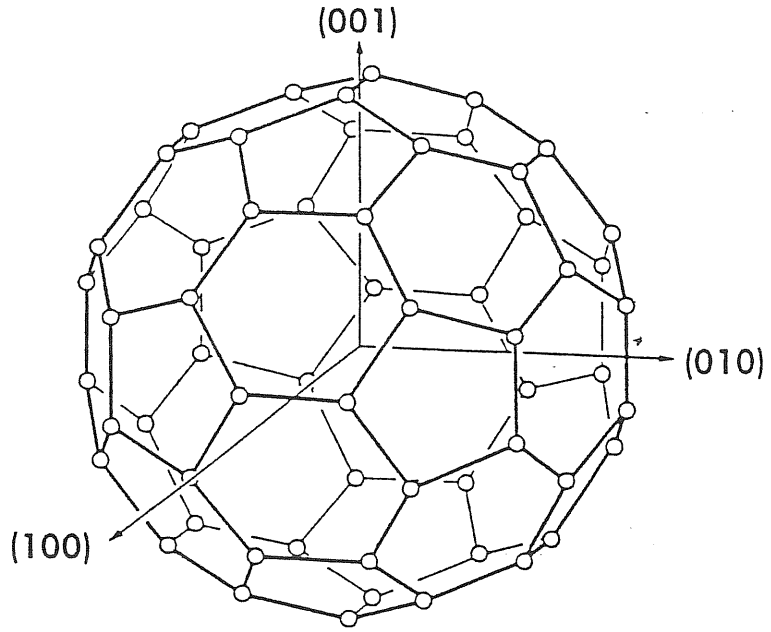

Figure 4.13: Geometry of the C_{60} molecule.There are two different type of C–C bonds: one is on the regular pentagons and the other is shared by two hexagons. Crystal axis of the fcc assumed in our calculations are also shown.

curve into three dimensions. [4] The inter–molecular interaction is a rather weak van der Waals interaction. At ambient conditions of pressure and for temperature below 249 °K, C_{60} molecules in fullerite are rotationally ordered and form a simple–cubic lattice with $Pa3$ space group, with four molecules per primitive cell [60]. Above 249 °K fullerite has the fcc structure with orientational disorder of the molecules. The lattice parameter is found to be a_0= 14.198 Å at room temperature [55]. At atmospheric pressure fullerite has low bulk

[4]The curvature introduces a rehybridization of the s and p–states of carbon, so that neither the σ nor the π orbitals are any longer "pure" as in the planar structures. In particular, the π–orbitals acquire a certain percentage (about 12%) of s character from the mixing of the $2p$ atomic states with the low–lying $2s$ ones [59].

modulus (K_0= 18.1 ± 1.8 GPa), characteristic of the isotropic van der Waals intermolecular bonding. As the intermolecular distances are reduced under increasing pressure, the bulk compressibility is expected to approach that of the C_{60} molecule (giving eventually to fullerite a super-hard property [50]).

The fcc structure of fullerite is found to be stable at ambient temperature up to hydrostatic pressures of about 20 GPa [55, 53]. For pressures below this limit, electronic bands are relatively narrow due to weak intermolecular bonding. Fullerite can be classified as a semiconductor with a direct energy gap at X–point of BZ of about 2.3 eV at zero pressure [61]. Electrical resistivity [54] and optical absorption [53] measurements show that this gap reduces by increasing pressure and should possibly close for pressures in the range of 30–40 GPa [53]. However the predicted metallic phase, together with the super–hard property of fullerite, has never been observed: an irreversible transformation occurs for pressures around 20 GPa. with C_{60} molecules collapsing into a new structure. Based on visual observations and Raman measurements, Núnez Regueiro and co–workers [52] have reported the appearance of polycrystalline diamond. This result apparently relies on the highly non–hydrostatic pressure conditions used. Under more hydrostatic conditions, Moshary *et al.* [53] have found a new phase which they suggested to be a new form of amorphous carbon (a–C) due to an anomalous high transparency, *i.e.* a large optical gap, possibly attributed to the formation of a high number of sp^3 bonds. More recently optical absorption experiments [62] on C_{60} in the same pressure range did not however find this anomalous transparency of the new phase thus suggesting that this phase is probably similar to a normal a–C.

At higher temperatures fullerite behaves quite differently, in particular in the relatively low pressure range. Iwasa *et al.* [57] find rhombohedral structure with hexagonal lattice parameters of $a_0 = 9.22$ Å and $c_0 = 24.6$ Å in samples of fullerite prepared at temperatures between 500 and 800 °C. This hexagonal structure can be interpreted as the distortion of fcc structure resulting from an elongation along the [111] direction. Núnez Regueiro *et al.* [56] find that fullerite collapses to a graphitic amorphous at 8 GPa and 1500 °K. At lower pressure (2–4 GPa) and for temperatures below 1000 °K they find the hexagonal structure, with a sort of polymerization of the molecules in the hexagonal plane. Finally, Yoo *et al.* with quasi–isoentropically shock–compression and subsequent quenching, observe a fast reconstructive transformation to graphite near 17 GPa; the graphite recovered from 27 GPa and about 600 °C is found to be relatively well ordered.

The absence of extensive theoretical studies on fullerite under pressure and the open questions posed by different contradictory experimental findings make this system a very appealing subject to be studied by means of our constant–pressure *ab–initio* MD.

Although in the real life there is orientational disorder for the molecules in the fcc structure (above 249 °K), guided by the recent experience of first principles constant–volume calculations on C_{60} [63], we choose to simulate an fcc cell containing a single C_{60} molecule. This implies that all the molecules in the infinite crystal have the same orientation, which we fix at the beginning of the simulation to be that of the tetrahedral space group T_h^3. This choice maintains the highest possible symmetry between the icosahedral symmetry of the C_{60} molecule and that of the fcc lattice. The use of a single molecule in the simulation box introduces immediately some limitations, in particular in the study of

molecular structures, since all molecules of the infinite crystal are identical and have the same behavior, inhibiting even in principle the possible formation of any molecular crystal arrangement not corresponding to a Bravais lattice. However we are mainly interested in the study of fullerite under extreme pressure conditions, where experiments reveal atomic structure derived from the collapse of C_{60}. The limitation introduced by the use of a single molecule is therefore expected not to be fundamental.

The lattice constant for the initial cell was fixed to $a_0 = 14.33$ Å, which is the equilibrium lattice constant obtained from static LDA calculations with Γ–point only, the same pseudopotential for carbon, and an energy cut–off of 80 Ry (this value for a_0 has to be compared with the experimental value at ambient pressure: 14.198 Å [55]). With our choice of parameters in Eq. 3.31 the Pulay stress [36] at a_0 is reduced from −29 GPa for a constant number of plane–waves calculation, corresponding to $E_{cut} = 35$ Ry at a_0, to −4 GPa.

In a first simulation we heated the system up to 300 °K with fixed–cell MD. We then started with the variable–cell MD, using $W = 4.9$ C–mass in Eq. 2.25. We increase the applied external pressure by steps, controlling ionic temperature with Nosè thermostat. Due to the small fullerite bulk modulus, in the first part of the compression procedure we observe large volume reduction, without any relevant distortion of C_{60} molecule. Up to a volume of 8.5 Å^3/atom ($\sim$ 70 % of the starting volume V_0) the cell almost deforms isotropically, reducing the center–to–center distance between nearest–neighbours molecules reducing from 10.13 Å to $\sim$ 9.1 Å. C_{60} molecule just "breathes" with mean radius oscillating around 3.5 Å, and the internal stress is determined almost only by this

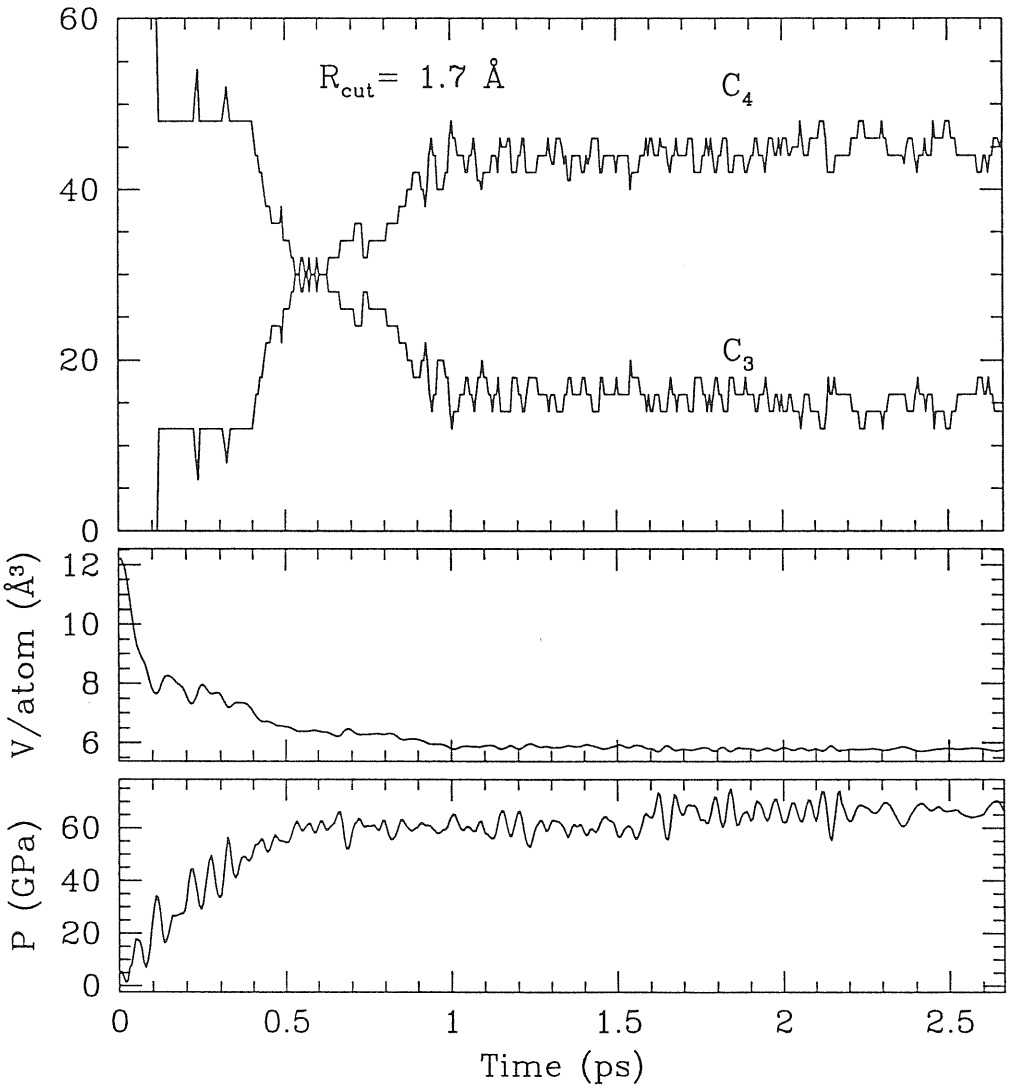

Figure 4.14: Compression of fullerite with variable–cell MD. From upper panel: number of 3–coordinated (C_3) and 4–coordinated (C_4) atoms inside a distance R_{cut} = 1.7 Å, volume per atom, and calculated internal pressure. The atomic temperature oscillates around T=300 °K, controlled by Nosè thermostat.

breathing. In Fig 4.14 the number of 3–coordinated (C_3) and 4–coordinated (C_4) atoms, the volume per atom, and the internal pressure are shown as functions of time during the simulation. Coordination is defined considering neighbour atoms to lie at distances less than the first minimum (r_m) of the particle–particle correlation function $g(r)$. In the present case this minimum is around 1.7 Å during the compression of the system, except for the first part of the simulation, when $g(r)$ has a very sharp first peak with $r_m = 1.5$ Å (see Fig. 4.15). In that case the second peak is however at $r > 2.1$ Å, due to the second nearest neighbours in C_{60}. Thus, choosing a cut–off radius $R_{cut} = 1.7$ Å for the calculation of atomic coordination in the whole simulation, only nearest neighbours are taken into account. Charge density plots show that for carbon–carbon distances up to this value the charge density overlap gives rise to chemical bonds. We can therefore consider nearest neighbour atoms as bonded.

As shown in Fig. 4.14 during the first part of the compression atoms are all 3–coordinated and no extra bonds appear. The angular distribution relative to this part shows two sharp peaks centered on the ideal C_{60} angles of 108° and 120° (see Fig. 4.15). The *plateau* at times between 0.1 and 0.4 ps reflects instead the presence of inter–molecular bonds. The last part of Fig. 4.14 show that C_4 atoms instead prevails at high pressure. For volumes immediately below 8 Å^3/atom charge density overlap between nearest–neighbour molecules becomes non longer negligible. We observe the formation of new inter–molecular bonds of the type showed in Fig 4.16, which we can label "65/56", since they link two atoms shared by a hexagon and a pentagon with two atoms shared by a pentagon and a hexagon of another molecule. The average length of the new bonds connecting the C_{60}'s is

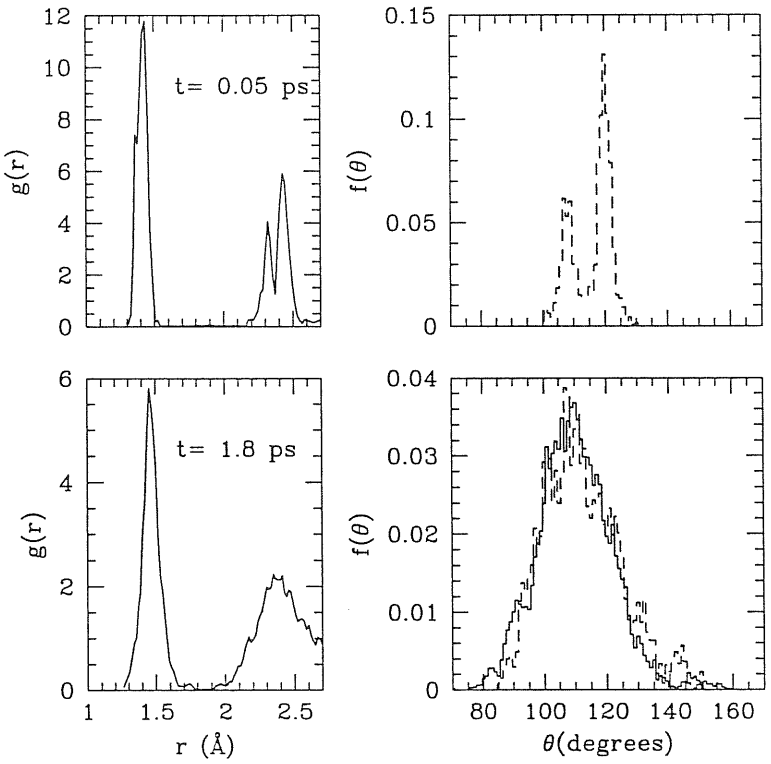

Figure 4.15: Radial distribution function $g(r)$ and angular distribution $f(\theta)$ of 4–coordinated (solid line) and 3–coordinated atoms (dotted line) at two different times during the simulation. Data are obtained averaging over 100 atomic configurations about the indicated time. $R_{cut} = 1.7$ Å has been used for the calculation of the coordination.

1.55 Å, which is indeed very close to the bond length in diamond. The formation of these bonds corresponds to a non–isotropic distortion of the cell and of C_{60}. Simulation cell presents an initial rhombohedral contraction along the $[\bar{1}11]$ direction. The distance between the centers of C_{60} and the six nearest–neighbour images on the $(\bar{1}11)$ plane increases to 9.25 Å, while the distance of the other six molecules outside this plane reduces to 8.5 Å.

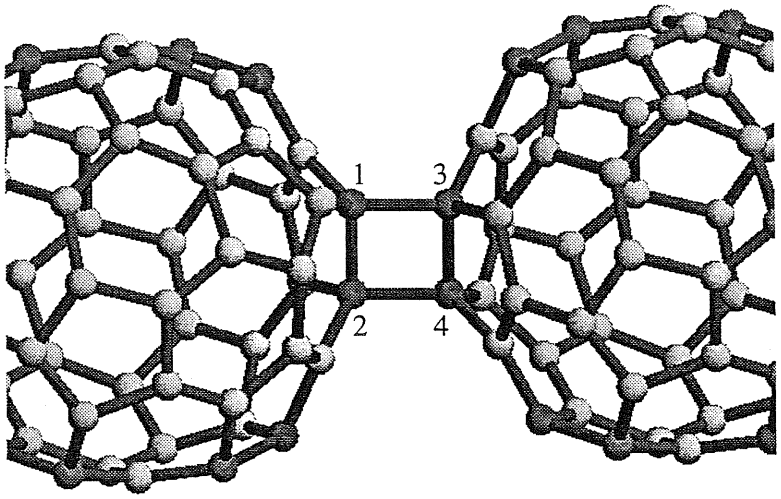

Figure 4.16: "65/56" bonds between atoms of two C_{60} molecules. The bond–length are: $d_{12} = d_{34} = 1.62$Å, $d_{13} = d_{24} = 1.55$Å.

C_{60} distorts correspondingly. This distortion is driven by the formation of 12 bonds of the type 65/56 all lying onto the $(\bar{1}11)$ plane. 65/56 bonds are not the most energetically convenient way to link C_{60} molecules. Hartree–Fock total energy calculations [64] on different C_{60} dimers show that the greatest energy gain is given by 66/66 bonds. The geometry of the initial orientation of C_{60} in our simulation favours 66/66 bonds. However a slight rotation of C_{60} during the first stages of the compression path makes a "56" bond facing a "65" bond. When this happens, cell fluctuations deform and bring C_{60} close enough to the

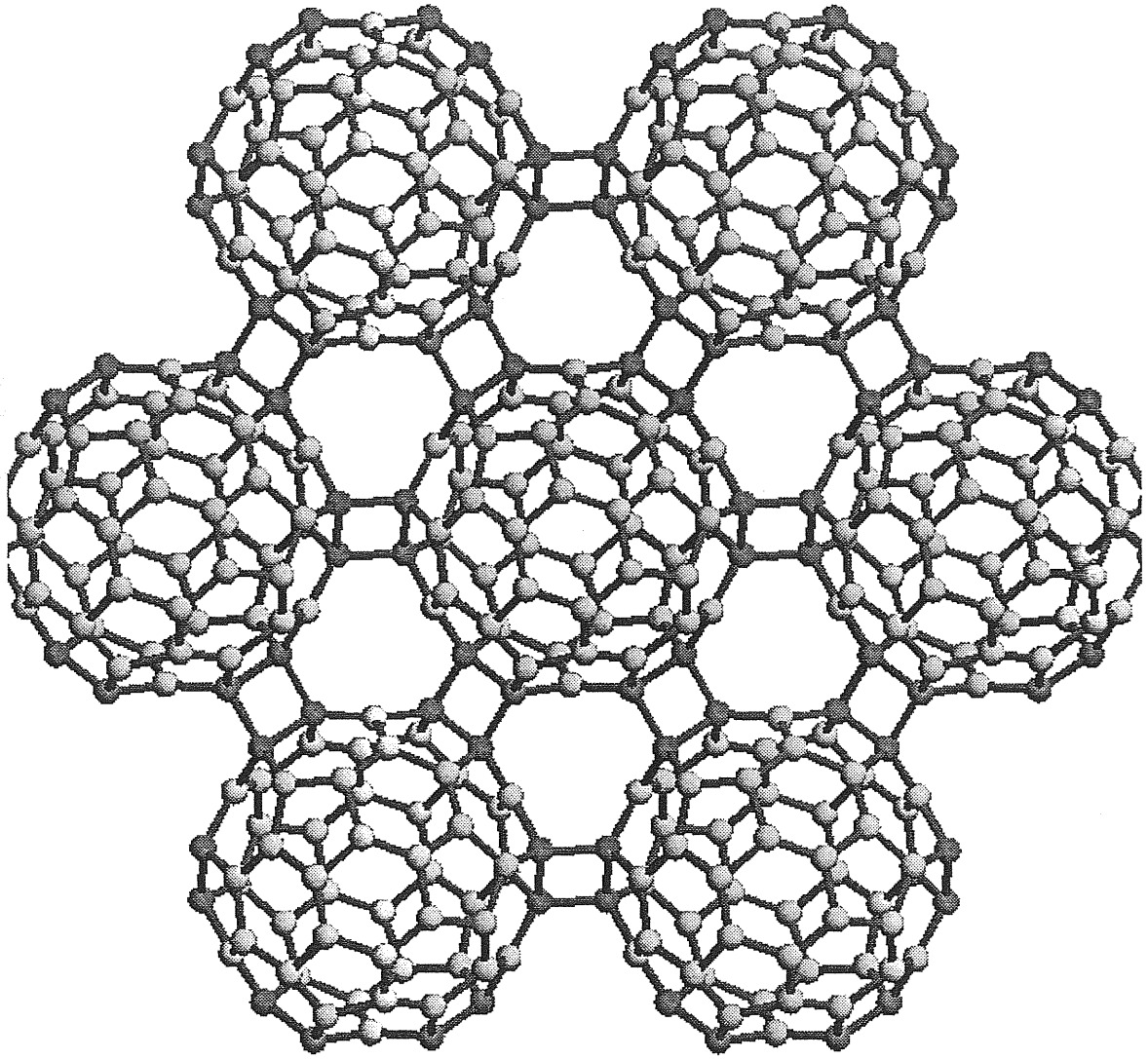

Figure 4.17: Hexagonal structure of fullerite. A hexagon into $(\bar{1}11)$ plane is shown. The stacking of the planes is $ABCABC$.

nearest neighbours in $(\bar{1}11)$ plane to form intermolecular bonds. In Fig. 4.17 we show a shell of nearest–neighbour molecules on this plane. The resulting hexagonal structure has a $ABCABC$ stacking of hexagonal planes. This stacking may however be an artefact of our initial choice of periodic boundary conditions. By further increase external pressure, this hexagonal structure appear to be stable until the volume of the system reduces to $\sim$7 Å^3/atom: no other bonds form and the rhombohedral distortion of the original fcc lattice is stabilized to an elongation along the $[\bar{1}11]$ direction, with a ratio $c/a = 2.56$ ($c/a = 2.18$ being that of ideal fcc). This crystalline structure is similar to that produced experimentally by Iwasa *et al.* [57], although molecule structure and inter–molecular bonds in the hexagonal phase are not experimentally known. By synthesizing samples at high temperature (between 500 and 800 °C) and quasi–hydrostatic pressure of 5 GPa, and then quenching temperature and relaxing pressure to ambient conditions, they have found an hexagonal structure with $c/a = 2.65$. However by relaxing the hexagonal structure, stable at the volume of 8.0 Å^3/atom and pressure of 15 GPa, down to zero applied pressure, we found that our system is unstable at ambient conditions and revert to pristine C_{60}. Metastability of hexagonal C_{60} at ambient pressure is also studied in a different set of experiments [57], showing that fullerite may be reobtained by simply heating the samples at $\sim$ 300°C.

As visible in Fig. 4.14, for pressures between 50 and 60 GPa and volumes less than 7 Å^3/atom, the number of 4–coordinated atoms increases: new inter–molecular bonds form. The simulation cell furthermore lowers its symmetry becoming triclinic. C_{60} becomes very distorted: some bonds between atoms of the same molecule involved in cross–

links of the type shown in Fig. 4.16 break and few atoms "collapse" inside the original C_{60} cage (see Fig 4.18a). These collapsed atoms are still 3–coordinated, but their angular distribution reveals a broad peak centered on 109°, suggesting incomplete sp^3 hybridization with a dangling bond pointing inside the molecule. This bond may eventually be saturated forming new intra–molecular bonds. The collapse of C_{60} ends up in an amorphous structure with a high amount of 4–coordinated atoms (more than 40 atoms of the original molecule, see Fig. 4.18b), which form a network that percolate through the space, and an angular distribution of bonds centered on 109° (see Fig. 4.15). The final volume is of 5.8 $Å^3$/atom for a calculated pressure of 70 GPa. The atomic structure we observe is quite different from that of normal a–C (suggested by Snoke *et al.* [62] also for the high pressure phase), and is in agreement with Ref. [53] where a high degree of sp^3 hybridization is suggested. The predominance of sp^3 bonds distinguishes indeed the obtained structure from ambient pressure a–C observed experimentally [65], or simulated with standard fixed–volume Car–Parrinello MD via melt–quenching [66]. Normal a–C is in fact found to be mostly "graphite–like" [65, 66], with a fraction of sp^2 sites ranging from 50 % and 90 % and sp^3 sites forming separated clusters.

Studying the symmetry of the cell, no evidences of intermediate phases between the hexagonal structure and the amorphous are found.

The structural transformation is also revealed by the change in the electronic structure. In Fig. 4.19 we report the eigenvalues of the two highest occupied and of the two lowest unoccupied Kohn–Sham electronic states, together with the energy gap between them as functions of time during the simulation. We recall that the Kohn–Sham eigenvalues

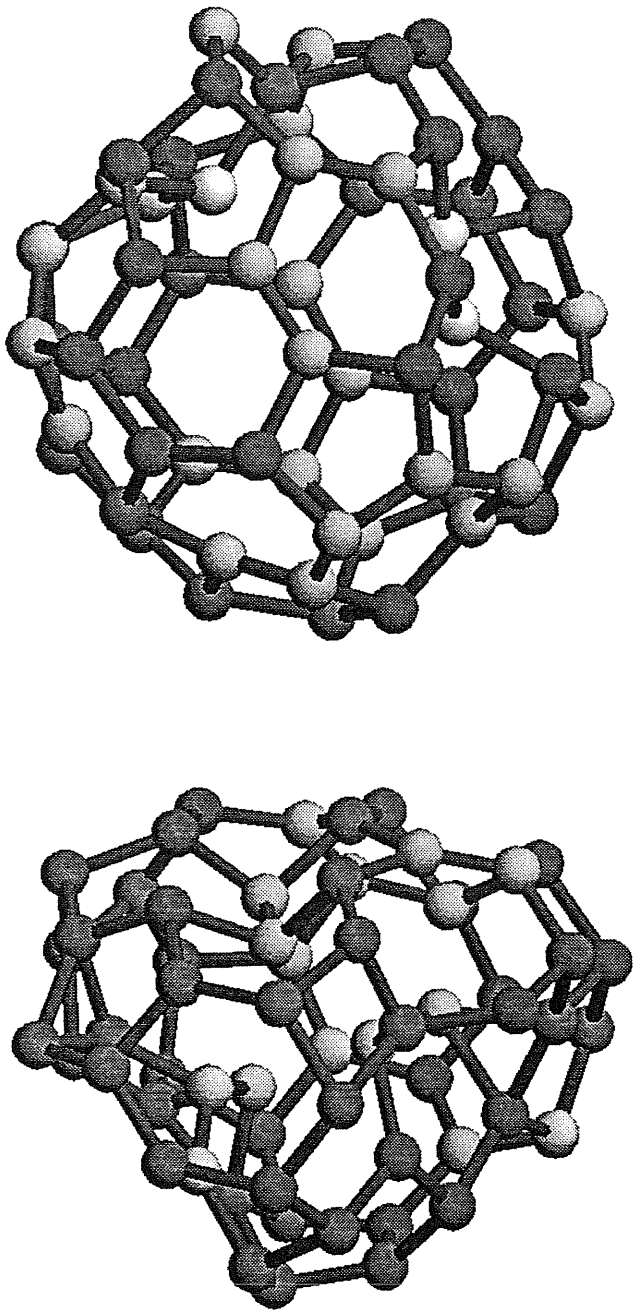

Figure 4.18: C_{60} molecule during the compression. Upper panel: snapshot at $t = 0.65$ ps. Collapsed part of C_{60} are clearly visible. Lower panel: final configuration at $t = 2.66$ ps. C_{60} collapses in an amorphous structure. Dark atoms are 4–coordinated (bonds outside the original molecule are not shown).

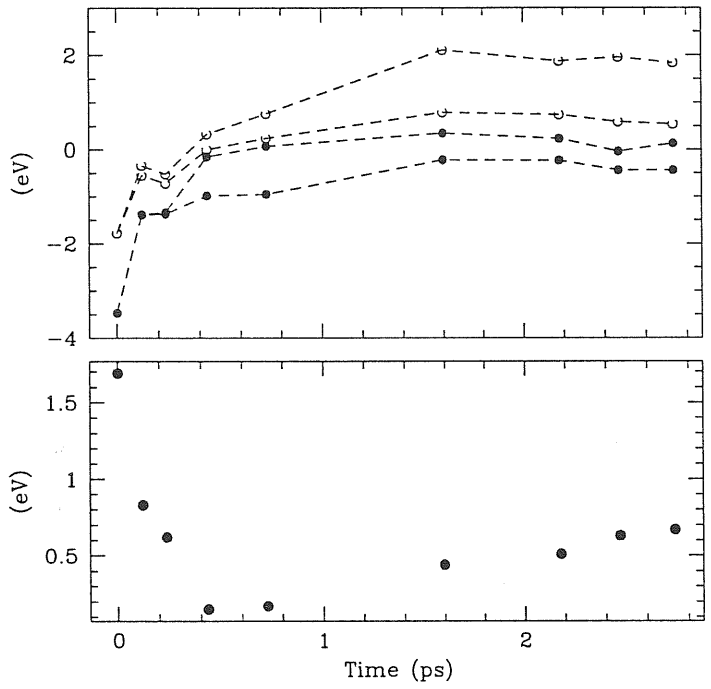

Figure 4.19: Upper panel: eigenvalues of the two highest occupied (solid spots) and of the two lowest unoccupied electronic states of C_{60}, as obtained using Γ–point sampling of the BZ in the MD simulation. Lower panel: corresponding HOMO–LUMO energy gap.

are not the quasi–particles energies, which in many body theory describe the electronic excitations. The similarity is largely an assumption and a result of experience on many systems, and in general comparison with LDA band structures and experiments must be made with caution [59]. Consistent with the known general trend [67], the LDA energy gap significantly underestimates by almost 1 eV the experimental one in fullerite [68, 69]. Therefore comparison with our results and experimental data is only qualitative. By increasing pressure the initial band gap (at Γ–point) of 1.7 eV reduces to 0.15 eV just

before the transition to amorphous takes place. This is in agreement with experimental findings, that also show a gap reduction under pressure [54, 62]. Correspondingly to the formation of sp^3 bonds, at the C_{60} — a–C transition the gap increases and is 0.7 eV in the final structure.

We also performed a second high temperature MD simulation starting from the same fcc fullerite. In this simulation our interest was mainly to obtain more informations about the hexagonal phase observed in the simulation at room temperature (unlike in experiments [56, 57], where the phase is observed after heating the system at high temperature), and in reproducing the transition to amorphous structure at a different temperature. Therefore we initially heated C_{60} at 600 °K. We then started increasing the applied pressure with a rate roughly one half of that used in the first simulation, raising simultaneously the temperature from 600 to 900 °K in a overall time of 0.3 ps. After that time the mean temperature was kept fixed by using a Nosè thermostat.

For pressures below 60 GPa, the behaviour of atomic coordination, compared to volume reduction and calculated pressure, is similar to that shown in Fig 4.14 for the room–temperature simulation. In particular a *plateau* of 12 4–coordinated atoms appear for volumes ranging between 8 and 7 $Å^3$/atom. In the present case however bonds configuration do not lead to an hexagonal structure. The deformation of the simulation cell remains roughly isotropic up to 60 GPa. No nearest–neighbour plane is chosen by the system to form the inter–molecular bonds, which instead fluctuate between all the nearest–neighbour molecules. A quenching of temperature down to 300 °K in $\sim$ 0.6 ps does not change this picture. More calculations are needed to clarify this point.

The collapse of C_{60} cage occurs again for volumes around 6.5 Å^3/atom and leads to amorphous structure with 75 % of sp^3 sites. By further increasing the pressure up to 120 GPa the fraction of sp^3 sites increase to 85 %. The final structure at that pressure has a volume of 5.1 Å^3/atom (to be compared to 4.7 Å^3/atom for diamond at the same pressure), and an energy band gap of 1 eV, greater than that of the first sample, according to the higher fraction of sp^3.

We have then relaxed the pressure to zero in 1 ps. The final structure is still an amorphous. We observe a monotonic decrease of sp^3 sites fraction, which stabilizes around 60 % at ambient pressure. These sites still percolate through the space forming a network. The corresponding angular distribution is still centered to 109°, but more broaden than at high pressure. Due to the strong sp^3 network which gives a high bulk modulus. the volume difference during the decompression is small, 6.4 Å^3/atom being the final volume at zero pressure (to be compared with 5.69 Å^3/atom of diamond and 12 Å^3/atom of fcc fullerite). The final structure at zero pressure has a Γ–point energy gap of 2.1 eV. More work is in progress to study this higly 4–coordinated a–C obtained upon compression at high pressure.

4.2.2 Graphite

The conversion of pure graphite into diamond is known to occur at extreme pressure and temperature conditions [70]. Despite a large amount of investigations of this important process, there are many open questions. First of all the main transformation path is uncertain [71]. Secondly, the mechanism leading alternatively to cubic and hexagonal diamond is unclear [72, 73]. Also, the presence of an intermediate phase between graphite and diamond has often been invoked [74, 75]. Ab-initio calculations aiming at resolving these questions were mainly based on the comparison of the structural properties of these known phases, or on the study of high-symmetry transformation paths [76, 77, 78, 79]. We have therefore applied our *ab-initio* MD scheme to study this transformation without artificial symmetry constraints.

Our starting simulation cell is a triclinic cell containing 48 atoms arranged in the graphite structure. According to the discussion given in section 4.1, the intial cell has been chosen as the one which minimizes the total energy at the experimental values of the graphite unit cell parameters (a_0 = 2.461 Å, c_0 = 6.709 Å) and sampling only the Γ–point of the super–cell BZ. The total energy of the selected cell is 8 mRy/atom lower than the value obtained at convergence in K–point sampling. The starting c/a obtained by relaxing both ions and cell degrees of freedom at zero external pressure is smaller than the experimental value by about 12 %. The difference in energy between our relaxed graphite super–cell and cubic diamond evaluated with ten special points in the irreducible BZ [80] is as small as 1 mRy/atom, but favours diamond, instead of graphite, as known

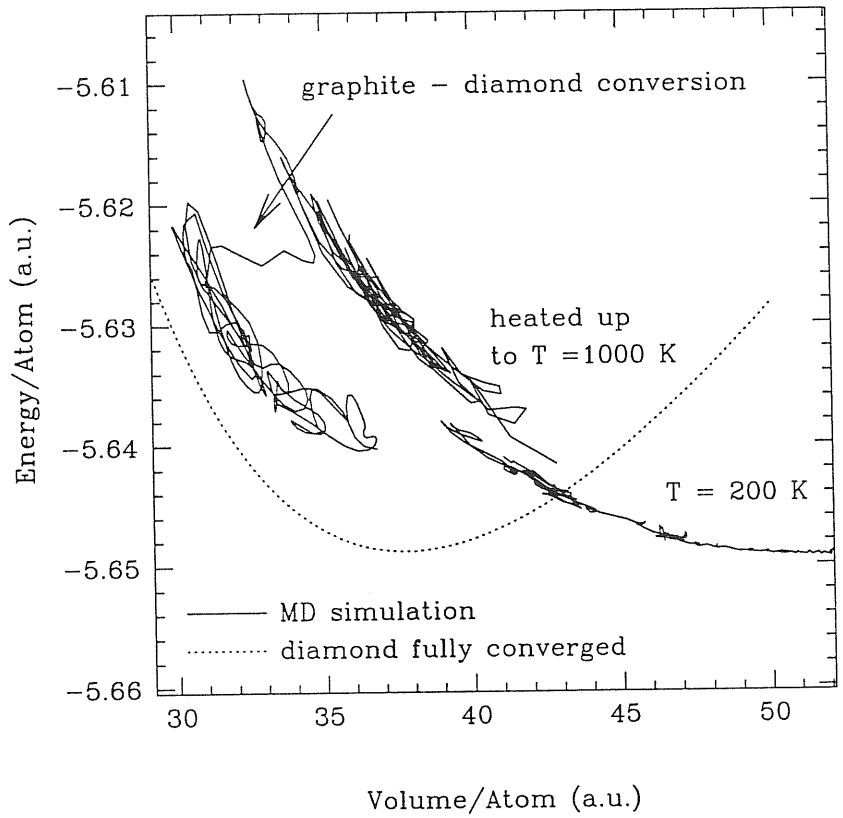

Figure 4.20: Graphite → cubic diamond transformation in the energy vs. volume diagram, as obtained by the MD simulation with the 48 atoms cell. Energy and volume per atom are reported.

experimentally and checked theoretically through carefully converged calculations [76]. Considering the large activation barrier for the graphite → diamond conversion, this error is however completely negligible. Figure 4.20 sketches the history of the simulation on the energy versus volume diagram. Graphite was first compressed at T= 200 °K up to a pressure of 60 GPa. At the first stages of the compression, the $ABAB$ stacking

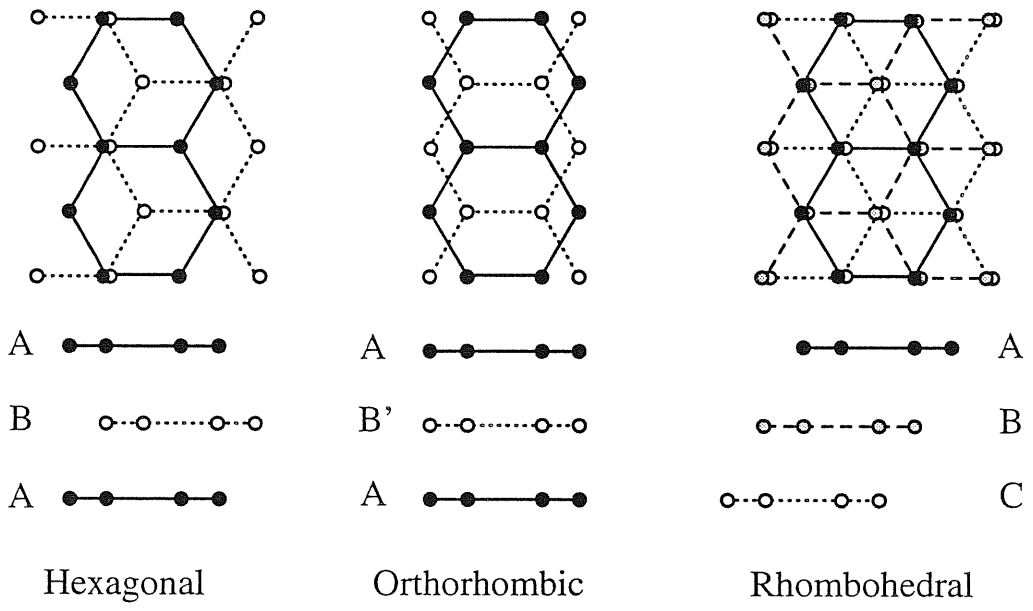

Figure 4.21: Hexagonal, orthorhombic and rhombohedral phases of graphite. The different stackings of hexagonal planes are viewed along the c–axis (above) and sideways (below).

of hexagonal graphite slowly changes to the $AB'AB'$ stacking of orthorhombic graphite (OG), shown in Fig. 4.21. Although OG is not found in nature, its relevance has been often pointed out in the literature since most high–pressure phases of carbon are connected by high–symmetry paths to OG [79, 75, 82]. Since we expect the cohesive energies of graphite in its different stackings to be very close one each other, we checked whether the transition hexagonal graphite $\rightarrow$ OG of our simulated crystal could be an artifact of the Γ–point sampling. We therefore performed a set of converged total–energy calculations of ideal graphite in its stackings, at different volumes, and we found that they are degenerate within

the computational error ($\sim$ 1 mRy/atom). In the absence of conclusive answer from static calculations, we attribute the relative stability of OG with respect to hexagonal graphite of our MD simulation to the Γ–point sampling, but we do not rule out the possibility that OG may indeed be the most stable stacking of graphite at high pressure, as suggested in Ref. [75].

Since both hexagonal and cubic diamond have been experimentally quenched to ambient conditions only after heating up to 1000–2000 °K during the compression, we have heated our crystal up to 1000 °K. Upon further compression, the graphite phase eventually converted into diamond. We then slowly released the pressure in order to follow a portion of the Murnaghan equation of state and to compare it with the equation of state of perfect cubic diamond computed with ten special points in the BZ (dotted line in Fig. 4.20). The $\sim$ 5 mRy/atom energy difference in the two equations of state has to be traced both to the Γ–point sampling of our supercell and to thermal motion. The simulated graphite $\rightarrow$ diamond conversion occurs, as usual, at a high value of the applied pressure ($\sim$ 100 GPa, to be compared with the experimental value of 15 GPa [70]). Unlike the previous example of Si, in this case the transition carries through without the formation of defects, and we get perfect cubic diamond. The transition is consistent with a solid-solid martensitic transformation. For increasing pressure, the interplanar distance in graphite first collapses, leading to a buckling of the graphitic basal planes. Next, the buckled planes suddenly give up their π electrons and bond to one another, becoming the (111) planes of the diamond phase, with the [001] direction of the original graphite phase becoming the [121] of diamond, as shown in Fig. 4.22. The geometric path followed by our

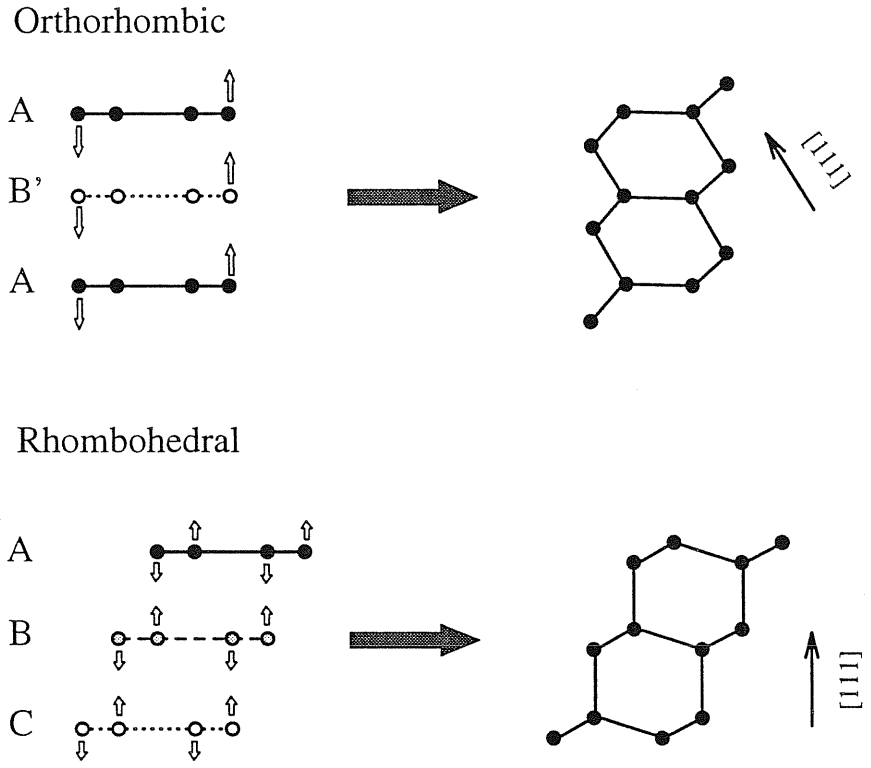

Figure 4.22: Geometric paths for graphite → diamond transformation. Depending on the stacking of graphite, the graphite [001] direction coincides with the diamond [111] in the case of rhombohedral graphite or with diamond [121] in the case of orthorhombic graphite. Atomic displacements from the graphite basal planes are shown on the left by the arrows.

system does not coincide with that proposed by Fahy *et al.* [78]. They have studied the transformation in two steps: 1) from hexagonal graphite (stacking $ABAB$ of the hexagonal planes) to rhombohedral graphite (stacking ABC, see Fig. 4.21) by slipping every third plane, 2) from rhombohedral graphite to cubic diamond by collapsing the interpla-

nar distance and subsequent buckling of the graphitic planes in such a way that the [001] direction of the graphite becomes the [111] of diamond, as shown in Fig. 4.22. Instead, the mutual orientation of our initial and final phases is consistent with that of shock waves experiments [81]. No evidence for a thermodynamically stable or metastable intermediate phase with buckled hexagonal planes is found at intermediate pressures.

The formation of hexagonal diamond was not observed in this first simulation. However, there are three geometrically equivalent directions, through which the graphite → hexagonal diamond may occur, while the periodic boundary conditions imposed by our 48 atom simulation cell allow for only one of them. Therefore we decided to repeat the simulation with a different box, which let all the three buckling paths open. This was done with a 32 atoms cell simply obtained with $2 \times 2 \times 2$ graphite unit cells. Preliminary results show that at room temperature and pressure of about 60 GPa the transition to hexagonal diamond takes place, and the mutual orientation of the two phases is in agreement with that proposed by the experimentalists [73, 74].

4.3 Acetylene

We present here the preliminary results of the simulation of acetylene under pressure. We are interested in the polymerization process in solid phase of the molecules of acetylene C_2H_2. The behavior of unsaturated organic compounds (like acetylene) under pressure is important for the study of the chemical bond. Molecules which interact only through week Van der Waals forces can get very close when an hydrostatic pressure is applied, and thus chemical reactions can take place when the intermolecular distance becomes smaller than a certain threshold value. These chemical reactions usually lead to the formation of linear polymers or networks. In the past many pressure induced chemical reactions were studied for a wide variety of organic molecules with double bonds C=C (alkenes) and triple bonds C≡C (alkynes), but in general the polymerization reactions were studied starting from the monomers in liquid phase [83, 84]. Only recently polymerization processes starting from molecular crystals have been studied, mainly in polydiacetylenes [85]. Solid phase polymerization is particularly interesting because it may allow the synthesis of polymer chains longer than those produced in the liquid phase.

C_2H_2 is liquid at room temperature and normal pressure. It crystalizes in the Pa3 structure at 0.7 GPa, and then in the Cmca structure at 0.9 GPa [86]. Recently Aoki *et al.* [86] have provided Raman and optical evidences of a polymerization reaction at 3.5 GPa converting the insulating molecular Cmca crystal into semiconducting polyacetylene. Polyacetylene is the prototype of semiconducting polymers widely studied in the last 20 years. The polymerization reaction takes few tens of hours to complete, indicat-

ing a delicate, possibly catalyzed, nucleation mechanism. Furthermore by increasing the pressure, and thus by reducing the distance between polymeric chains, the formation of crosslinks and the replacement of sp^2 with sp^3 hybrids are expected. This should increase the electronic energy gap with the subsequent change in the optical properties of polyacetylene. In fact colored polyacetylene crystals have been observed to become transparent for pressures above 5 GPa [86].

In our simulations we used a Von Barth–Car [46] pseudopotential for Carbon and naked coulomb potential for Hydrogen, an energy cut–off E_{cut} = 40 Ry, and the gradient corrections for exchange and correlation functional (Becke [87] corrections for exchange and Perdew [88] corrections for correlation). Before starting with the MD, we performed static total energy calculations on the structures Pa3 (cubic) and Cmca (orthorhombic). The Cmca structure lattice constant is greater than the experimental one by $\sim$ 7 %. By adding the attractive Van der Waals forces between third neighbouring molecules. as described by LeSar [89], the lattice constant changes only by $\sim$ 1 %. Due to this small improvement, Van der Waals corrections are not included in our MD simulation. Angles between molecules and bond–lengths are well reproduced (errors less than 2 % at the experimental equilibrium volume). Cmca phase has lower energy than Pa3, in agreement with experimental findings at low temperatures. We started a MD simulation with 16 C_2H_2 molecules in the Cmca structure disposed in an orthorhombic supercell with edges a, 2b, 2c with a, b, c lattice parameters of Cmca unit cell (see Fig 4.23). We initially increased pressure up to 8 GPa at 400 °K, observing only a gradual rotation of the C_2H_2 molecules. By a further pressure shock of 17 GPa, acetylene molecules react, forming

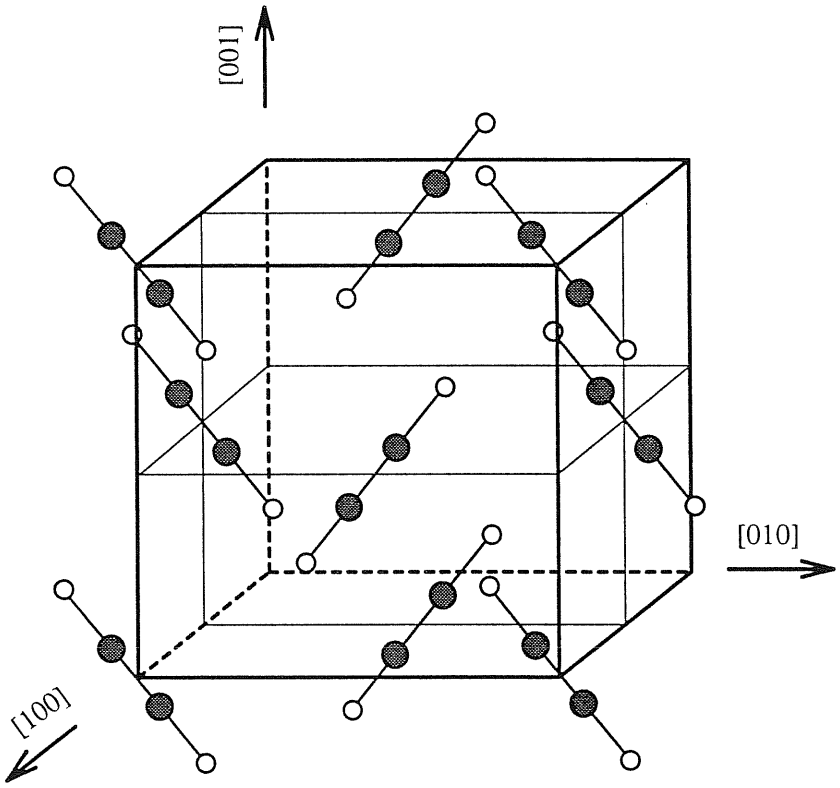

Figure 4.23: Initial Cmca structure for acetylene.

polyacetylene chains in a mixture of *trans* and *cis* forms. In Figs. 4.24–4.26 are reported the snapshots of a single a–b plane of our supercell (we have 4 planes) at three selected times during the polymerization process. In Fig 4.24 at 8 GPa, before the pressure shock, the molecules are in the Cmca structure at 400 °K. In Fig. 4.25 the pressure shock has deformed the molecules in the *cis* and *trans* configurations. In these configurations the molecules react forming the larger complex shown, and finally producing the polyacetylene chains in Fig 4.26. On the other planes a similar reaction occur. Due to the decrease of tilting angle of molecule in the Cmca structure at high pressure the molecules are nearly

parallel and thus two nearly equivalent planes for the polymerization exist: the a–b and the c–b. Incipient polymerization in the c–b plane produces the plane interlinks shown in Fig. 4.27.

By further increasing the pressure a gradual conversion of sp^2 into sp^3 bonds takes place ending up at 65 GPa with what appears to be hydrogenated amorphous carbon, where 85 % of carbon atoms are fourfold coordinated in the sp^3 configuration. The $sp \rightarrow sp^2$, and the $sp^2 \rightarrow sp^3$ conversions are irreversible and do not reverse by returning to zero pressure. These results confirm the long standing idea that unsaturated C-C bonds can not survive at high pressure [90].

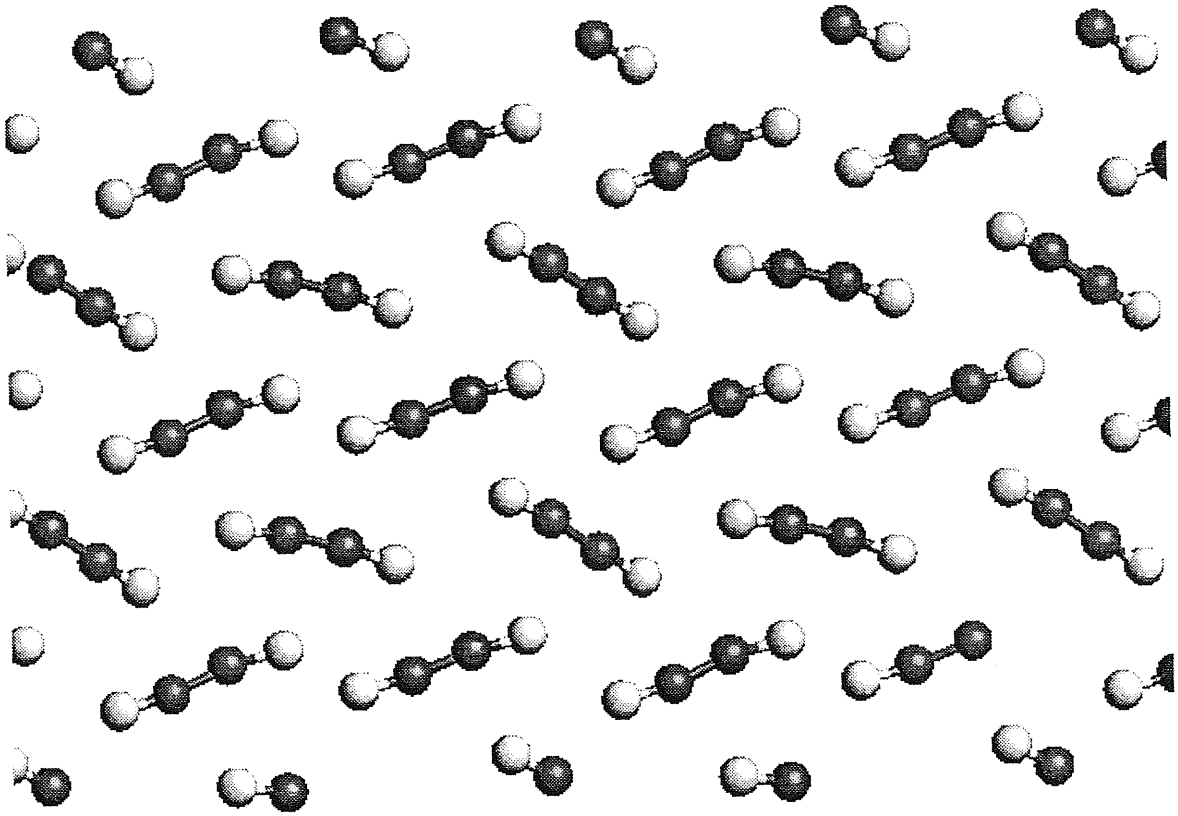

Figure 4.24: Acetylene molecules on a single a–b plane of the supercell. Molecules are in the Cmca structure. P = 8 GPa, T = 400 °K.

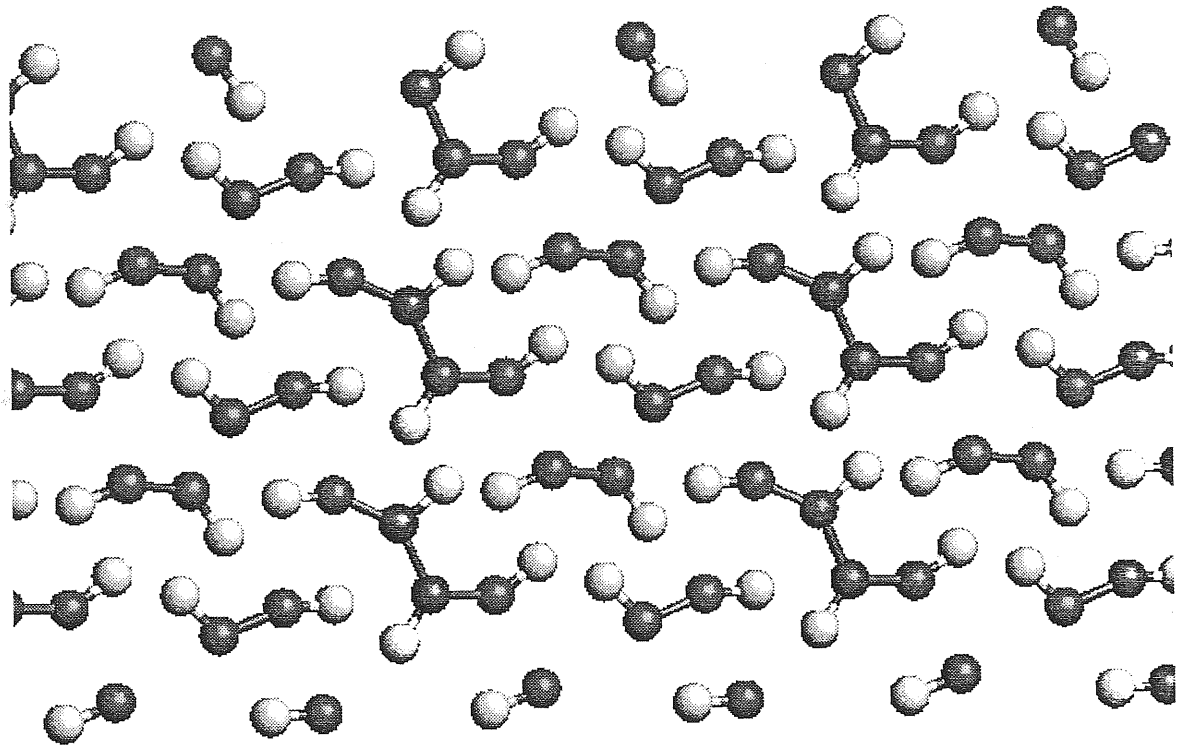

Figure 4.25: *Cis* and *trans* configuration of deformed acetylene molecules on the same plane of previous figure after the pressure shock (see text).

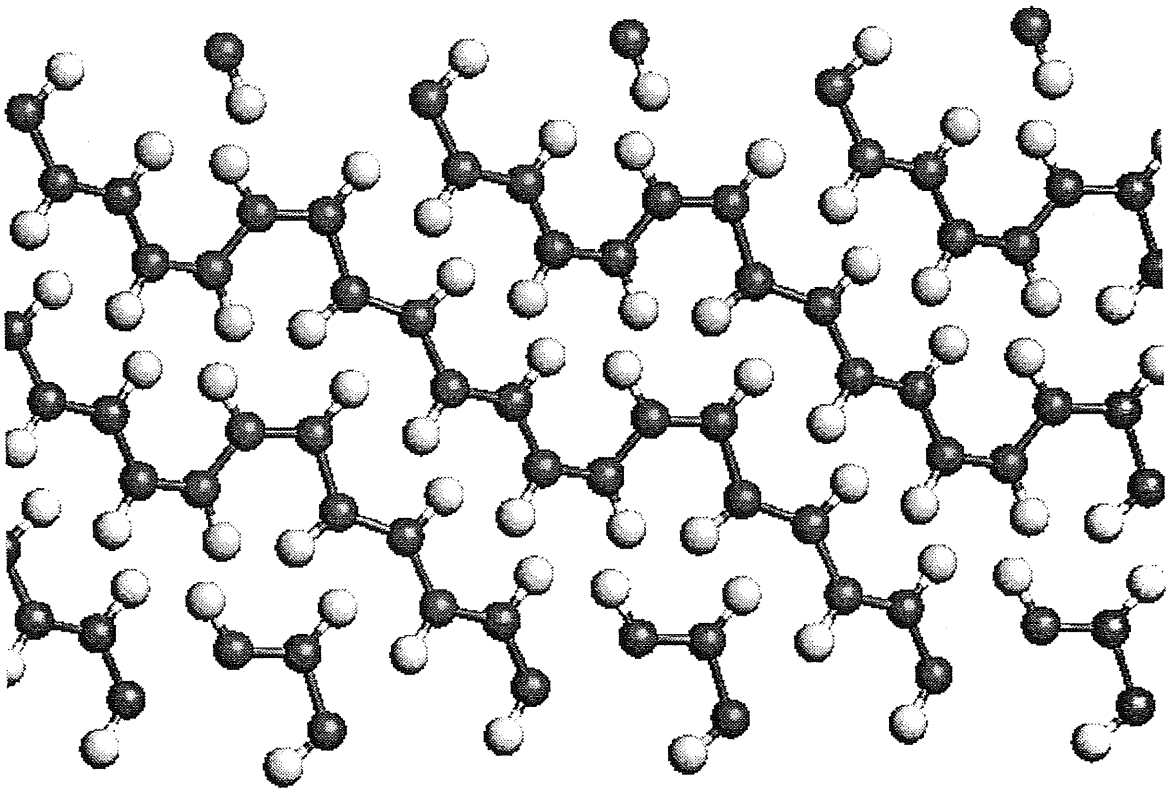

Figure 4.26: Polyacetylene chains on the a–b plane of the super–cell.

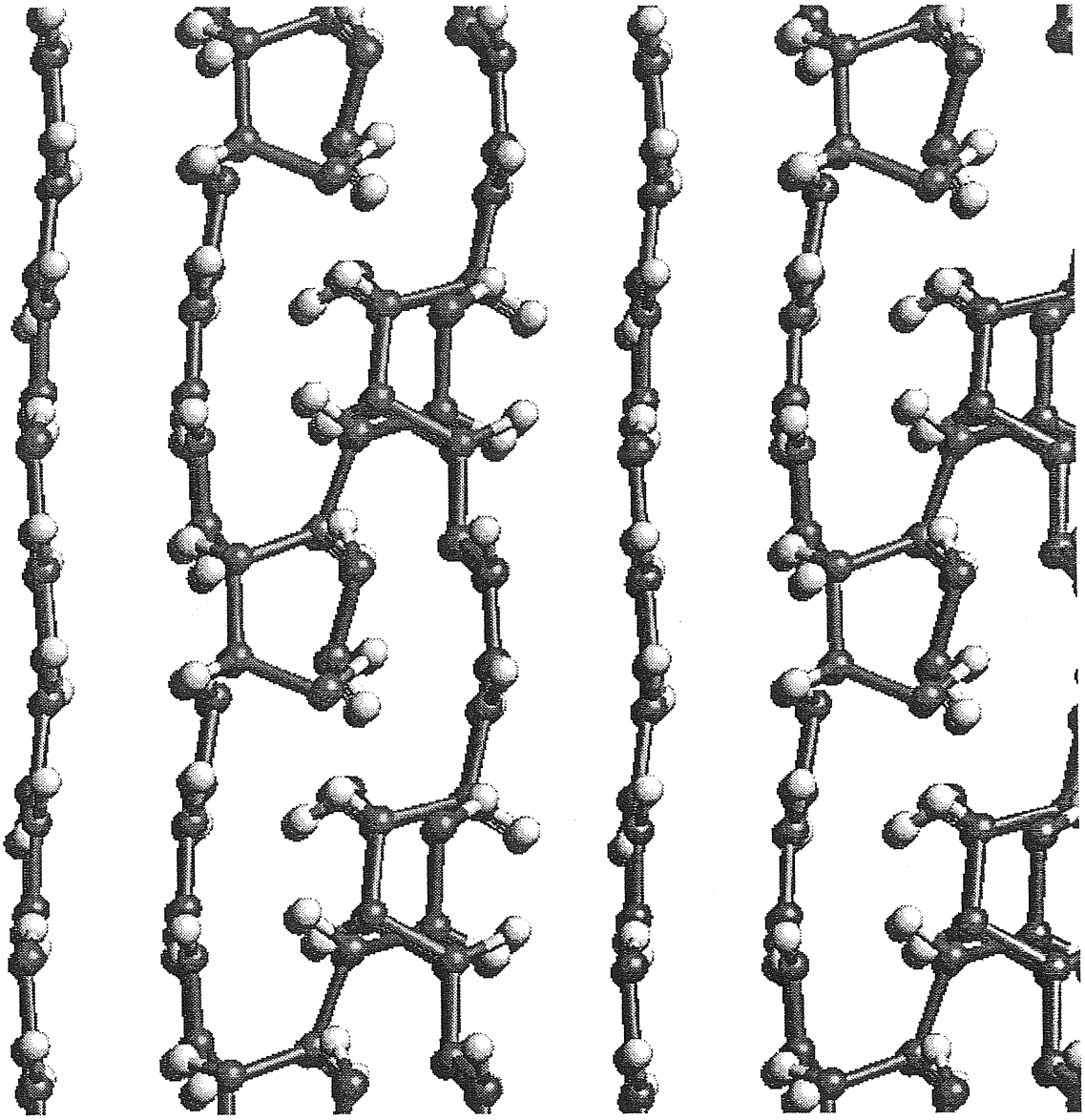

Figure 4.27: Cross–links between a–b planes, due to incipient polymerisation in the a–c plane.

5 Conclusions

In this thesis we have presented a new scheme for first–principle constant pressure MD simulation. This was obtained by efficiently combining Car–Parrinello method with Parrinello–Rahman scheme for variable cell shape dynamics. With this extension first–principle dynamical simulation of solid–solid phase transitions is now possible.

The presented applications show the power of the method: in all cases the simulated system *spontaneously* transform into the right phase, involving strong electronic structure rearrangement as hybridization change or metal–insulator transition. These kind of transformations require a good (self–consistent) description of electronic properties. For this reason our method seems at the moment to be the only reliable computational tool for the prediction of new unknown phases without any initial guess on the final stable structure.

Along the thesis we pointed out possible drawbacks of the method and suggested possible solutions. The bias due to constant plane wave number assumption (implicit in our formalism) has been corrected by introducing a modified kinetic energy functional. The price paid in this case is a shortening of the MD integration step, that can however be compensated by preconditioning electronic masses. The main limitation at the moment

seems to be related to the poor K–point representation, which up to now could be improved only by increasing the system size. In many cases few hundreds atoms are probably sufficient to achieve K–point convergence with the super–cell Γ–point sampling used in the present work. It is plausible that in the near future the simulation of systems of similar size will become practicable using parallel codes.

Although in principle the path followed by the simulated system during the structural transformation is not significant, the presented applications suggest that with our method is anyway possible to get informations about the "true" physical path. In C_{60}, graphite and acetylene the mechanism leading the simulated transformation is meaningful. We believe that in general the path obtained with the simulation may be realistic when the transformation is guided by a rearrangement of the local chemistry as in the case of hybridization change. Moreover, our method seems to be very promising for the study of chemistry under pressure.

Studying silicon, we reproduce the well–known and expected transition from diamond to sh, and, upon decompression and heating, we find the reverse transition sh $\rightarrow$ a–Si, also observed in very recent experiments. The simulation of $C_{60} \rightarrow$ a–C shows that a–C obtained in this way differs from that obtained via melt–quenching, showing in particular a high density of sp^3 sites. These are not clustered as in ordinary a–C, but percolate in the whole space. Moreover the observed intermediate molecular phase, in which C_{60} molecules are connected by short covalent bonds, helps in understanding the mechanism of formation of sp^3 sites before molecules collapse. We show that upon fast compression acetylene polymerizes at relatively low pressures, and finally converts to hydrogenated amorphous

carbon. The observed $sp \rightarrow sp^2$ and $sp^2 \rightarrow sp^3$ conversions under pressure confirm the long standing idea that unsaturated C–C bonds can not survive at high pressure. Finally, in studying the graphite → diamond transformation we find a path which does not coincide with that proposed by previous theoretical calculations, but which is in agreement with the final orientation observed in crystals undergoing shock waves.

The implementation of ultra–soft pseudopotentials in our method opens the possibility to study systems containing oxygen. The simulation of high pressure phases of solid oxygen (not reported in this thesis) is now in progress. Many interesting problems involving structural transformations of oxides and of other very hard materials in pressure and temperature ranges outside the present experimental capabilities are now practicable with our method, possibly allowing for a deeper understanding of the physical phenomena related to the very fascinating field of high pressure physics.

Aknowledgments

First of all I would like to thank my supervisors Prof. Michele Parrinello and Dr. Guido Chiarotti for their guidance and encouragement during this work, and Prof. Erio Tosatti for stimulating discussions.

I am very grateful to Dr. Marco Bernasconi and Dr. Sandro Scandolo, who have followed particularly the work on graphite and acetylene, for their precious and continous help.

A special thank to Dr. Wanda Andreoni for teaching and help and for her hospitality during my stay at IBM–Research Laboratory in Zurich, where the work on C_{60} has been done.

It is a pleasure for me to collaborate with all these people.

6 Appendix

6.1 Explicit derivation of stress tensor in LDA–DFT

We will here describe the specific form of DFT–LDA total energy functional used in our version of the CP *FORTRAN* code. We will also present the explicit formulas for the various contribution of this functional to the stress tensor. For the symbols used in this Appendix and not explicitly introduced, we refer to Chapter 3.

Let us start from Eq. 3.1. To efficiently treat the slowly decaying Coulomb forces present in the second, third and last term of this equation, it is convenient to regard the ionic core charges as smeared Gaussian distributions of width R_c, centered at the ionic sites, instead of treating them as point charges:

$$\rho_{ion} = -\sum_I \frac{Z_v}{\pi^{3/2} R_c^3} \exp\left[-\frac{|\mathbf{r} - \mathbf{R}_I|^2}{R_c^2}\right], \tag{6.1}$$

where Z_v is the number of valence electrons of the ion. With this choice we can rewrite Eq 3.1 as [19, 91]:

$$E = E_{ke} + E_{xc} + E_{loc}^{ps} + E_{nl}^{ps} + E_H + E_{sr} - E_{self}, \tag{6.2}$$

where all terms, except E_{xc}, are written in Fourier space. E_{ke} is the electronic kinetic energy, E_{xc} the exchange–correlation energy. The electron–ion interaction energy is written as the sum of two parts, the *local* (E^{ps}_{loc}) and the *non–local* (E^{ps}_{nl}) contribution. E_H is the electrostatic energy of the *total* charge distribution $\rho_t = \rho_e + \rho_{ion}$; E_{self} is the constant self–interaction of the ionic charges, and E_{sr} a corrective term depending only on the ionic positions, which cancels the error introduced in considering Gaussian ionic charges instead of point charges [19, 91].

The LDA form is used for E_{xc}, *i.e.* the exchange–correlation energy density is locally approximated by the one of the homogeneous electron gas at the same density $\rho_e(\mathbf{r})$, such as:

$$E_{xc}[\rho_e] = \int \mathrm{d}\mathbf{r}\rho_e(\mathbf{r})\epsilon_{xc}(\rho_e(\mathbf{r})), \tag{6.3}$$

where $\epsilon_{xc}(\rho_e)$ is the exchange–correlation energy density of the homogeneous electron gas at density ρ_e.

The terms of the total energy E (Eq. 6.2) are implemented in the CP *FORTRAN* code by the following formulas:

$$E_{ke} = \frac{1}{2}\sum_{i=1}^{M} f_i \sum_{\mathbf{q}} G^2 c_i^*(\mathbf{q}) c_i(\mathbf{q}) \tag{6.4}$$

$$E_{xc} = \int \mathrm{d}\mathbf{r}\epsilon_{xc}(\rho_e(\mathbf{r}))\rho_e(\mathbf{r}) \tag{6.5}$$

$$E^{ps}_{loc} = \Omega \sum_{\mathbf{q}} \rho_e^*(\mathbf{G}) S(\mathbf{G}) v_{loc}(|\mathbf{G}|) \tag{6.6}$$

$$E^{ps}_{nl} = \begin{cases} \sum_i f_i \sum_{nn'} D^0_{nn'} \sum_I \langle\psi_i|\beta^I_n\rangle\langle\beta^I_{n'}|\psi_i\rangle & \text{for US–PP} \\ \sum_i f_i \sum_{lm} \langle\phi_{lm}|\delta v_l|\phi_{lm}\rangle^{-1} \sum_I \langle\psi_i|\xi^I_{lm}\rangle\langle\xi^I_{lm}|\psi_i\rangle & \text{for NC–PP} \end{cases} \tag{6.7}$$

$$E_H = \frac{4\pi\Omega}{2}\sum_{\mathbf{q}\neq 0}\rho_T^*(\mathbf{G})\frac{1}{G^2}\rho_T(\mathbf{G}) \tag{6.8}$$

$$E_{sr} = \frac{1}{2}\sum_{I=1}^{N}\sum_{J\neq I}^{N}\frac{Z_v^2}{|\mathbf{R}_I-\mathbf{R}_J|}\,\mathrm{erfc}\left(\frac{|\mathbf{R}_I-\mathbf{R}_J|}{R_c\sqrt{2}}\right) \tag{6.9}$$

$$E_{self} = \frac{1}{\sqrt{2\pi}}\frac{NZ^2}{R_c}. \tag{6.10}$$

In the Eq. 6.6 $S(\mathbf{G}) = \sum_I \exp(-i\mathbf{G}\cdot\mathbf{R}_I)$ is the structure factor for the ions, which, thanks to Eq. 3.6, is invariant under a change of $\mathbf{h}$. Notice that in the previous formulas appear both quantities defined on the *real* and on *scaled* cell, by using the scale transformation laws for coordinates and wave–functions in direct and Fourier space (Eqs. 2.2, 2.19, 2.20, 3.5, 3.7).

We write now the explicit expression for the derivative of the previous terms of E with respect to the matrix $\mathbf{h}$, in a unified formulation valid both for US–PP and NC–PP. In the latter case, to get the right expressions $\rho_e^{hard} = 0$.

$$\frac{\partial E_{ke}}{\partial \mathbf{h}_{\alpha\beta}} = -\sum_{i=1}^{M} f_i \sum_{\mathbf{q}} \mathbf{G}_\alpha \mathbf{G}_\gamma (\mathbf{h}^t)^{-1}_{\gamma\beta} c_i^*(\mathbf{q}) c_i(\mathbf{q}) \tag{6.11}$$

$$\begin{aligned}\frac{\partial E_{xc}}{\partial \mathbf{h}_{\alpha\beta}} &= \left\{\int d\mathbf{r}\,[\epsilon_{xc}(\rho_e(\mathbf{r})) - v_{xc}(\mathbf{r})]\,\rho_e(\mathbf{r})\right\}(\mathbf{h}^t)^{-1}_{\alpha\beta} \\ &+ \int d\mathbf{r} v_{xc}(\mathbf{r})\left(\rho_e^{hard}(\mathbf{r})(\mathbf{h}^t)^{-1}_{\alpha\beta} + \frac{\partial \rho_e^{hard}(\mathbf{r})}{\partial \mathbf{h}_{\alpha\beta}}\right)\end{aligned} \tag{6.12}$$

$$\begin{aligned}\frac{\partial E_{loc}^{ps}}{\partial \mathbf{h}_{\alpha\beta}} &= -\Omega\sum_{\mathbf{q}}\rho_e^*(\mathbf{G})S(\mathbf{G})\left(\frac{\partial v_{loc}(|\mathbf{G}|)}{\partial G^2}2\mathbf{G}_\alpha\mathbf{G}_\gamma + v_{loc}(|\mathbf{G}|)\delta_{\alpha\gamma}\right)(\mathbf{h}^t)^{-1}_{\gamma\beta} \\ &+ \Omega\sum_{\mathbf{q}}\left(\rho_e^{hard}(\mathbf{G})^*(\mathbf{h}^t)^{-1}_{\alpha\beta} + \frac{\partial\rho_e^{hard}(\mathbf{G})^*}{\partial\mathbf{h}_{\alpha\beta}}\right)S(\mathbf{G})v_{loc}(|\mathbf{G}|)\end{aligned} \tag{6.13}$$

$$\frac{\partial E_{nl}^{ps}}{\partial \mathbf{h}_{\alpha\beta}} = \begin{cases} 2\sum_i f_i \sum_{nn'} D^0_{nn'} \sum_I \mathrm{Re}\left[\frac{\partial}{\partial\mathbf{h}_{\alpha\beta}}\langle\psi_i|\beta_n^I\rangle\langle\beta_{n'}^I|\psi_i\rangle\right] & \text{for US–PP} \\ 2\sum_i f_i \sum_{lm}\alpha_{lm}\sum_I \mathrm{Re}\left[\frac{\partial}{\partial\mathbf{h}_{\alpha\beta}}\langle\psi_i|\xi_l m^I\rangle\langle\xi_l m^I|\psi_i\rangle\right] & \text{for NC–PP}\end{cases} \tag{6.14}$$

$$\frac{\partial E_H}{\partial \mathrm{h}_{\alpha\beta}} = \left[-E_H\delta_{\alpha\gamma} + 4\pi\Omega\sum_{\mathbf{q}\neq 0}\frac{\rho_t^*(\mathbf{G})}{|\mathbf{G}|^2}\left(\frac{\rho_t(\mathbf{G})}{|\mathbf{G}|^2}+\frac{1}{2}\rho_{ion}(\mathbf{G})R_c^2\right)\mathbf{G}_\alpha\mathbf{G}_\gamma\right](\mathrm{h}^t)^{-1}_{\gamma\beta}$$
$$+ 4\pi\Omega\mathrm{Re}\left[\sum_{\mathbf{q}\neq 0}\frac{\rho_t^*(\mathbf{G})}{|\mathbf{G}|^2}\left(\rho_e^{hard}(\mathbf{G})^*(\mathrm{h}^t)^{-1}_{\alpha\beta}+\frac{\partial\rho_e^{hard}(\mathbf{G})^*}{\partial \mathrm{h}_{\alpha\beta}}\right)\right] \quad (6.15)$$

$$\frac{\partial E_{sr}}{\partial \mathrm{h}_{\alpha\beta}} = -\frac{1}{2}\sum_I\sum_{J\neq I}\left\{\frac{Z_v^2}{|\mathbf{R}_I-\mathbf{R}_J|^3}\mathrm{erfc}\left(\frac{|\mathbf{R}_I-\mathbf{R}_J|}{R_c\sqrt{2}}\right)\right. \quad (6.16)$$
$$\left. + \frac{\sqrt{2}}{R_c\sqrt{\pi}}\frac{Z_v^2}{|\mathbf{R}_I-\mathbf{R}_J|^2}\exp\left(-\frac{|\mathbf{R}_I-\mathbf{R}_J|^2}{R_c\sqrt{2}}\right)\right\}(\mathbf{R}_I^\alpha-\mathbf{R}_J^\alpha)(\mathbf{R}_I^\gamma-\mathbf{R}_J^\gamma)(\mathrm{h}^t)^{-1}_{\gamma\beta}$$

$$\frac{\partial E_{self}}{\partial \mathrm{h}} = 0\,. \quad (6.17)$$

In Eq. 6.12 $v_{xc}(\mathbf{r}) = \frac{\partial\epsilon_{xc}\rho_e}{\partial\rho_e(\mathbf{r})}$; in Eq. 6.14 $\alpha_{lm} = \langle\phi_{lm}|\delta v_l|\phi_{lm}\rangle^{-1}$. Note that in Eq. 6.14 for US–PP, the symmetry of D^0 ($D^0_{nn'} = D^0_{n'n}$) has been used.

To conclude this Appendix we give in detail the derivative of the scalar product $\langle\beta_n^I|\psi_i\rangle$ ($\langle\xi_{lm}^I|\psi_i\rangle$) and of ρ_e^{hard}.

Let us consider $\frac{\partial}{\mathrm{h}_{\alpha\beta}}\langle\psi_i|\beta_n^I\rangle$: $|\beta_n^I\rangle$ is an atomic state (with momentum l) centered on I-th ion. Using the plane–wave basis set we can write the previous scalar product as:

$$\langle\psi_i|\beta_n^I\rangle = \sum_{\mathbf{q}}(-i)^l c_i^*(\mathbf{q})\mathrm{e}^{-i\mathbf{q}\cdot\mathbf{S}}Y_{lm}(\hat{\mathbf{G}})\frac{4\pi}{\sqrt{\Omega}}\int_0^\infty \mathrm{d}x x^2\tilde{\beta}_n(x)j_l(|\mathbf{G}|x), \quad (6.18)$$

where Y_{lm} is the spherical harmonic function with indices l, m, $\hat{\mathbf{G}}$ the versor of vector $\mathbf{G}$, j_l the bessel function and $\tilde{\beta}_n(x)$ the radial component of $\beta_n(\mathbf{r})$. Using this expression one immediately recognize the dependence of Eq. 6.18 on h, through $Y_{lm}(\tilde{\mathbf{G}})$, Ω and $j_l(|\mathbf{G}|x)$. We can thus write:

$$\frac{\partial}{\partial \mathrm{h}_{\alpha\beta}}\langle\psi_i|\beta_n^I\rangle = \sum_{\mathbf{q}}(-i)^l c_i^*(\mathbf{q})\mathrm{e}^{-i\mathbf{q}\cdot\mathbf{S}_I}\frac{4\pi}{\sqrt{\Omega}}\left[\left(\frac{\partial Y_{lm}(\hat{\mathbf{G}})}{\partial \mathrm{h}_{\alpha\beta}}-\frac{1}{2}Y_{lm}(\hat{\mathbf{G}})(\mathrm{h}^t)^{-1}_{\alpha\beta}\right)\right.$$
$$\left.\int_0^\infty \mathrm{d}x x^2\tilde{\beta}_n(x)j_l(|\mathbf{G}|x) + Y_{lm}(\hat{\mathbf{G}})\int_0^\infty \mathrm{d}x x^2\tilde{\beta}_n(x)\frac{\partial j_l(|\mathbf{G}|x)}{\partial \mathrm{h}_{\alpha\beta}}\right]. \quad (6.19)$$

Eq. 6.18 is also valid for the derivative of $\langle \xi^I_{lm} | \psi_i \rangle$) and of ρ_e^{hard}, with the replacement of $\tilde{\beta}_n(x)$ with $\delta v_l(x)\phi_{lm}(x)$ (see Eq. 3.16).

Let us consider ρ_e^{hard} (Eq. 3.19). We need $\partial \rho_e^{hard}/\partial h$ both in direct (Eq. 6.12) and in reciprocal space (Eqs. 6.13 and 6.15). From the definition of ρ_e^{hard} (see Eq. 3.19) in Fourier space, one has:

$$\begin{aligned} \frac{\partial \rho_e^{hard}(\mathbf{G})}{\partial \mathrm{h}_{\alpha\beta}} &= \sum_{nn'I} \frac{\partial Q_{nn'}}{\partial \mathrm{h}_{\alpha\beta}} \mathrm{e}^{-\mathrm{q}\cdot\mathrm{S}_I} \sum_i f_i \langle \psi_i | \beta_n^I \rangle \langle \beta_{n'}^I | \psi_i \rangle \\ &+ \sum_{nn'I} Q_{nn'} \mathrm{e}^{-\mathrm{q}\cdot\mathrm{S}_I} 2\mathrm{Re} \sum_i f_i \frac{\partial}{\mathrm{h}_{\alpha\beta}} \langle \psi_i | \beta_n^I \rangle \langle \beta_{n'}^I | \psi_i \rangle. \end{aligned} \tag{6.20}$$

Like β_n^I, the functions $Q^I_{nn'}(\mathbf{r})$ are centered on I-th ion, and localized in atomic core region. They are given by a linear combination of products of atomic functions (with given momentum) [29]. It is therefore possible to expand them in spherical harmonic functions. In reciprocal space we have:

$$Q^I_{nn'}(\mathbf{G}) = \mathrm{e}^{-i\mathbf{G}\cdot\mathbf{R}_I} \sum_{lm} (-i)^l \mathcal{A}(l,m;n,n') Y_{lm}(\hat{\mathbf{G}}) \frac{4\pi}{\Omega} \int_0^\infty \mathrm{d}x x^2 \tilde{Q}_{nn'}(x) j_l(|\mathbf{G}|x), \tag{6.21}$$

where $\mathcal{A}(l,m;n,n')$ are the coefficients defined in Ref. [92], $\tilde{Q}_{nn'}(x)$ the radial components of $Q_{nn'}(\mathbf{r})$, and the sum over l runs from 0 to (l_m+1), where l_m is the maximum angular quantum number of states $|\beta_n\rangle$. Like in Eq. 6.18, the dependence of Eq. 6.21 on h is through $Y_{lm}(\hat{\mathbf{G}})$, Ω and $j_l(|\mathbf{G}|x)$. To calculate $\frac{\partial \rho_e^{hard}(\mathbf{r})}{\partial \mathrm{h}_{\alpha\beta}}$ we choose to transform directly Eq. 6.20 using FFT.

The constraints contribution to internal stress (second term of Eq. 3.27), from Eq. 3.25 and Eq. 3.26, is given by:

$$\sum_{ij} \Lambda_{ij} \frac{\partial}{\partial \mathrm{h}_{\alpha\beta}} \langle \psi_i | S | \psi_j \rangle = \sum_{ij} \Lambda_{ij} \sum_{nn'} q_{nn'} \left[\frac{\partial}{\partial \mathrm{h}_{\alpha\beta}} \langle \psi_i | \beta_n^I \rangle \langle \beta_{n'}^I | \psi_j \rangle + \langle \psi_i | \beta_n^I \rangle \frac{\partial}{\partial \mathrm{h}_{\alpha\beta}} \langle \beta_{n'}^I | \psi_j \rangle \right] \tag{6.22}$$

and can be calculated very simply using Eq. 6.19 for $\frac{\partial}{\partial \mathrm{h}_{\alpha\beta}} \langle \psi_i | \beta_n^I \rangle \langle \beta_{n'}^I | \psi_j \rangle$.

6.2 Computational effort for stress calculation

We now investigate the computational effort needed to calculate internal stress with the two different types of pseudopotential implemented in our method, and fix the convenience criterion for choosing between them.

In the Car–Parrinello method many parts of the molecular–dynamics algorithm are performed in $O(MN \ln N)$ operations, where M is the number of electronic wave–functions and N the number of plane–waves used to expand each of them. This performance is due to FFT techniques, used to switch from direct to reciprocal space and vice–versa, since terms of Eq. 3.1 arising from the local potential and kinetic energy are diagonal in direct and reciprocal space respectively. The wave–functions orthogonalization algorithm used to solve the Lagrange multiplier Λ_{ij} in Eq. 2.21 requires $O(M^2N)$ operations, since one has to deal with $M \times M$ overlap matrices and each term of them is a scalar product between wave–functions, which costs $O(N)$ of operations in reciprocal space. Finally, the part of the method concerned with evaluating non–local contributions to total energy, forces and stresses, calculated in reciprocal space, scales like $O(mMN)$, where m is the number of atoms in the simulation cell.

Since both M and N scales like m, orthogonalization step and non–local operations scale like m^3, but in general the prefactor associated with the second is larger than that for the first.

The FFT and orthogonalization algorithms do not depend on the pseudopotential used. Thus the time spent in these parts of the method is anyway reduced by using the US–PP thanks to the smaller energy cut–off needed in the expansion Eq. 3.2. Nevertheless, for large systems the calculation of non–local contributions becomes the most time consuming part. The order mMN of operations for this part comes from the scalar products in Eq. 3.16 and Eq. 3.24 for the two classes of pseudopotentials respectively. These scalar products are performed in reciprocal space and are given by a sum over **G**–vectors of terms containing the Fourier coefficients of the wave–functions, the spherical harmonic functions and one–dimensional integrals depending on $|\mathbf{G}|$ (see Eq. 6.18). The number of operations needed to calculate one scalar product of this type scales thus like the number of plane–waves (N) (like for the terms of the matrices used for the orthogonalization algorithm). The number of these scalar products is given by mM times the number of atomic functions used for the pseudopotential (N_ξ or N_β). When forces and stress tensor are needed, one has to calculate also the derivatives of these scalar products. Note also that for US–PP the presence of $\hat{S}$ operator in Eq. 3.25 and of ρ_e^{hard} (Eq. 3.19) requires the calculation of the same scalar products of Eq. 3.24, and thus these quantities and their derivatives do not require any additional relevant computation. Summarizing, if we take $N_\beta = 2N_\xi$, the total number of scalar products is twice larger for US–PP than for NC–PP and, at least for fixed–cell Molecular Dynamics, the ultra–soft scheme becomes advantageous compared

with the norm–conserving one when the number of plane–waves for the first is less than one half the number of plane–waves for the second. In terms of energy cut–off for the expansion Eq. 3.2, this gives:

$$E_{cut}^{US} < \frac{1}{2^{2/3}} E_{cut}^{NC}. \tag{6.23}$$

When the cell is moving the situation is quite different: the set of **G**–vectors in reciprocal space varies, together with the simulation cell. This implies that the one–dimension integrals which appears in the scalar products $\langle\psi_i|\beta_n^I\rangle$ or $\langle\psi_i|\xi_{lm}^I\rangle$ should in principle be calculated at each step of the simulation, because of their dependence on $|\mathbf{G}|$. This would add a relevant computational overhead, expecially for low–symmetry cells, where one has a large number of **G**–shells. To avoid this problem we have tabulated these integrals as functions of G on a uniform one–dimensional mesh from 0 to a given G_{max} depending on the pseudopotential and interpolating at each step the integrals for the actual $|\mathbf{G}|$. This is done both for NC–PP and US–PP and thus it does not change the criterion of Eq. 3.28.

Another problem related with the change of **G**–vectors is the cost for the computation of the augmentation functions $Q_{nn'}$ in reciprocal space (Eq. 6.21), and their partial derivatives with respect to $\mathbf{h}_{\alpha\beta}$, which are peculiar of the US–PP scheme and have to be calculated at each time step of the simulation. It is not straightforward to get the new convenience criterion by modifying Eq. 3.28. In particular the one–dimensional integrals which enter in the calculation of $Q_{nn'}$ (see Eq. 6.21) are of the same type of those discussed above: we can again tabulate these integrals and reduce the operations required by using the symmetries of $Q_{nn'}$. In Table 6.1 we compare the computer time for a single free–cell MD step using Vanderbilt ultra–soft and norm–conserving pseudopotential for

E_{cut} (Ry)	Mesh	Time (s/step)	
		NC–PP	Ultra–soft PP
8	20		26
12	24		58
24	36	30	110
36	40	61	205
48	48	82	
60	56	107	
72	60	134	

Table 6.1: Computational cost of free dynamics with variable cell. Comparison between Norm–conserving (NC–PP) and Ultra–soft (Ultra–soft PP) pseudopotentials. For different energy cut–off is reported the CPU time of a step of dynamics with variable cell for a system of 32 Oxygen atoms. In the second column there is the linear size of the corresponding cubic mesh used for FFT. The computer used is a workstation IBM-Risc/6000 580.

different energy cut-off. The data refer to a system of 32 Oxygen molecules arranged in a orthorhombic simulation box. One can see that for such a system and variable simulation cell it is convenient to use Ultra–soft pseudopotentials instead of Norm–conserving ones when:

$$E_{cut}^{US} < \frac{1}{3} E_{cut}^{NC}. \tag{6.24}$$

Bibliography

[1] M.T. Yin and M.L. Cohen, Phys. Rev. B **26**, 5668 (1982).

[2] R. Car and M. Parrinello, Phys. Rev. Lett. **55**, 2471 (1985).

[3] M. Parrinello and A. Rahman, Phys. Rev. Lett. **45**, 1196 (1980).

[4] H.C. Andersen, J. Chem. Phys. **72**, 2384 (1980).

[5] see for example: L. Landau and E.M. Lifshitz, "Theory of Elasticity", (Pergamon Press, Oxford, 1959).

[6] M. Parrinello, in *Molecular Dynamics Simulations of Statistical-Mechanical Systems*, ed. by G. Ciccotti and W.G. Hoover (North-Holland, 1986).

[7] J.R. Ray and A. Rahman, J. Chem. Phys. **80**, 4423 (1984).

[8] M. Parrinello and A. Rahman, J. Appl. Phys., **52**, 7182 (1981).

[9] S. Nosé, Mol. Phys. **52**, 255 (1984).

[10] S. Melchionna, G. Ciccotti and B.L. Holian, Mol. Phys. **78**, 533 (1993).

[11] R.M. Wentzcovitch, Phys. Rev. B **44**, 2358 (1991).

[12] J.P. Hansen and I.R. Donald, *Theory of Simple Liquids*, (Academic Press, 1976).

[13] R. Car and M. Parrinello, in *Simple Molecular Systems at Very High Density* (Plenum Publishing Corp., 1989) p. 455.

[14] D.K. Remler and P.A. Madden, Mol. Phys. **70**, 921 (1990).

[15] G. Galli and A. Pasquarello, in *Computer Simulation in Chemical Physics*, ed. M.P Allen and D.J. Tildesley (Kluwer Acedemic Publisher, 1993), p.261.

[16] P. C. Hohenberg and W. Kohn, Phys. Rev. **136** B864 (1964).

[17] W. Kohn and L. J. Sham, Phys. Rev. **140**, A1133 (1965).

[18] W. Kohn and P. Vashishta, in *Theory of the Inhomogeneous Electron Gas*, ed. S. Lundqvist and N. H. March, Plenum Publishing Corp., New York (1983).

[19] G. Galli and M. Parrinello in *Computer Simulation in Material Science*, edited by M. Meyer and V. Pontikis (Kluwer, Dordrecht, 1991).

[20] G. Pastore, E. Smargiassi, and F. Buda, Phys. Rev. A, **44**, 6334 (1991).

[21] P. E. Blöchl and M. Parrinello, Phys. Rev. B **45**, 9413 (1992).

[22] F. Buda, R. Car and M. Parrinello, Phys. Rev. B **41**, 1680 (1990).

[23] O.H. Nielsen and R.M. Martin, Phys. Rev. Lett. **50**, 697 (1983).

[24] O.H. Nielsen and R.M. Martin, Phys. Rev. B **32**, 3780 (1985).

[25] D. R. Hamann, M. Schlüter e C. Chiang, Phys. Rev. Lett. **43**, 1494 (1979).

[26] G. B. Bachelet, D. R. Hamann e M. Schlüter, Phys. Rev. B **26**, 4199 (1982).

[27] D. M. Ceperley e B. K. Alder, Phys. Rev. Lett. **45**, 566 (1980).

[28] J. C. Perdew e A. Zunger, Phys. Rev. B **23**, 5048 (1981).

[29] D. Vanderbilt, Phys. Rev. Lett. **41**, 7892 (1990).

[30] L. Kleinman e D. M. Bylander, Phys. Rev. Lett. **48**, 1425 (1982).

[31] X. Gonze, P. Käckel and M. Scheffler, Phys. Rev. B **41**, 12264 (1990).

[32] K. Laasonen, A. Pasquarello, R. Car, C. Lee and D. Vanderbilt, Phys. Rev. B **47**, 10142 (1993).

[33] A. Pasquarello, K. Laasonen, R. Car, C. Lee and D. Vanderbilt, Phys. Rev. Lett. **69**, 1982 (1992).

[34] C. Lee, D. Vanderbilt, K. Laasonen, R. Car, and M. Parrinello, Phys. Rev. Lett. **69**, 462 (1992).

[35] K. Laasonen, M. Parrinello, R. Car, C. Lee and D. Vanderbilt, Chem. Phys. Lett.

[36] P. Gomes Dacosta, O.H. Nielsen and K. Kunc, J. Phys. C **19**, 3163 (1986).

[37] M. Bernasconi, G.L. Chiarotti, P. Focher, S. Scandolo, E. Tosatti and M. Parrinello, J. Phys. and Chem. of Solids. (1994).

[38] P. Focher, G.L. Chiarotti, M. Bernasconi, E. Tosatti and M. Parrinello, Europhys. Lett. **36**, 345 (1994).

[39] S.J. Duclos, Y.K. Vohra and A.L. Ruoff, Phys. Rev. B **41**, 12021 (1990).

[40] J.Z. Hu, L.D. Merkle, C.S. Menoni and I.L. Spain, Phys. Rev. B **34**, 4679 (1986), and references therein.

[41] M.I. McMahon *et al.*, Phys. Rev. B **50**, 739 (1994).

[42] M. Imai, K. Yaoita, Y. Katayama, J.–Q. Chen, Jour. of Non–Cryst. Solids **150**, 49 (1992).

[43] K. J. Chang and M. L. Cohen, Phys. Rev. B **31**, 7819 (1985).

[44] R. J. Needs and R. M. Martin, Phys Rev. B **30**, 5390 (1984).

[45] I. Štich, R. Car and M. Parrinello, Phys. Rev. B **44**, 11092 (1991).

[46] W. Andreoni, D. Sharf and P. Giannozzi, Chem. Phys. Lett. **173**, 449 (1990).

[47] F. Tassone, F. Mauri and R. Car, to be published

[48] M.E. Tuckerman and M. Parrinello, submitted to J. Chem. Phys. (1994).

[49] A.F. Hebard, M.J. Rosseinsky, R.C. Haddon, D.W. Murph, S.H Glarum, T.T.M. Palstra, A.P. Ramirez and A.R. Kortan, Nature **350**, 600 (1991).

[50] R.S. Ruoff and A.L. Ruoff, Nature **350**, 663 (1991).

[51] C.S. Yoo and W.J. Nellis, Science **254**, 1489 (1991).

[52] M. Núnez Regueiro, P. Monceau and J.L. Hodeau, Nature **355**, 237 (1992).

[53] F.M. Moshary, N.H. Chen and I.F. Silvera, Phys. Rev. Lett. **69**, 466 (1992).

[54] M. Núnez Regueiro, P. Monceau, A. Rassat, P. Bernier and A. Zahab, Nature **354**, 289 (1991)

[55] S.J. Duclos, K. Brister, R.C. Haddon, A.R. Kortan and F.A. Thiel, Nature **351**, 380 (1991).

[56] M. Núnez Regueiro, private communication.

[57] Y. Iwasa, T. Arima, R.M. Fleming, T. Siegrist, O. Zhou, R.C. Haddon, L.J. Rothberg, K.B.Lyons, H.L. Carter jr., A.F. Hebard, R. Tycho, G. Dabbagh, J.J. Krajewski, G.A. Thomas and T. Yagi, Science **264**, 1570 (1994).

[58] R.D. Johnson, N. Yannoni, G. Meijer and D.S. Bethune

[59] W. Andreoni, in *Electronic Properties of Fullerenes*, ed. H. Kuzmany, J. Fink, M. Mehring and S. Roth (Springer–Verlag, 1993).

[60] P.A. Heiney, J.E. Fisher, A.R. McGhie, W.J. Romanow, A.M. Denenstein, J.P. McCauley Jr., A.B. Smith III and D.E. Cox, Phys. Rev. Lett. **66**, 2911 (1991).

[61] R.W. Lof *et al.*, Phys. Rev. Lett **68**, 3924 (1992).

[62] D.W. Snoke, K. Syassen and A. Mittelbach, Phys. Rev. B **47**, 4146 (1993).

[63] W. Andreoni, private communication.

[64] D.L. Strout *et al.*, Chem. Phys. Lett. **214**, 576 (1993).

[65] J. Robertson, Adv. in Phys. **35**, 317 (1986).

[66] G. Galli, R.M. Martin, R. Car and M. Parrinello, Phys. Rev. B **42**, 7470 (1990).

[67] R.W. Godby, M. Schlüter and L.J. Sham, Phys. Rev. Lett. **56**, 2415 (1986).

[68] N. Troullier and J.L. Martins, Phys. Rev. B **46**, 1754 (1992).

[69] E.L. Shirley and S.G. Louie, Phys. Rev. Lett. **71**, 133 (1993).

[70] F.P. Bundy, Physica A **156**, 169 (1989).

[71] R. Clarke and C. Uher, Adv. Phys. **33**, 469 (1984).

[72] T. Yagi, W. Utsumi, M. Yamakata, T. Kikegawa and O. O. Shimomura, Phys. Rev. B **46**, 6031 (1992).

[73] S. Endo, N. Idani, R. Oshima, K.J. Takano and M. Wakatsuki, Phys. Rev. B **49**, 22 (1994).

[74] F.P. Bundy and J.S. Kasper, J. Chem. Phys. **46**, 3437 (1967).

[75] K.J. Takano, H. Harashima and M. Wakatsuki, Jpn. J. Appl. Phys. **30**, L860 (1991).

[76] M.T. Yin and M.L. Cohen, Phys. Rev. B **29**, 6996 (1984).

[77] S. Fahy, S.G. Louie and M.L. Cohen, Phys. Rev. B **35**, 7623 (1987).

[78] S. Fahy, S.G. Louie and M.L. Cohen, Phys. Rev. B **34**, 1191 (1986).

[79] Ç. Mailhiot and A.K. McMahan, Phys. Rev. B **44**, 11578 (1991)

[80] D.J. Chadi and M.L. Cohen, Phys. Rev. B **8**, 5747 (1973).

[81] E.J. Wheeler and D. Lewis, Mat. Res. Bull. **10**, 687 (1975).

[82] A.V. Kurdyumov, Sov. Phys. Dokl. **20**, 218 (1975).

[83] R. Meer, A.L.German and D.Heikens, J. Polym. Sci. **15**, 1765 (1977).

[84] J.E. Rice and Y. Okamoto, J. Org. Chem. **44**, 446 (1981).

[85] *Polydiacetylenes*, ed. by H.J. Cantow, (Springer Verlag, Berlin 1984).

[86] K. Aoki, Y. Kakudate, S. Usuba, M. Yoshida, K. Tanaka, and S. Fujiwara, J. Chem. Phys. **88**, 4565 (1988).

[87] A.D. Becke, Phys. Rev. A **38**, 3098 (1988).

[88] J.P. Perdew, Phys. Rev. B **33**, 8822 (1986).

[89] R. LeSar, J. Chem. Phys. **86**, 1485 (1987).

[90] M. Nicol and G.Z. Yin, J. Phys. Colloque **45**, C8-163 (1984).

[91] P. Focher and G.L. Chiarotti (CNR Rapporto Tecnico, Trieste, 1992).

[92] M. Weissbluth, *Atoms and Molecules*, (Academic Press, 1978), pag. 246.